

Automatic Modeling of Building Interiors Using Low-Cost Sensor Systems

A thesis accepted by the Faculty of Aerospace Engineering and Geodesy of the University of Stuttgart in partial fulfilment of the requirements for the degree of Doctor of Engineering Sciences (Dr.-Ing.)

by

Ali Mohammad Khosravani

born in Shiraz, Iran

Main referee: Prof. Dr.-Ing. habil. Dieter Fritsch
Co-referee: Prof. Dr.-Ing. habil. Volker Schwieger
Date of defence: December 09, 2015

Institute for Photogrammetry
University of Stuttgart
2016

**Automatic Modeling of Building Interiors
Using Low-Cost Sensor Systems**

Von der Fakultät Luft- und Raumfahrttechnik und Geodäsie
der Universität Stuttgart
zur Erlangung der Würde eines
Doktors der Ingenieurwissenschaften (Dr.-Ing.)
genehmigte Abhandlung

Vorgelegt von

M.Sc. Ali Mohammad Khosravani

aus Shiraz, Iran

München 2016

Verlag der Bayerischen Akademie der Wissenschaften
in Kommission beim Verlag C. H. Beck

Adresse der Deutschen Geodätischen Kommission:



Deutsche Geodätische Kommission

Alfons-Goppel-Straße 11 • D – 80 539 München

Telefon +49 – 89 – 23 031 1113 • Telefax +49 – 89 – 23 031 -1283 / - 1100

e-mail hornik@dgfi.badw.de • <http://www.dgk.badw.de>

Hauptberichter: Prof. Dr.-Ing. habil. Dieter Fritsch

Mitberichter: Prof. Dr.-Ing. habil. Volker Schwieger

Tag der mündlichen Prüfung: 09.12.2015

Diese Dissertation ist auf dem Server der Deutschen Geodätischen Kommission unter <http://dgk.badw.de/>
sowie auf dem Server der Universität Stuttgart unter <http://elib.uni-stuttgart.de/opus/doku/e-diss.php>
elektronisch publiziert

© 2016 Deutsche Geodätische Kommission, München

Alle Rechte vorbehalten. Ohne Genehmigung der Herausgeber ist es auch nicht gestattet,
die Veröffentlichung oder Teile daraus auf photomechanischem Wege (Photokopie, Mikrokopie) zu vervielfältigen.

This dissertation is gratefully dedicated to my beloved mother, for her endless love and encouragements, and to my late father.

Kurzfassung

Die dreidimensionale Rekonstruktion von Innenraumszenen zielt darauf ab, die Form von Gebäudeinnenräumen als Flächen oder Volumina abzubilden. Aufgrund von Fortschritten im Bereich der Technologie entfernungsmessender Sensoren und Algorithmen der Computervision sowie verursacht durch das gesteigerte Interesse vieler Anwendungsgebiete an Innenraummodellen hat dieses Forschungsfeld in den letzten Jahren zunehmend an Aufmerksamkeit gewonnen. Die Automatisierung des Rekonstruktionsprozesses ist weiterhin Forschungsgegenstand, verursacht durch die Komplexität der Rekonstruktion, der geometrischen Modellierung beliebig geformter Räume und besonders im Falle unvollständiger oder ungenauer Daten. Die hier vorgestellte Arbeit hat die Erhöhung des Automatisierungsgrades dieser Aufgabe zum Ziel, unter der Verwendung einer geringen Anzahl an Annahmen bzgl. der Form von Räumen und basierend auf Daten, welche mit Low-Cost-Sensoren erfasst wurden und von geringer Qualität sind.

Diese Studie stellt einen automatisierten Arbeitsablauf vor, welcher sich aus zwei Hauptphasen zusammensetzt. Die erste Phase beinhaltet die Datenerfassung mittels eines kostengünstigen und leicht erhältlichen Sensorsystems, der Microsoft Kinect. Die Entfernungsdaten werden anhand von Merkmalen, welche im Bildraum oder im 3D Objektraum beobachtet werden können, registriert. Ein neuer komplementärer Ansatz für die Unterstützung der Registrierungsaufgabe wird präsentiert, da diese Ansätze zur Registrierung in manchen Fällen versagen können, wenn die Anzahl gefundener visueller und geometrischer Merkmale nicht ausreicht. Der Ansatz basiert auf der Benutzerfußspur, welche mittels einer Innenraumpositionierungsmethode erfasst wird, und auf einem vorhandenen groben Stockwerksmodell.

In der zweiten Phase werden aus den registrierten Punktwolken mittels eines neuen Ansatzes automatisiert hochdetaillierte 3D-Modelle abgeleitet. Hierzu werden die Daten im zweidimensionalen Raum verarbeitet (indem die Punkte auf die Grundrissebene projiziert werden) und die Ergebnisse werden durch eine Extrusion in den dreidimensionalen Raum zurückgewandelt (wobei die Raumhöhe mittels einer Histogrammanalyse der in der Punktwolke enthaltenen Höhen erfasst wird). Die Datenanalyse und -modellierung in 2D vereinfacht dabei nicht nur das Rekonstruktionsproblem, sondern erlaubt auch eine topologische Analyse unter Verwendung der Graphentheorie. Die Leistungsfähigkeit des Ansatzes wird dargestellt, indem Daten mehrerer Sensoren verwendet werden, die unterschiedliche Genauigkeiten liefern, und anhand der Erfassung von Räumen unterschiedlicher Form und Größe.

Abschließend zeigt die Studie, dass die rekonstruierten Modelle verwendbar sind, um vorhandene grobe Innenraummodelle zu verfeinern, welche beispielsweise aus Architekturzeichnungen oder Grundrissplänen abgeleitet werden können. Diese Verfeinerung wird durch die Fusion der detaillierten Modelle einzelner Räume mit dem Grobmodell realisiert. Die Modellfusion beinhaltet dabei die Überbrückung von Lücken im detaillierten Modell unter Verwendung eines neuen, auf maschinellem Lernen basierenden Ansatzes. Darüber hinaus erlaubt der Verfeinerungsprozess die Detektion von Änderungen oder Details, welche aufgrund der Generalisierung des Grobmodells oder Renovierungsarbeiten im Gebäudeinnenraum fehlten.

Abstract

Indoor reconstruction or 3D modeling of indoor scenes aims at representing the 3D shape of building interiors in terms of surfaces and volumes, using photographs, 3D point clouds or hypotheses. Due to advances in the range measurement sensors technology and vision algorithms, and at the same time an increased demand for indoor models by many applications, this topic of research has gained growing attention during the last years. The automation of the reconstruction process is still a challenge, due to the complexity of the data collection in indoor scenes, as well as geometrical modeling of arbitrary room shapes, specially if the data is noisy or incomplete. Available reconstruction approaches rely on either some level of user interaction, or making assumptions regarding the scene, in order to deal with the challenges. The presented work aims at increasing the automation level of the reconstruction task, while making fewer assumptions regarding the room shapes, even from the data collected by low-cost sensor systems subject to a high level of noise or occlusions. This is realized by employing topological corrections that assure a consistent and robust reconstruction.

This study presents an automatic workflow consisting of two main phases. In the first phase, range data is collected using the affordable and accessible sensor system, Microsoft Kinect. The range data is registered based on features observed in the image space or 3D object space. A new complementary approach is presented to support the registration task in some cases where these registration approaches fail, due to the existence of insufficient visual and geometrical features. The approach is based on the user's track information derived from an indoor positioning method, as well as an available coarse floor plan.

In the second phase, 3D models are derived with a high level of details from the registered point clouds. The data is processed in 2D space (by projecting the points onto the ground plane), and the results are converted back to 3D by an extrusion (room height available from the point height histogram analysis). Data processing and modeling in 2D does not only simplify the reconstruction problem, but also allows for topological analysis using the graph theory. The performance of the presented reconstruction approach is demonstrated for the data derived from different sensors having different accuracies, as well as different room shapes and sizes.

Finally, the study shows that the reconstructed models can be used to refine available coarse indoor models which are for instance derived from architectural drawings or floor plans. The refinement is performed by the fusion of the detailed models of individual rooms (reconstructed in a higher level of details by the new approach) to the coarse model. The model fusion also enables the reconstruction of gaps in the detailed model using a new learning-based approach. Moreover, the refinement process enables the detection of changes or details in the original plans, missing due to generalization purposes, or later renovations in the building interiors.

Contents

Kurzfassung.....	5
Abstract	6
1. Introduction.....	11
1.1. Motivation	11
1.2. Objectives.....	13
1.3. Outline and Design of the Thesis	13
2. Overview of Indoor Data Collection Techniques.....	15
2.1. State-of-the-Art Sensors for 3D Data Collection.....	16
2.1.1. Laser Scanners.....	17
2.1.2. 3D Range Cameras	22
2.2. The Registration Problem.....	31
2.2.1. Registration Using Point Correspondences in the Point Clouds	31
2.2.2. Registration by the Estimation of the Sensor Pose.....	33
3. Data Collection using Microsoft Kinect for Xbox 360	36
3.1. Point Cloud Collection by Kinect.....	36
3.1.1. System Interfaces and SDKs	36
3.1.2. System Calibration	36
3.1.3. Generation of Colored Point Clouds	39
3.2. Point Clouds Registration.....	42
3.2.1. Point Clouds Registration Based on RGB and Depth Information	42
3.2.2. Point Clouds Registration Based on an Indoor Positioning Solution and Available Coarse Indoor Models	43
3.3. Kinect SWOT Analysis	49
4. Overview of Available Indoor Modeling Approaches	50
4.1. Classification of Available Modeling Approaches.....	51
4.2. Iconic Approaches.....	52
4.2.1. Image-Based Modeling	52
4.2.2. Range-Based Modeling	57
4.2.3. Modeling Based on Architectural Drawings	60
4.3. Symbolic Approaches.....	63

5. Automatic Reconstruction of Indoor Spaces.....	65
5.1. Point Cloud Pre-Processing.....	66
5.1.1. Outlier Removal.....	66
5.1.2. Downsampling.....	67
5.1.3. Noise Removal.....	67
5.1.4. Leveling the Point Cloud.....	68
5.1.5. Height Estimation and Furniture Removal.....	69
5.2. Reconstruction of Geometric Models.....	70
5.2.1. Generation of Orthographic Projected Image.....	70
5.2.2. Binarization.....	71
5.2.3. Morphological Image Processing.....	72
5.2.4. Estimation of the Lines Representing the Walls in 2D.....	73
5.2.5. Topological Corrections.....	76
5.2.6. 2D to 3D Conversion of Reconstructed Models.....	81
6. Experimental Results and Analysis.....	82
6.1. Kinect System Calibration and Accuracy Analysis.....	82
6.1.1. System Calibration.....	82
6.1.2. Accuracy of Kinect Range Measurements.....	85
6.2. Evaluation of the Reconstruction Approach.....	88
6.2.1. Parameter Selection in Different Scenarios.....	88
6.3. Quality of the Reconstructed Models.....	93
7. Application in the Refinement of Available Coarse Floor Models.....	95
7.1. Registration of Individual Detailed Models to an Available Coarse Floor Model.....	96
7.1.1. Approximate Registration.....	96
7.1.2. Fine Registration.....	97
7.2. Fusion of Detailed Models to the Coarse Model.....	99
8. Conclusion.....	103
8.1. Summary.....	103
8.2. Contributions.....	103
8.3. Future Work.....	104
Appendix A. Point Cloud Registration – Fundamental Principles.....	106
A.1. Closed-Form Solution.....	107
A.2. Iterative Solution (ICP).....	109
Appendix B. RANSAC.....	112
Appendix C. SLAM Problem.....	113

Appendix D. Hough Transform	115
D.1. Standard Hough Transform	115
D.2. Progressive Probabilistic Hough Transform.....	116
Appendix E. Reconstruction of Detailed Models – Case Studies	117
References	123
Relevant Publications.....	130
Curriculum Vitae.....	131
Acknowledgment	132

1. Introduction

1.1. Motivation

Indoor modeling addresses the reconstruction of 2D and 3D CAD models of building interiors by means of surfaces or volumes. Such models can be derived from photographs by the extraction and matching of features of interest, or from point clouds by the fitting geometric primitives.

Models of buildings interior structure are demanded by many applications to support a variety of needs, from navigation to simulation. In robotics and computer vision, existence of a map or simultaneous mapping is essential for localization of the user or a mobile robot. In virtual city models, interior models constitute the levels-of-detail 4 (LOD4) models (according to OGC standard CityGML (Kolbe et al., 2005)), to support many spatial-based applications such as GIS, urban planning, risk management, emergency action planning, environmental simulation, navigation, etc.. In Building Information Modeling (BIM), which is used for supporting construction, planning, design, and maintaining infrastructures, interior models are the geometric basis of semantic information. In architecture, virtual indoor models support interior designers to have a realistic and more precise impression about spaces.

The most important challenge in the reconstruction of indoor models is the time and costs of data collection and generating such models. In practice, this task is mainly performed using manual and semi-automatic approaches, and therefore the user qualifications play an important role in the speed and accuracy of the process. According to the comparison made by Panushev and Brandt (2007), the reconstruction of average-sized building interiors takes several months, although modeling single objects can be a fairly quick task. Therefore, the automation of this process is required. This automation is still a challenge, due to the existence of clutter, complexity of the shape of the interior and challenges in the data collection.

Indoor data collection is mostly performed from ground level viewpoints, and therefore is more complex and challenging in comparison with airborne and remote data collection. Moreover, data collection platforms delivering high accuracy data (e.g. Terrestrial Laser Scanners (TLS)) are usually heavy and expensive, and therefore large-scale data collection is time consuming and costly. However, development of low-cost range measurement sensors has recently increased the focus on range-based indoor mapping. According to Luhmann et al. (2014), the mass market effect of the consumer-grade 3D sensing camera Microsoft Kinect (over 10 million units in circulation), had a significant impact on the photogrammetric community where the number of 3D sensing systems is in the range of 1000s. The registration of the point clouds collected by such low-cost and handheld systems is also an active research area; as will be seen later, this task can be a challenge in scenarios having a poor texture or insufficient geometrical features. Presented works by Henry et al. (2012), Newcombe et al. (2011), Whelan et al. (2013) consider the Kinect a suitable platform for a fast and affordable data collection. Google Project Tango, Structure Sensor and DPI-7/8 are examples of commercial solutions developed so far, for the collection of 3D data from building interiors, as the user walks through space. For the registration of the collected point clouds, the systems benefit from the geometric information extracted

from the range images, or observations made in color image space, or a combination of both information for an accurate pose estimation. Therefore, the systems turned to be fragile in scenarios that the mentioned sources of information are not available or insufficient, such as scenes with low visual or geometrical features (e.g. hallways). Therefore, other sources of information and new strategies shall be considered to fill the gap in the available registration approaches.

Despite the fact that indoor data collection has already been studied by many researchers, and is facilitated due to advances in sensor technology and vision algorithms, less attention is still paid to the reconstruction of CAD models based on the collected data. Moreover, although some reconstruction approaches are already available, the quality and density of the collected data by low-cost sensor systems are not always consistent with the assumptions made by the approaches. In other words, affordability comes with loss of quality and trade-offs; data collected by low-cost sensor systems are subject to more noise, gaps and other artifacts that make the reconstruction process more challenging than before. Due to the complexity of indoor scenes, existence of gap and clutter, and extreme conditions for the registration of collected point clouds, still a general and fully automatic indoor reconstruction approach does not exist. Available approaches rely either on some level of user interaction, or make assumptions regarding the room shapes, quality of the collected data, etc. Commercial software solutions such as Leica Cyclone and Leica CloudWorx are widely used for modeling from the collected point clouds; however, they are based on a high level of user interaction. A strategy for the automation of this process is proposed for instance by Budroni and Böhm (2009) using a linear and rotational plane sweeping algorithm, however, under the assumption that the walls are parallel or perpendicular to each other (Manhattan-world scenario). Moreover, the ceiling and floor points have to be collected in this modeling approach (for the cell decomposition process), which is a challenge for low-cost mobile mapping systems, due to the poor texture and 3D information required for the registration of the point clouds captured from different viewpoints. Another example of automatic reconstruction of indoor scenes is presented by Previtali et al. (2014), based on the RANSAC algorithm for the extraction of planar features. Although this algorithm can model rooms with more general shapes, still the collection of floor or ceiling points for the cell decomposition is necessary. Another category of approaches converts the modeling problem from 3D to 2D, and extract line segments corresponding to walls by processing images derived from the projection of points onto the ground plane. Okorn et al. (2010) use the Hough transform for this purpose; however, the resulting 2D plan does not represent a topologically correct model. Adan and Huber (2011) use a similar approach, but add more semantic information into the models and deal with occlusions using a ray-tracing algorithm, assuming 3D data is collected from fixed and known locations. Valero et al. (2012) further improve the results using a more robust line detection algorithm and considering some topological analyses. However, this approach requires a dense and high quality input point cloud, which is a challenge to fulfill using low-cost sensor systems.

Therefore, new approaches are required to fill the gap between the new data collection strategies and available reconstruction approaches, by making fewer assumptions regarding the point cloud quality, data collection strategy and different room shapes, and at the same time dealing with the gaps in the data.

1.2. Objectives

Regarding the mentioned gaps in the previous section, this work aims at increasing the automation level, and at the same time the performance of the reconstruction process (i.e. modeling arbitrary shapes with a higher level of detail), with a focus on the data collected by low-cost sensor systems. For this purpose, the following objectives shall be fulfilled in this study:

Investigation on indoor data collection using low-cost sensor systems: In this part of the work, state-of-the-art sensor systems used for the collection of 3D data in indoor scenes shall be investigated. A suitable sensor system shall be selected as the case study, and the registration of the collected point clouds by this sensor has to be studied in different scenarios.

Defining a robust and efficient reconstruction approach: In this part of the work, topologically correct models have to be automatically reconstructed from the point clouds collected by the selected low-cost sensor system in the previous part. Furniture and clutter have to be removed from the point cloud automatically, or with a minimal user interaction. The reconstruction approach shall be capable of dealing with the noise and occlusions contained in the collected data; strategies have to be defined to compensate such effects. Moreover, the approach shall include modeling of more general shapes of the building interiors (not only Manhattan-world scenarios). It is also required to reconstruct available larger gaps (e.g. those caused by the existence of windows), using available sources of information, such as architectural drawings and available floor plans.

Investigation on update and refinement of available coarse floor models: As-designed building models and available floor plans do not necessarily represent the actual state of the building interiors (as-built models). For many indoor applications, such models and plans have to be verified, updated or refined, in order to fulfill the required accuracies. Low-cost data collection approaches have great potential for a fast and efficient fulfillment of this task, if a suitable reconstruction and fusion algorithm is available. This shall be investigated within the study as well.

1.3. Outline and Design of the Thesis

In order to fulfill the required tasks mentioned in the previous section, the thesis is structured within the next seven chapters, as follows.

Chapter 2 presents state-of-the-art sensors used for 3D data acquisition in indoor scenes, together with available approaches used for the registration of the data collected from different viewpoints.

In chapter 3, Microsoft Kinect is selected as the case study; the mathematical background for the system calibration and generation of colored point clouds from disparity and color images is presented in this chapter. Challenges regarding the data collection and registration are discussed in this chapter, and a new complementary approach for the registration of the point clouds is proposed.

Chapter 4 presents state-of-the-art indoor reconstruction approaches, based on different sources of input data. Iconic (bottom-up) approaches use real measurements, mainly derived from images and range data. In contrast, symbolic (top-down) approaches support indoor reconstruction based on hypotheses, in case of having incomplete or erroneous data.

Chapter 5 presents the proposed approach for the reconstruction of indoor spaces from the collected point clouds using a pilot study.

Experimental results are presented in chapter 6. The chapter starts with the system calibration and accuracy analysis of the range measurements by Kinect, and then continues with the performance evaluation of the reconstruction approach in different scenarios.

Chapter 7 aims at the refinement of available coarse floor models by the fusion of the detailed model of individual rooms. Larger gaps in the detailed models (e.g. those caused by the existence of windows) are reconstructed here, as a byproduct of the fusion process, using a proposed learning-based approach.

Chapter 8 concludes the presented work with a summary of the achieved results and contributions. It further suggests research areas, in which more investigation is required to increase the performance of the proposed system and improve achieved results.

2. Overview of Indoor Data Collection Techniques

For the reconstruction of building interiors geometrical information has to be provided. Depending on the application and required accuracy, different sensor systems can be employed for this purpose. Figure 2.1 presents a classification of available non-contact 3D data collection methods based on light waves. This chapter only presents state-of-the-art sensors used for the collection of 3D data in indoor mapping applications with more focus on low-cost solutions, together with the available techniques used for the registration of data collected from different viewpoints.

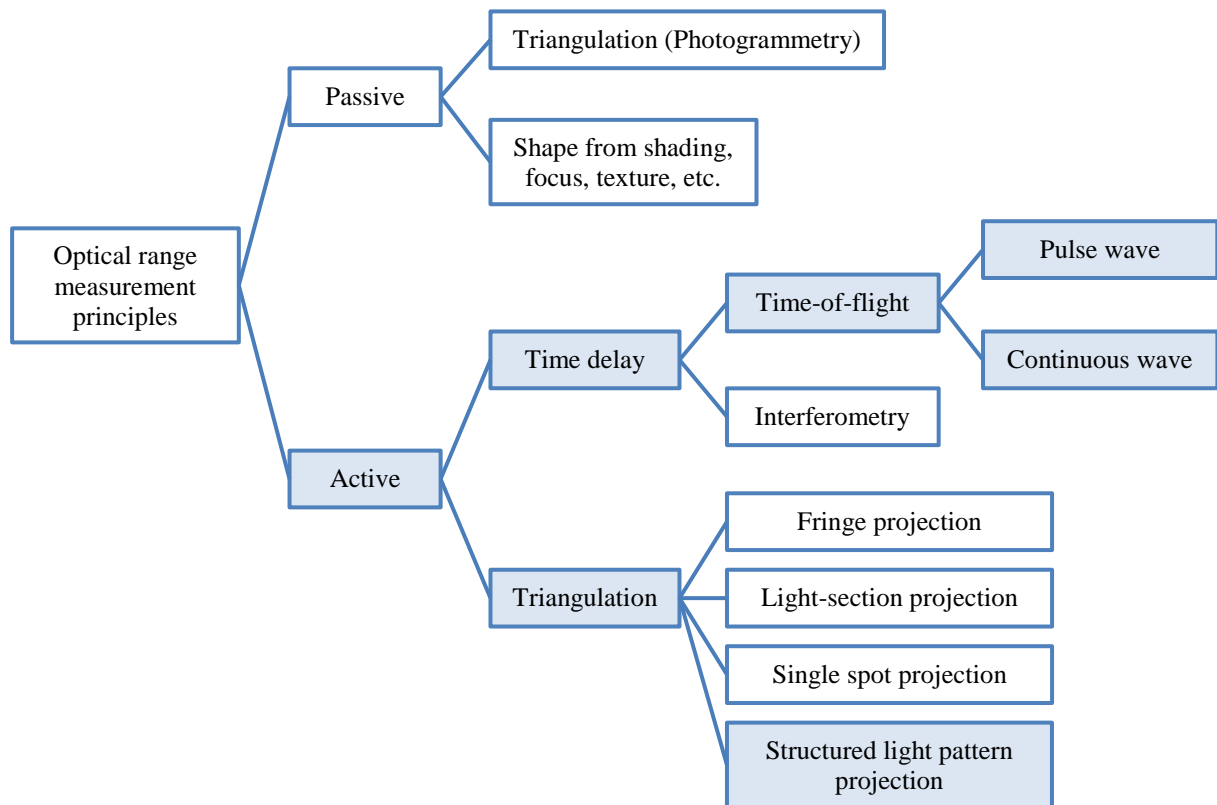


Figure 2.1 – Classification of available non-contact 3D data collection methods based on light waves. Methods which are typically used for the collection of building interiors data are highlighted. (Adapted from Luhmann et al. (2014) and Remondino and El-Hakim (2006))

2.1. State-of-the-Art Sensors for 3D Data Collection

Sensor systems used for 3D data acquisition in indoor scenes are divided to two main categories, based on their sensing principle: passive and active systems.

Passive Systems

Passive triangulation systems provide 3D information by measuring and analyzing the 2D image coordinates of interest points, collected from multiple viewpoints (see figure 2.2). In close range photogrammetry, solid state sensor cameras such as SLR-type cameras, high resolution cameras and high speed cameras are certainly the most popular passive systems (Maas, 2008). Passive systems are highly dependent on the ambient light conditions and the visual texture. The derivation of 3D information requires post-processing efforts; however, the systems are low-cost, portable and flexible to use.

The second type of passive systems rely on visual qualities such as texture, focus, shading and light intensity to estimate surface normal vectors and therefore, the shape of the surface. For example, shape-from-shading techniques recover the shape from the variation of shading in the image. This requires recovering the light source in the image, which is a difficult task in real images, and requires simplifications and making assumptions regarding the light conditions. Moreover, as also stated by Zhang et al. (1999), even with such assumptions, finding a unique solution to the corresponding geometrical problem is still difficult, since the surface is described in terms of its normal vectors, and additional constraints are required. In general, this category of passive approaches is not suitable in indoor modeling applications, and is mentioned here only for the completeness.

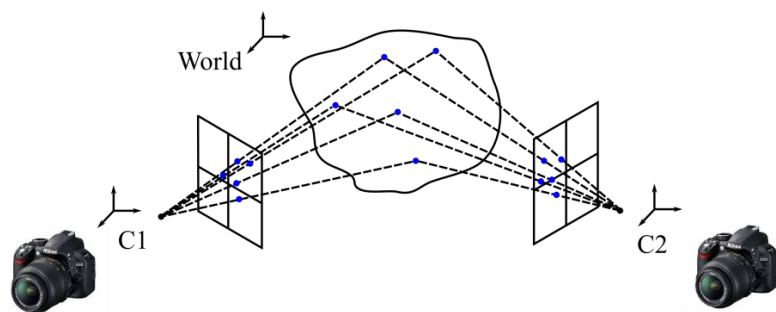


Figure 2.2 – Passive triangulation principle.

Active Systems

Active systems rely on their own illumination and deliver 3D information (range images and point clouds) without requiring post processing efforts by the user, and therefore are more suitable for automation purposes. Since the systems do not rely on the visual appearance of the objects and provide their own features to be measured, they are well suited for measuring textureless surfaces, which is the case in many indoor spaces.

Advances in sensor design and technology as well as vision algorithms and computational capabilities have resulted in portability, cost reduction and performance improvements of active range measurement systems. In indoor reconstruction applications, not only terrestrial laser scanners have become slightly less expensive and smaller than before, but also other solutions have been optimized for the collection of 3D data, such as time-of-flight cameras and triangulation systems using projected

light patterns. In the following section, popular and state-of-the-art systems used for the 3D data collection of indoor spaces are introduced.

2.1.1. Laser Scanners

2.1.1.1. Terrestrial Laser Scanners

Terrestrial laser scanners (TLS) are increasingly used to capture accurate and dense 3D data in many applications, from the recording of building interiors to the documentation of heritage sites. They can collect thousands to hundreds of thousands of points per second with millimeters accuracy.

Distance measurements in terrestrial laser scanners are realized based on two methods: estimation of light travel time and triangulation. The light travel time can be measured directly using pulse wave time-of-flight (TOF) measurement, or indirectly by phase measurement in continuous wave lasers. Short range laser scanners use triangulation principle for the range measurements, and are typically used in industrial applications, where the object distance is less than 1m. Triangulation-based scanners are not of interest in this study.

Time-of-Flight Measurement Principle (Short Laser Pulse)

The light velocity is constant in a given medium. In vacuum, the accepted value for the light velocity is 299 792 458m/s. In other mediums, the light velocity is related to this value using a correction factor called the refraction index. Therefore, by knowing the light velocity in the medium and estimating the light travel time (from a source to the object surface, and back to the source), the object distance is estimated by the following equation (see figure 2.3):

$$d = \frac{c}{n} \cdot \frac{\Delta T}{2} \quad (2.1)$$

where, d is the distance between the source and the object, c is the light velocity in vacuum, n is the refraction index of the medium and ΔT is the light travel time. As mentioned by Beraldin et al. (2005), the range measurement uncertainty is related to the time measurement uncertainty and the signal-to-noise ratio (SNR) by equation (2.2).

$$\delta d = \frac{c}{n} \cdot \frac{\delta \Delta T}{2\sqrt{\text{SNR}}} \quad (2.2)$$

Therefore, assuming $\text{SNR} = 100$ and $\delta \Delta T = 1\text{ns}$, the range measurement uncertainty will be 15mm. In case of having N independent measurements, the uncertainty reduces by a factor proportional to the square root of N . However, increasing the number of measurements has applicability limitations in scanning methods (Beraldin et al., 2005; Vosselman and Maas, 2010).

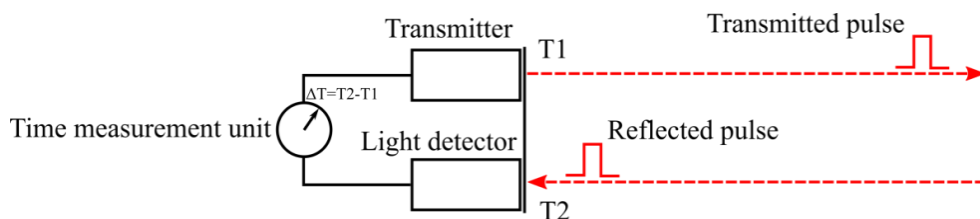


Figure 2.3 – Pulse wave TOF measurement principle.

As mentioned by Beraldin et al. (2005) and Vosselman and Maas (2010), most of the pulse wave TOF laser scanners provide an uncertainty of a few millimeters in the range measurements up to 50m, as long as a high SNR is maintained. However, as mentioned by Beraldin et al. (2010), exact and accurate measurement of the pulsed laser arrival time is a challenge, due to the difficulties in the detection of the time trigger in the returned echo. For example, if the pulse is time-triggered at the maximum amplitude, the detection of the time trigger will be difficult if the returned echo provides more than one peak. The detection threshold can also be set to the leading edge of the echo, but on the other hand the threshold will be strongly dependent on the echo's amplitude, which is subject to change due to the light attenuation nature in the atmosphere. Another method which is proven to be more suitable is the constant fraction (Wagner et al., 2004), in which the trigger is typically set to 50% of its maximum amplitude.

Phase Shift Measurement Principle (Continuous Wave)

Besides the direct measurement of the TOF, the estimation of the light travel time can also be realized indirectly by the measurement of the phase difference between the original and returned waveforms using amplitude modulation (AM) or frequency modulation (FM) techniques. The phase difference between the two waveforms is related to the time delay and therefore to the corresponding distance by equations (2.3) and (2.4) (see figure 2.4).

$$\Delta t = \frac{\Delta\phi}{2\pi} \cdot \frac{n \cdot \lambda_m}{c} \quad (2.3)$$

$$d = \Delta\lambda = \frac{c}{n} \cdot \Delta t, \quad d_{\max} = \frac{\lambda_m}{2} \quad (2.4)$$

in which, d is the distance equivalent to the phase shift (the absolute distance is the summation of this distance and a multiplication of the full wavelength), $\Delta\phi$ is the phase shift and λ_m is the wavelength of the modulated beam (c/f_m). As mentioned by Beraldin et al. (2005), the distance uncertainty in case of AM is given approximately by:

$$\delta d = \frac{1}{4\pi} \cdot \frac{\lambda_m}{\sqrt{\text{SNR}}} \quad (2.5)$$

As it can be seen in the equation, a low frequency f_m results in a less precise range measurement. Therefore, using blue opposed to a near-infrared laser will decrease the range measurement uncertainty. However, reducing the wavelength (increasing the frequency) will limit the operating range of the system, due to the faster attenuation of high frequency waves.

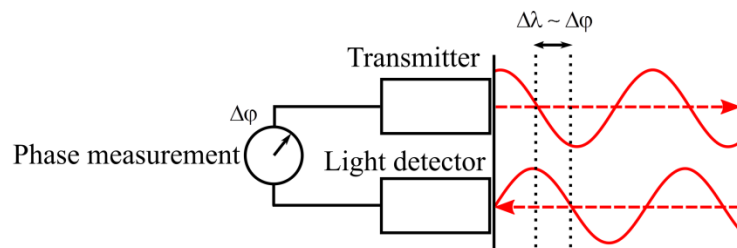


Figure 2.4 – Continuous wave phase shift measurement principle.

Since the returned signal cannot be associated with a specific part of the original signal, the calculated distance is not the absolute distance between the source and the object, but a fraction of the full wavelength. The absolute distance is obtained by the summation of this value with a multiplication of the full wavelength, also known as the ambiguity interval. The ambiguity interval cannot be purely resolved by the phase shift measurement, and therefore, using multiple measurements with different modulation frequencies is required. As mentioned by Guidi and Remondino (2012), continuous wave solutions use two or three different modulation frequencies: a low modulation frequency for a large ambiguity interval, and higher modulation frequencies for increasing the angular resolution and therefore the resolution of the range measurements. By increasing the number of steps between the low and high frequencies, the FM technique is realized. This has the advantage of reducing the measurement uncertainty level, which is less than that of pulse wave devices (typically in range of 2-3mm), as well as continuous wave devices with two or three modulation frequencies (typically 1mm at a proper distance). Such devices are mostly used in industrial and cultural heritage applications. According to Beraldin et al. (2005), The distance measurement uncertainty for such devices is approximately given by:

$$\delta d = \frac{\sqrt{3}}{2\pi} \cdot \frac{c}{\Delta f} \cdot \frac{1}{\sqrt{\text{SNR}}} \quad (2.6)$$

where, Δf is the frequency excursion (Skolnik, 1980).

According to Guidi and Remondino (2012), continuous wave systems provide smaller distance measurement uncertainties in comparison with pulse wave systems due to two reasons: a) since the light is sent to the target continuously, more energy is sent to the target and therefore a higher SNR is provided; b) the low-pass filtering used for the extraction of the signal further reduces the noise. However, limitations caused by resolving the ambiguity interval make the operating range of such systems smaller than pulse wave systems.

A large number of commercially available laser scanners operate based on pulse wave TOF measurements. Such measurements operate at longer distances, but on the other hand are less sensitive with respect to the object surface variations and small details. Moreover, the measurement rates are usually about one order of magnitude slower than phase shift scanners. However, state-of-the-art pulse wave TOF laser scanners such as Leica Scanstation P20/30/40 have overcome the speed limitation, and can measure up to one million points per second even with TOF technology.

Regarding the application, range of operation, measurement principle, demanded accuracy and price, different models of laser scanners are commercially available. Table 2.1 presents some of the popular state-of-the-art models of available laser scanners used in surveying and photogrammetric tasks based on TOF and phase shift measurement principles. Amongst the different models of the scanners, RIEGL VZ series are made specially for long range measurements. Depending on the model, the measurement range in RIEGL VZ series varies from 400m (VZ400, ca. 75K€) up to 6000m (VZ-6000, ca. 150K€); this extended range is suitable for topographical, mining and archaeological applications. Z+F and FARO laser scanners are based on phase shift measurements, and therefore provide a very high measurement rate. Before the release of the Leica P20/30/40 series (TOF laser scanners), Z+F laser scanner used to be the only TLS in the market which could measure about one million points per second. FARO Focus^{3D} X130 and X330 models provide a similar measurement rate, however, with smaller weight and price, which makes the scanners very popular for many indoor and outdoor applications. Although the captured data by TLS is of high quality and density, the price of such devices is usually too high to be accessible and used by public. In practice, the task of indoor data collection along with 3D reconstruction, which is required for generating BIMs, is usually performed by professional service providers ("U.S. General Services Administration," 2009).





Laser scanner				
Manufacturer	Leica Geosystems	RIEGL	Zoller+Fröhlich	FARO
Model	Scanstation P40	VZ-400	Imager 5010C	Focus ^{3D} X330
Measurement Principle	TOF (pulsed laser)	TOF (pulsed laser)	Phase shift	Phase shift
Measurement rate (PPS)	Up to 1Mio	Up to 122K	> 1Mio	Up to 976K
Field of view (H×V)	360°×270°	360°×100°	360°×320°	360°×300°
Measurement range	0.4m - 270m	1.5m – 600m	0.3m - 187m	0.6m - 330m
Accuracy of single point measurement (1σ)	0.4mm @ 10m 0.5mm @ 50m	5mm @ 100m	0.3mm @ 25m 1.6mm @ 100m (80% reflectivity, 127K points/sec)	Up to ± 2mm 0.3mm @ 10-25m (90% reflectivity, 122K points/sec)
Weight of the scanner	12.5kg	9.6kg	11kg	5.2kg
Price of the scanner (€)*	N. A.	Ca. 75K	Ca. 65K	Ca. 50K

Table 2.1 – Examples of typical models of terrestrial laser scanners with their technical specifications from the company product information (images adapted from the corresponding company website). *Non-official prices in Germany, March 2015.

2.1.1.2. 2D Scanning Laser Range Finders (LRFs)

In robotic applications, the perception of the environment is required. This is usually fulfilled by the use of inexpensive 2D scanning laser range finders (LRF), as an alternative to 3D laser scanners which are not cost-effective for many applications. Such devices can provide accurate and high resolution data in 2D, with a wide field of view and large measurement range, useful for mapping, obstacle avoidance, feature detection and self-localization applications. Figure 2.5 depicts an exemplary 2D range image derived by a 2D laser range finder. The range estimation in LRFs is realized based on pulse wave TOF or phase shift measurements (technically simpler than TOF), although nowadays due to advances in sensors technology, TOF measurements are accepted as the standard technique (Chli et al., 2015).

In robotic applications, the most popular used LRFs are those offered by SICK and Hokuyo companies. The price of the products ranges between a few hundred to a few thousand Euros, depending on the detectable range, precision and resolution. Therefore, each type is preferred for a special application. For instance, systems such as Hokuyo URG-04LX-UG01 and SICK TiM551 are more suitable for obstacle detection and avoidance, but not optimal for mapping purposes, due to their low angular and range resolution. For more detailed and high resolution mapping applications, more accurate products such as Hokuyo UTM-30LX and SICK LMS511 (largest SICK LRF) are usually preferred. The mentioned LRF models together with the corresponding technical specifications are presented in table 2.2.

Laser range finder				
Manufacturer	SICK	SICK	Hokuyo	Hokuyo
Model	LMS511	TIM551	URG-04LX-UG01	UTM-30LX
Scan time	13msec/scan	67msec/scan	100msec/scan	25msec/scan
Angular field of view	190°	270°	240°	360°
Angular resolution	0.25°	1°	0.36°	0.25°
Operating range	0m - 80m	0.05m - 10m	0.02m - 4m	0.1m - 60m
Systematic error	25mm (1m - 10m) 35mm (10m - 20m)	60mm	N. A.	N. A.
Statistical error	7mm (1m - 10m) 9mm (10m - 20m)	20mm	30mm (0.02m - 1m) 3% (0.02m - 4m)	30mm (0.1m - 10m) 50mm (10m - 30m)
Dimensions (W×D×H) [mm]	160×155×185	60×60×86	50×50×70	60×60×87
Weight	3.7kg	250gr	160gr	370gr
Price (€)*	Ca. 6100	Ca. 1700	Ca. 1200	Ca. 4800

Table 2.2 – Examples of the most popular laser range finders (technical specifications and adapted images from the corresponding company website). *Non-official prices in Germany, March 2015.

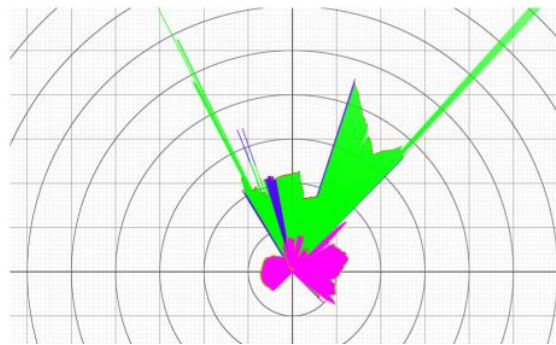


Figure 2.5 – An exemplary 2D range image derived by Hokuyo URG-04LX-UG01 laser range finder. Colors indicate the intensity of the reflected beams. (adapted from “UrgBenri Information Page” (2015))

2.1.1.3. Indoor Mobile Mapping Systems Based on Laser Scanners

Indoor Mobile Mapping Systems (IMMS) have enabled a fast 3D data collection of large building interiors using kinematic platforms. For the positioning purpose, opposed to the outdoor mobile mapping systems that use GNSS solutions, these systems mostly use Simultaneous Localization and Mapping (SLAM) methods. In most IMMS, in order to achieve a cost-effective solution, 3D maps are created by a single tilted or multiple 2D laser scanners mounted on the system. Commercial solutions such as i-MMS (by VIAMETRIS), ZEB1 (by CSIRO) and MID (supported by VIAMETRIS) are examples of state-of-the-art IMMS based on 2D laser scanners.

i-MMS: This system consists of a mobile platform, 3 Hokuyo laser scanners (1 for positioning using SLAM and 2 for the data collection), a Point Grey Ladybug spherical camera and batteries.

ZEB1: This system uses a handheld platform, 1 Hokuyo laser scanner, a low-cost IMU and a computer. The performance of *i-MMS* and *ZEB1* is investigated and compared by Thomson et al. (2013). The comparison shows that *i-MMS* generates higher quality point clouds, although both systems deliver results in centimeters accuracy, and therefore inadequate for surveying applications requiring millimeters accuracy.

MID: This system features a Hokuyo laser scanner, a 5Mpx fisheye camera, an SBG-Systems AHRS (Attitude and Heading Reference System, consists of set of three MEMS based gyroscopes, accelerometers and magnetometers) and a tablet PC. The integrated positioning solution provides up to 1cm absolute accuracy, while the laser scanner delivers measurements with 3cm accuracy (0.1m - 10m) (“MID Brochure,” 2014).

To achieve millimeters accuracy, the use of more expensive laser scanners in IMMS is inevitable; an example is the TIMMS system offered by Trimble-Applanix. The use of indoor mobile mapping systems is the optimum solution for the data acquisition in large public buildings such as railway stations and airports, in which the measurement range is usually too high for the low-cost systems, or the data acquisition shall be performed faster than usual static laser scanning. The mentioned mobile mapping systems are depicted in figure 2.6.



Figure 2.6 – Examples of commercial indoor mobile mapping systems. Left to right: Trimble-Applanix TIMMS, VIAMETRIS *i-MMS*, CSIRO *ZEB1* and VIAMETRIS *MID*. (images from the corresponding company website)

2.1.2. 3D Range Cameras

As an alternative solution to the abovementioned laser-based systems, one can use range cameras to capture the scene 3D information using CMOS or CCD technologies at high frame rates, based on TOF or triangulation principles.

2.1.2.1. Time-of-Flight (TOF) Cameras

TOF cameras measure the distance based on either timing of pulse, continuous wave modulation or signal gating, using the so called PMD (Photonic-Mixer-Device) sensors. Each PMD sensor has an

LED light emitter and a CMOS sensor. Each CMOS pixel, depending on the measurement principle, estimates the time delay between the emission and arrival of the signal. This enables 3D imaging without the need for scanning (Thorsten and Hagebecker, 2007). Technical details regarding the cameras' components and the measurement principles are not of interest in this study; interested readers may refer to Buxbaum et al. (2002), Kraft et al. (2004), as well as Sell and O'Connor (2014).

TOF cameras initially had very small resolutions; for instance the effector-PMD product introduced in 2005 has only 1 pixel resolution, used for the distance measurement in industrial applications. However, advances in micro-optics and microelectronics caused the development of TOF cameras with better performances and higher resolutions. According to Kolb et al. (2009), the development of TOF cameras from 2006 to 2008 shows an increase by factor of 8 or 9. MESA SwissRanger 4000 introduced in 2008 is the first commercial-grade TOF camera which has a resolution of 176 by 144 pixels. Another popular TOF camera PMD CamCube introduced in 2009 has a resolution of 204 by 204 pixels. Some of the most widely used TOF camera models together with their technical specifications are presented in table 2.3.

TOF cameras are not intended to be used in applications requiring high measurement accuracies. The main advantage of the cameras is the ability of delivering frame-based real-time measurements. This is required by applications dealing with object detection and recognition at very high frame rates, such as industrial, automotive (car comfort and safety), robotics, gaming and security applications. The cameras are also used in indoor localization and mapping applications requiring centimeters accuracy (Hong et al., 2012; May et al., 2009). However, in general they are not an optimal solution for indoor mapping applications, due to their high level of noise, small field of view and low resolution.

Different studies have investigated the calibration of TOF cameras by modeling the systematic errors contained in the range data. For instance, the study presented by Lindner et al. (2008) shows that one may expect a systematic error of 5-15cm and a noise of 5cm in the range data measure by the PMD CamCube camera. However, the systematic errors can be modeled and removed by B-splines (Lindner et al., 2008) or harmonic series (Pattinson, 2010).




Range camera			
Manufacturer	IEE	MESA Imaging	PMDTechnologies
Model and release date	3D-MLI Sensor (2008)	SwissRanger 4000 (2008)	CamCube 2.0 (2009)
Resolution	61×56	176×144	204×204
Operating range	7.5m	5m or 10m (optional)	7.5m
Scan rate	10 fps	10 - 30 fps	25 fps
Accuracy	2cm @ 1.5m	1cm or 1%	2cm @ 2m
Dimensions (W×D×H) [mm]	144×104×54	65×65×76	194×80×60 optics

Table 2.3 – Examples of TOF cameras. (adapted images and technical specifications from the corresponding company website)

2.1.2.2. Active Triangulation Systems

The second type of the range cameras uses the fundamental trigonometric theorems to compute the object distance, and has been widely used in close range photogrammetry. Triangulation systems can be divided into two categories: passive and active. Passive triangulation systems extract and match features across multiple images taken from different viewpoints (stereo photogrammetry, see), while active triangulation systems integrate a projector into the system in order to generate structured light patterns (Maas, 2008). Figure 2.7 depicts the schematic setup of a systems based on the active triangulation principle. In this method, the camera and projector must be calibrated and spatially oriented to each other. The pattern is recorded by a CCD camera and analyzed by the integrating computer in order to compute α and β , and therefore the dimensions of the triangle using the cosine law. This yields the (X, Z) coordinates of the laser spot on the object surface using equations (2.7) and (2.8).

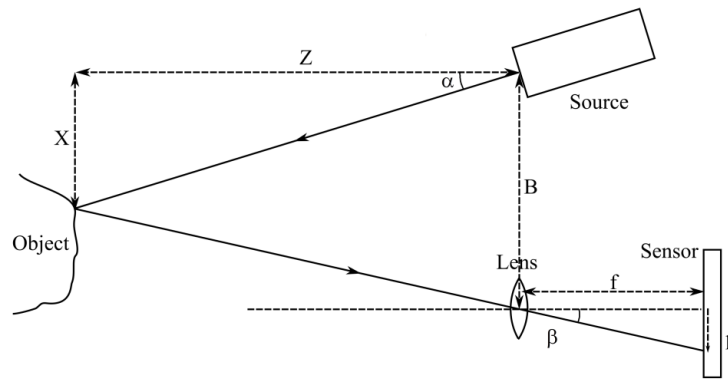


Figure 2.7 – Single point triangulation principle. (adapted from Beraldin et al. (2010))

$$B = X + Z \tan(\beta) = Z \tan(\alpha) + Z \tan(\beta) \quad (2.7)$$

$$Z = \frac{B}{\tan(\alpha) + \tan(\beta)} = \frac{B \cdot f}{f \tan(\alpha) + p} \quad (2.8)$$

In these equations Z (the perpendicular distance) is the unknown, p (the distance between the projection of the point and the principal point of the sensor), f (the effective focal length) and B (the baseline) are known (estimated by the system calibration), and α and β are measurements. According to Beraldin et al. (2010), the perpendicular distance uncertainty in this case is given by:

$$\delta Z \approx \frac{Z^2}{B \cdot f} \cdot \delta p \quad (2.9)$$

where δp depends on the type of the laser spot, peak detection algorithm, SNR (signal-to-noise ratio) and the shape of the projected spot. Since δp depends on the SNR which is proportional to the square of the object distance, the distance uncertainty in theory is proportional to the fourth power of the object distance. It makes the triangulation systems poor candidates for long-range applications, but dominant in sub-meter ranges.

The projected patterns can be of different formats, for instance stationary and dynamic fringes, light sections or speckle patterns. Figure 2.8 depicts two different types of active triangulation systems. Figure 2.8 (a) presents a fringe coded-light projection system, in which a sequence of n binary stripe patterns with $2^0 \dots 2^{n-1}$ vertical black and white stripes is projected onto the object surface, in order to assign a binary code to each pixel of the CCD camera. In figure 2.8 (b), a known pattern is projected

on the object surface. The pattern is collected by the camera and the point correspondences are found by matching the collected pattern with the reference pattern in the image, in order to recover the object surface based on the disparity measurements.

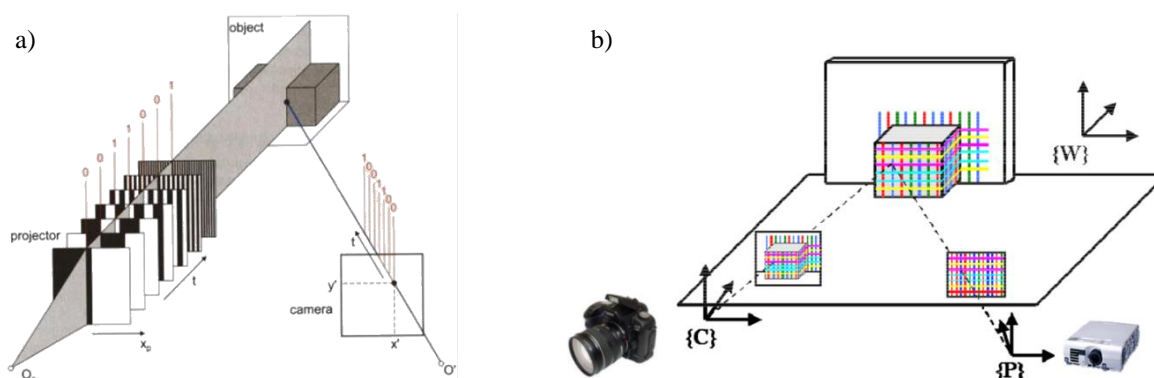


Figure 2.8 – Active triangulation systems based on: a) fringe coded-light projection (from Luhmann et al. (2014)); b) structured light pattern (from Remondino (2010)).

2.1.2.3. Low-Cost Consumer-Grade Range Cameras Based on Active Triangulation and TOF Principles

Range cameras have been employed by the gaming industry for several years in order to provide controllers based on the human gesture and natural user interactions. Companies such as 3DV System Ltd. (Yahav et al., 2007) and Optrima NV (Van Nieuwenhove, 2011) provided range cameras for game consoles based on the TOF principle. PrimeSense, the previous market leading company (now a part of Apple Inc.) released range cameras originally applied to gaming, based on the active triangulation principle. The company is best known for providing the technology to Microsoft for producing the first Kinect, previously known as Project Natal. Figure 2.9 depicts the range cameras based on the PrimeSense technology; some of them were licensed to ASUS and Microsoft. The performance of some of these sensors (in terms of accuracy and repeatability) is analyzed and compared by Böhm (2014).

Although the range imaging devices and technology have been available for several years, interest in these sensors initially remained low; interest grew with the release of Microsoft Kinect. The most important reason was the mass production of Microsoft Kinect (24 million units were sold as of February 2013 (“Microsoft News,” 2013)), which had a great effect on the photogrammetric community in which the number of traditional 3D sensing systems such as laser scanners is in the range of 1000s. The low price of this system has made it one of the most affordable and accessible systems for the collection of 3D data. (Böhm, 2014; Luhmann et al., 2014)



Figure 2.9 – Range cameras based on the PrimeSense technology. Top to bottom: Microsoft Kinect, PrimeSense PSDK, ASUS Xtion Pro Live and ASUS Xtion Pro. (from Böhm (2014))

Microsoft Kinect for Xbox 360

The Microsoft Kinect was originally developed by the PrimeSense LTD as a human interface and a hands-free game controller for Microsoft Xbox 360 game console in November 2010. Releasing the non-official and later the official Software Development Kits (SDKs) for this device opened the way for a wide range of new activities in which range cameras play an important role, such as Augmented Reality, robotics (“MS Robotics Developer Studio,” 2014), security and surveillance (“Connecting Kinects for Group Surveillance,” 2014), medicine and surgery (“GestSure,” 2014; Loriggio, 2011), etc.

Reverse engineering has determined that this RGB-D sensor system consists of an IR laser projector, an IR camera (640×480 pixels resolution at 30fps, or 1280×1024 pixels at a lower frame rate with 11-bit depth), an RGB camera (640×480 pixels resolution at 30fps, or 1280×1024 pixels at a lower frame rate with 8-bit depth), a 3-axis accelerometer for recognizing the current orientation of the Kinect and a microphone array for capturing sound (see figure 2.10). The system has a 43° vertical by 57° horizontal field of view, and performs within the range of 0.7-6m, providing centimeters accuracy in the range measurements.

The system projector emits a fix IR laser speckle pattern to the object surface (see figure 2.11 (a)). The pattern is then recorded by the IR camera which is located at a distance of about 7.5cm from the projector. The pattern consists of a 3×3 grid of light and dark speckles, with a significantly lighter speckle at the center of each grid (see figure 2.11 (b)). This special pattern design is used for the image matching technique performed by the Kinect (the algorithm is patented by PrimeSense and is not disclosed), in order to compute the disparity image by a comparison between the collected and the reference pattern. The disparity image is then converted to a point cloud using the SDKs and mathematical relationships mentioned in section 0. The accuracy analysis of the system range measurements is presented in section 6.1.2.

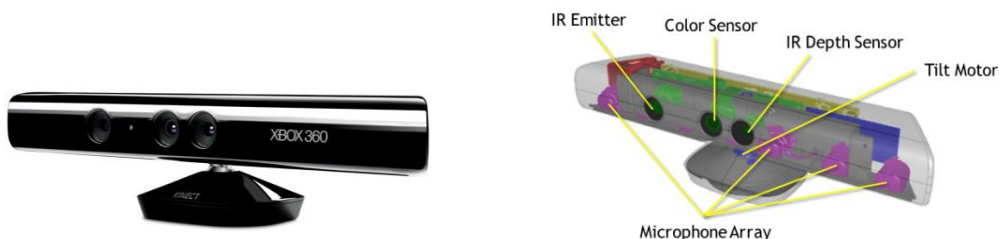


Figure 2.10 – Microsoft Kinect integrated sensors. (from (“MSDN Kinect,” 2015))

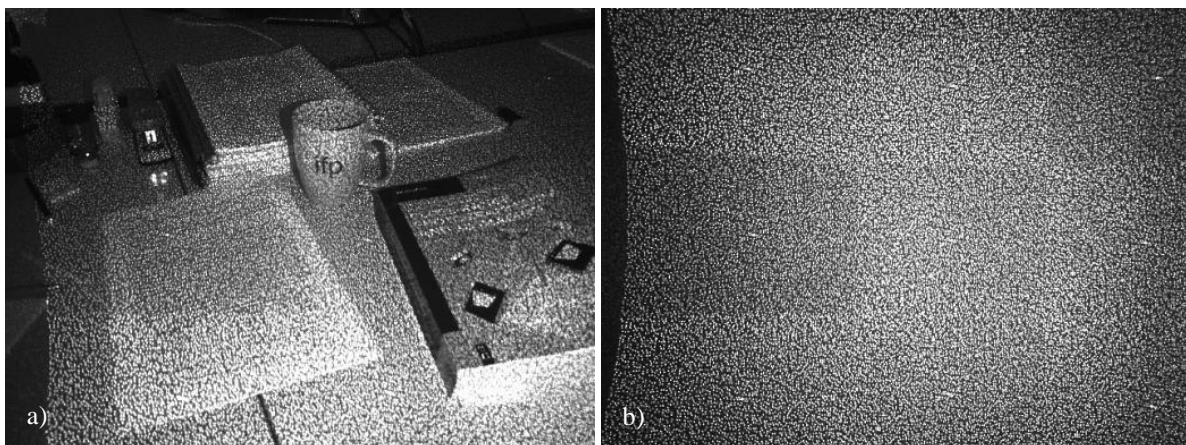


Figure 2.11 – Kinect IR laser speckle pattern projected on a real scene (left) and a flat surface (right).

Microsoft Kinect V2 for Xbox One

Opposed to the mentioned sensor systems based on the PrimeSense technology, the Kinect V2 system is based on the time-of-flight principle. This system was released in November 2013 as a motion sensing input device for Xbox One, together with an SDK for software developers. The system uses the TOF technology and chips developed by Cantesa (Bamji et al., 2015) which was acquired by Microsoft before the release of the first Kinect sensor.

The system features an RGB camera with 1920×1080 pixels resolution at 30fps, an IR emitter and an IR sensor with 512×424 pixels resolution at 30fps (see figure 2.12). The pixels in the IR sensor are divided into a top and bottom half, each driven by separate clock drivers, working with tens of MHz frequency (Bamji et al., 2015), which means increasing the depth camera's resolution to 1024×848 ("Doc-Ok.org," 2015). The performance range of the system is 0.5-4.5m, with $70^\circ H \times 60^\circ V$ field of view. The accuracy of depth measurements by this system is within 2% across all lighting, color, users, and other conditions in the operating range (Sell and O'Connor, 2014).

The system costs around 150 Euros (non-official price in Germany, March 2015); the comparison between the resolution, accuracy and price of Kinect V2 with other TOF cameras such as SwissRanger 4000 or CamCube, which cost some thousands of Euros, is noticeable. Figure 2.13 depicts a sample point cloud collected by this system.

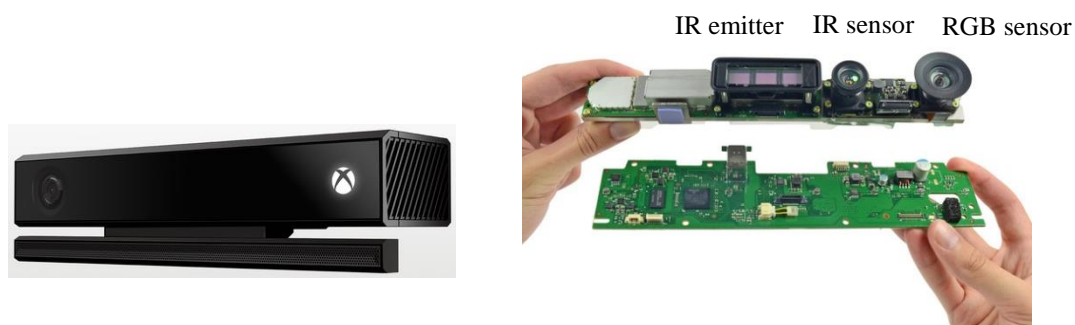


Figure 2.12 – Kinect V2 for Xbox One. (from ("iFixit," 2013))

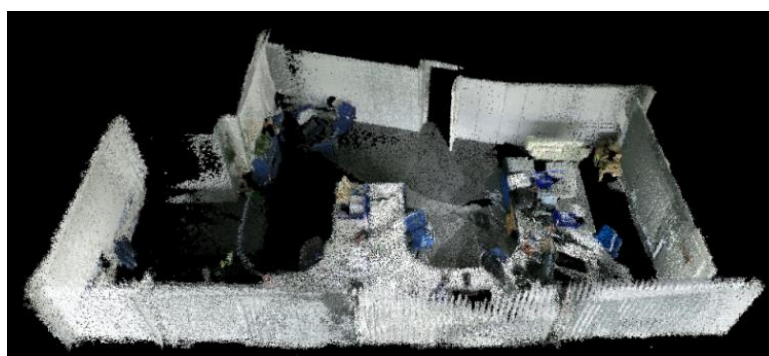


Figure 2.13 – A sample registered point cloud collected by Kinect V2 without noise removal.

2.1.2.4. Indoor Mobile Mapping Systems Based on Low-Cost Range Cameras

Inspired by Microsoft Kinect, and based on the PrimeSense active triangulation and state-of-the-art TOF technologies, low-cost commercial indoor mobile mapping systems are being developed increasingly. Examples of such systems are presented in the following parts.

DotProduct DPI-7 and DPI-8

The DPI-7 handheld scanner is developed by DotProduct LLC, and uses a PrimeSense Carmine 1.08 RGB-D sensor for the collection of range images. According to “DPI-7 User Manual” (2014), the system integrates a 7” tablet as the user interface for the data collection as well as recording and processing the data. The integrated software automatically colorizes the point clouds, and performs the localization using the scene geometrical information (similar to KinectFusion (Newcombe et al., 2011)) for the alignment of the collected range images, with the ability to re-localize the sensor in case of losing the location track. Moreover, the software filters the noise of the point cloud and adjusts the color of the collected points which might be inconsistent due to the light conditions of the corresponding color images. The tablet is additionally used to give feedback to the user regarding the quality of the collected data and location tracking, indicated by augmented colors. Figure 2.14 depicts a sample point cloud collected by this system.

The successor of this system, DPI-8, uses an 8” NVIDIA SHIELD tablet with 2GB of RAM (twice the DPI-7), which results in a higher performance, as well as the ability of capturing rooms of at least 3 times the size. The nominal accuracy of the range measurements in both systems are the same (see table 2.4). In fact, due to the use of a similar sensor, the accuracy of the range measurements is similar to the accuracy measurements captured by Kinect. The system measures depths within the range of 0.6m - 3.3m; longer distances are filtered out in order to avoid the effect of noise in longer measurements. The DPI-8 system costs about 5800€ in Germany (May 2015).

Range	Typical accuracy (RMS)	Minimum accuracy
< 1m	0.2%	0.4%
1m - 2m	0.5%	0.8%
2m-3.3m	0.8%	1.2%
> 3.3m	Not specified	Not specified

Table 2.4 – Nominal accuracy of DPI-7 and DPI-8 range measurements.

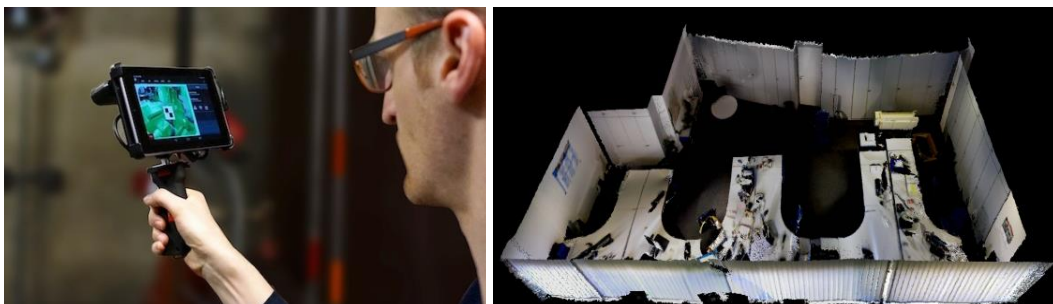


Figure 2.14 – Left: DPI-7 system (adapted from “DotProduct LLC” (2015)); Right: a sample point cloud collected by this system (noise is already removed by the integrated software).

Structure Sensor

This sensor system is developed by Occipital, and captures the 3D map of indoor spaces using a range measurement system developed by PrimeSense (active triangulation) and an integrating iPad containing the software (figure 2.15 depicts the system). The software colorizes and aligns the range images captured from different viewpoints, and creates meshes. A notable feature of this system is the SDK provided for the developers in order to enable them to write mobile applications that interact with the 3D maps, Augmented Reality, measurements on the objects, gaming, etc. Some of the technical specifications of the system are summarized in Table 2.5. The range image alignment in this system is based on the observations in the 3D object space (similar to KinectFusion (Newcombe et al., 2011)); the sensor tracking is lost in case of dealing with flat surfaces.

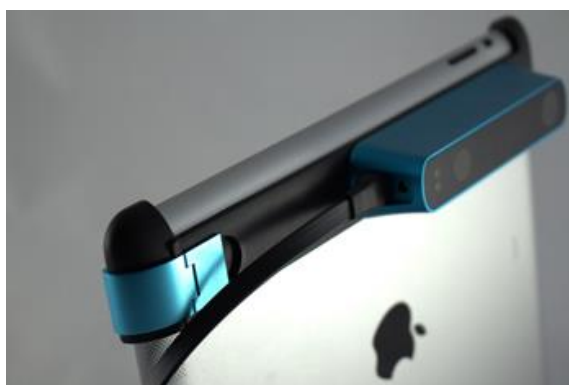


Figure 2.15 – Structure Sensor mounted on an iPad. (from the company website)

Field of view (H×V)	58°×45°
Measurement rate	30fps & 60fps
Measurement range	0.4m - 3.5m
Precision	1% of the measured distance
Weight	99.2gr
Dimensions (W×D×H) [mm]	27.9×119.2×29
Price (\$)*	379 and 499

Table 2.5 – Technical specifications of the Structure Sensor. *Official prices without iPad, in US, March 2015.

Google Project Tango

In recent years Google Inc. has shown increasing interest in indoor mapping and virtual reality. Examples of the developed systems and applications are Google backpacker (the indoor version of the Google Street View cars), Google Art project (360 degree tours of art galleries using Street View indoor technology), Google Glass (for Augmented Reality and photography) and Google Project Tango.

The Google Project Tango is an Android device platform integrating depth sensors, advanced computer vision and image processing algorithms, developed in collaboration with currently 24 universities and industrial research labs for real-time 3D mapping of interiors (“Tango Concepts,” 2015) (see figure 2.16). The system range measurement is based on the TOF principle, using a PMD sensor developed by PMDTechnologies (2015). The sensor provides a quarter of a million of measurements every second (Say hello to Project Tango!, 2014), and works best within the range of 0.5m - 4m. The device collects range images while tracking its 3D motion using a wide-angle camera working based on visual-inertial odometry techniques, in order to create the 3D map of the environment (“Tango Concepts,” 2015).

The system costs around 1000\$ (non-official price in US); currently, only a limited number of the prototypes of this product is available for researchers and software developers to develop applications and algorithms.

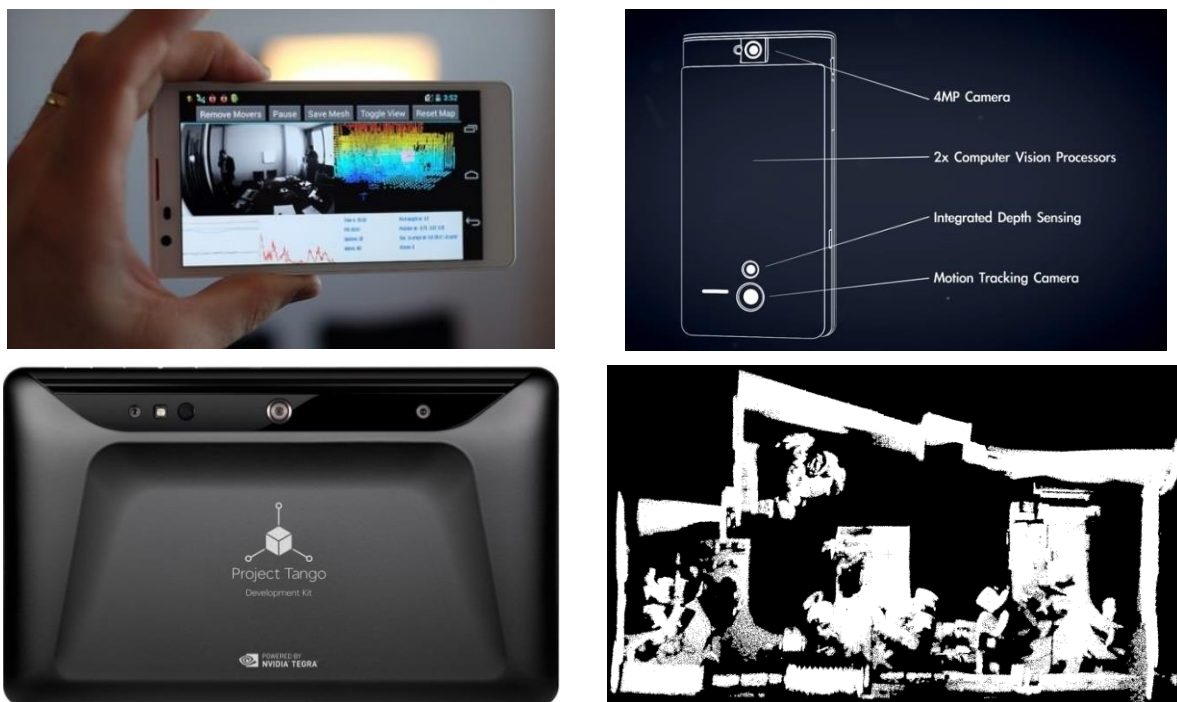


Figure 2.16 – Google Project Tango smartphone and tablet together with a sample collected data. (adapted from “Google Store” (2015), “Say hello to Project Tango!” (2014) and “The Verge” (2015))

2.2. The Registration Problem

Due to scene complexities and the scanners limited field of view, in many applications it is required to collect point clouds from multiple viewpoints in order to cover the whole scene. Point clouds collected from different viewpoints have their own local coordinate system; in order to align the coordinate systems, the corresponding point clouds have to be registered together using a rigid-body transformation, which is a special case of the 3D similarity (Helmert's 7-parameters) transformation by setting the scale factor to 1. The transformation can be estimated using point correspondences in the point clouds, or by estimating the sensor pose in the reference coordinate system.

2.2.1. Registration Using Point Correspondences in the Point Clouds

The rigid-body transformation parameters can be estimated using point correspondences in the point clouds. In case the point correspondences are already given in the form of 3D features in the scene (artificial or natural) or 2D features in the corresponding intensity or color images, the transformation parameters can be estimated for instance using a closed-form solution based on the unit quaternions (Horn, 1987; Sanso, 1973). If the point correspondences are not provided, they can be estimated based on the geometrical structure of the scene, using an iterative procedure called Iterative Closest Point (ICP) algorithm (Besl and McKay, 1992). See appendix A for the mathematical background of the two approaches.

2.2.1.1. Correspondences by Recognition of 3D Features

Artificial Targets

According to Luhmann et al. (2014), the most accurate way of registration is based on using artificial objects of known geometry in the scene, and spheres have proven to be the most reliable choice. The spheres in the scene are usually detected using the RANSAC algorithm, and their centers are used as tie points in the registration process (figure 2.17). More details about RANSAC algorithm is presented in appendix B.

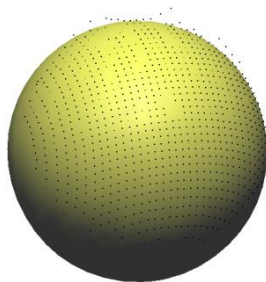


Figure 2.17 – Fitting a sphere to a set of measured points.

Natural Targets

3D features can also be defined in the scene using well-defined sharp corners manually (figure 2.18 (a)), or automatically using feature extractors such as NARF (Normal Aligned Radial Feature) (Steder et al., 2011) (figure 2.18 (b)). The NARF feature extractor works with the corresponding range images. It first identifies the interest points on the objects border (outer shape of the object from a certain perspective view), in locations where the surface is stable (robust estimation of normal vectors is possible). Then it defines a descriptor for the interest points based on the amount and the main direction of the surface changes (in terms of the surface curvature) in the vicinity of the point.

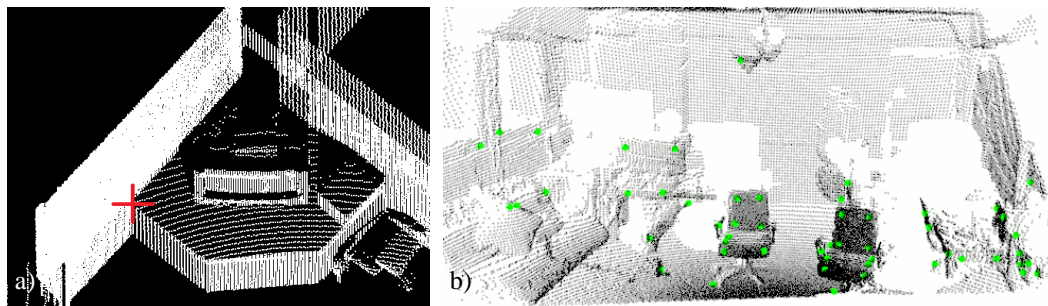


Figure 2.18 – Identification of 3D natural target points manually (left) and using NARF feature extractor (adapted from “Documentation - Point Cloud Library (PCL)” (2015)) (right).

2.2.1.2. Correspondences by the Recognition of Features in 2D Images

3D point correspondences can be identified based on the information provided by the corresponding color, intensity or reflectance image. However, as also mentioned by Luhmann et al. (2014), this requires a perfect registration of the corresponding images, which means each pixel in the color, intensity or reflectance image must correspond to the same point in the corresponding point cloud. In this case, point candidates can be derived in the 2D image space using image processing techniques (to recognize artificial targets) or 2D feature extractors such as SIFT (Lowe, 2004), SURF (Bay et al., 2006), FAST (Rosten and Drummond, 2006, 2005), etc. The extracted features then have to be matched against each other across different images. The matching process can be performed using the RANSAC algorithm, based on the rigid-body transformation model in case of using intensity images, or by the fundamental matrix in case of using color images. An example of the registration using this method is presented by Böhm and Becker (2007). They extract and match SIFT features across the corresponding reflectance images, and compute a pair-wise registration using a rigid-body transformation (see figure 2.19).



Figure 2.19 – SIFT features extracted and matched for a reflectance image. (from Böhm and Becker (2007))

2.2.1.3. Correspondences by the Analysis of the Scene Geometry – Iterative Closest Point (ICP) Algorithm

In case no point correspondences are available, or the accuracy and distribution of the available corresponding points are not sufficient for an accurate point cloud registration, one can alternatively use the Iterative Closest Point (ICP) algorithm (Besl and McKay, 1992). For each point in the local point cloud (scan world), the algorithm finds the closest points in the reference point cloud, and estimates a rigid-body transformation. After applying the transformation, the algorithm is repeated until the sum of the residuals of the distances between the point correspondences is smaller than a threshold (see figure 2.20). This registration method requires initial values; bad initial values may cause a wrong convergence of the solution. More details regarding the ICP algorithm are provided in appendix A.

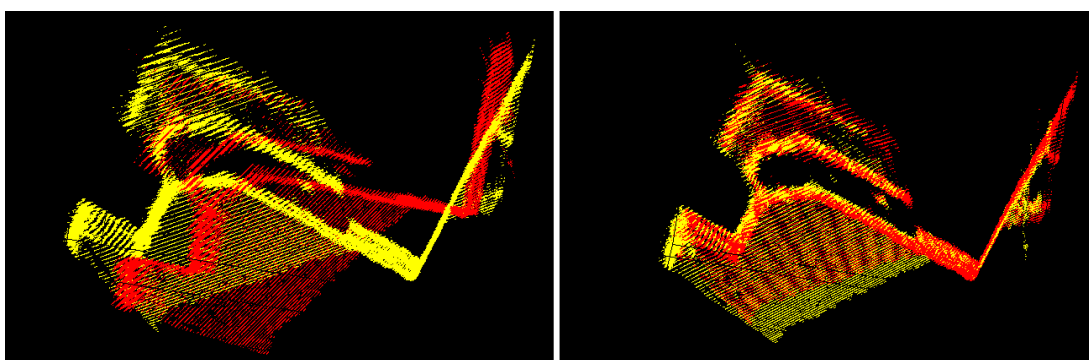


Figure 2.20 – Point cloud alignment using the ICP algorithm.

2.2.2. Registration by the Estimation of the Sensor Pose

Beside the abovementioned approaches, point clouds can be aligned if the sensor poses are estimated in a common coordinate system. The sensor pose can be estimated by the integration of different sensors such as low-cost MEMS-IMUs, LRFs and cameras into the range measurement system.

2.2.2.1. Registration Based on Structure from Motion Methods

The estimation of camera poses from two and three viewpoints has been focused for a long time by photogrammetric and computer vision communities, and closed-form solutions have been developed to solve this problem (Hartley and Zisserman, 2003). For multiple views, Structure from Motion (SfM) methods estimate the sensor pose incrementally; image features are extracted and matched for an initial image pair, the points are triangulated, and a new image is added. The solution is then globally optimized using a bundle adjustment in a post processing step. There is a wide range of SfM methods, each of which dealing differently with the large number of images, and pipelines for solving the problem (Snavely, 2008). Famous commercial software solutions are available for solving the SfM problem, such as Bundler (Snavely et al., 2006), VisualSfM (Wu, 2013), Agisoft PhotScan, etc.

SfM methods estimate the camera pose in a local coordinate system up to the scale factor. To register the point clouds, camera locations have to be first scaled to a metric coordinate system. The scale factor is estimated using a 3D similarity transformation, having point correspondences in the color and range image channels. More details regarding this registration approach is presented in section 3.2.1.

2.2.2.2. Registration Based on SLAM Methods

In real-time and robotic applications, the sensor pose is estimated using SLAM approaches. In such applications, the autonomous platform needs to localize itself within an unknown environment, while simultaneously creating the map of the environment (see appendix C). Frese et al. (2010) present an overview regarding available SLAM methods based on the application and different sensor inputs in 2D and 3D. According to this overview, in 3D applications, two general variants of SLAMs are recognized: graph-based SLAM methods that rely on scan matching, and visual SLAM methods based on point features extracted from images. Most of the graph-based SLAM methods use pair-wise alignment of the consecutive scans and create constraints for the sensor 6 degree-of-freedom (DOF). Nüchter et al. (2007) and Wurm et al. (2010) present localization and mapping methods using ICP scan matching, supported by loop closure and pose graph for the global consistency and optimization. The KinectFusion software implemented by the Microsoft Research Group (Newcombe et al., 2011) besides presenting an optimized method for the sensor tracking, creates a dense and smooth 3D map by the use of Kinect point clouds in real-time. Sensor tracking in this method is based on a GPU implementation of a coarse-to-fine ICP algorithm. Open-source implementations of this method (KinFu and KinFu Large Scale) are provided by the Point Cloud Library (PCL) (Rusu and Cousins, 2011) (see figure 2.21). Such methods, however require a suitable scene structure and enough geometric information for the successful constraining of the sensor 6 DOF, and therefore fail in case of dealing with flat surfaces.

Visual SLAM systems estimate the sensor pose by tracking sparse points of interest, extracted from images, using vision algorithms. The offline version of this problem is studied as the bundle adjustment problem in photogrammetry, and as SfM in computer vision community (Frese et al., 2010; Hartley and Zisserman, 2003; Triggs et al., 2000). According to Newcombe et al. (2011), research on SLAM has focused more on real-time marker-free tracking and mapping using monocular RGB cameras. Systems such as Parallel Tracking and Mapping (PTAM) enable marker-free tracking of the camera together with Augmented Reality applications using a single camera (Klein and Murray, 2007). This system emphasizes on the localization of the camera, and therefore performs mapping by sparse point models.

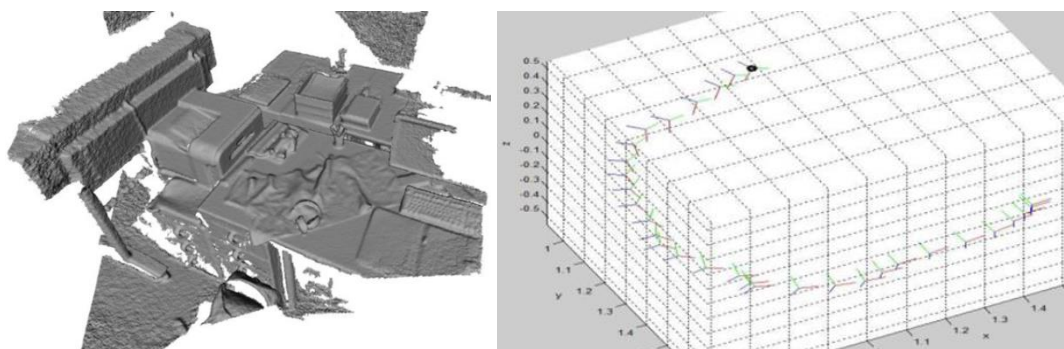


Figure 2.21 – Creating an exemplary 3D map and sensor tracking using the KinFu software provided by the PCL software library.

RGB-D sensors such as Microsoft Kinect provide range data together with corresponding color images. This enables the combination of geometric and scale information with visual features to localize the sensor and create the map of the environment. The combination of both information is specially useful for Kinect which has a relatively small field of view ($57^{\circ}\text{H}\times 43^{\circ}\text{V}$), and therefore vision-only and graph-based methods may easily fail due to finding insufficient visual or geometrical features in the scene. Henry et al. (2012) present an RGBD-ICP mapping method that tightly uses

RGB and depth information for a robust frame-based matching and loop closure. This method first extracts and matches sparse visual features (SIFT features) in two consecutive RGB images, and associates them with depth values in the corresponding depth images to generate feature points in 3D. Then it finds the best rigid-body transformation between the two sets using RANSAC algorithm. The transformation is then refined using the ICP algorithm. The ICP algorithm, however, minimizes two different Euclidean distances: the mean distance between visually associated points (sparse points) and the mean distance between dense points (Kinect point clouds), by setting different weights for each of the two distances in the error minimization process. This enables the method to benefit from the visual information when the scene geometry cannot constrain the sensor 6 DOF, or to benefit from the scene geometrical information in case of having poor visual features. The results then become globally consistent using a graph optimization process. The process is summarized in figure 2.22. A sample map created by this method is depicted in figure 2.23.

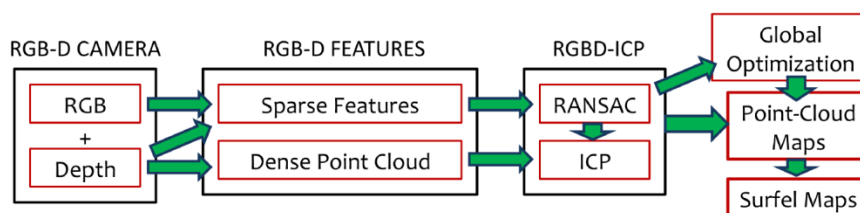


Figure 2.22 – Overview of the RGBD-ICP mapping system. The algorithm uses visually associated and dense points for frame-to-frame alignment and loop closure detection in parallel threads. (from Henry et al. (2012))

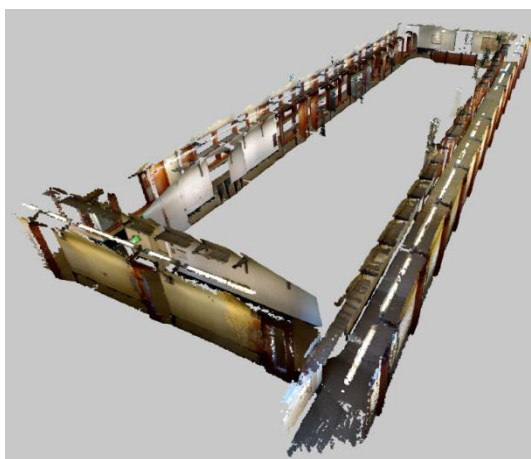


Figure 2.23 – A sample map created by the RGBD-ICP mapping system. (from Henry et al. (2012))

3. Data Collection using Microsoft Kinect for Xbox 360

In the previous chapter, potential sensors and approaches for the collection of range data in indoor scenes were introduced. In the presented work, the low-cost and accessible RGB-D camera Microsoft Kinect for Xbox 360 is employed as the case study for the collection of 3D point cloud of interiors. This chapter presents the mathematical background for the system calibration, derivation of point clouds from disparity data and colorization of the point clouds. Moreover, in extreme cases where vision-based and depth-matching-based registration approaches mentioned in the previous chapter fail, due to the lack of visual features and appropriate geometrical scene structure, a registration approach based on an indoor positioning solution is proposed as a complementary approach.

3.1. Point Cloud Collection by Kinect

3.1.1. System Interfaces and SDKs

For the collection of colored point clouds using Kinect, low level data streams such as color images and disparity data have to be extracted using a Software Development Kit (SDK). SDKs enable the interaction of the user with the system using specific programming languages (e.g. C, C++, C#, Java and Python). In November 2010, when the Kinect system was first introduced as an interface for the Xbox 360 game console, no official driver was introduced for developers. However, shortly after that, open-source drivers such as libfreenect (OpenKinect project) and OpenNI (PrimeSense) were released to support the data acquisition with Kinect. The official Kinect SDK for the Microsoft Windows operating system was released in February 2011, which additionally supports gesture and face recognition, voice recognition, alignment of the range data, etc.. In the present work, the libfreenect driver was used for the interaction with the Kinect, as it supports programming under the free and popular operating system Linux.

3.1.2. System Calibration

The Kinect system integrates a range measurement system (combination of an IR laser projector and an IR camera) and an RGB camera (see figure 3.1). For the colorization of the Kinect point clouds, and also registration of the point clouds using visual information, the Kinect range data have to be registered with the color information. For a correct pixel-to-pixel registration of RGB and depth values, besides the calibration of the IR and RGB cameras, the relative pose between the two cameras has to be estimated precisely. The camera calibration refers to the determination of camera interior orientation parameters (principal distance and the image coordinates of the principal point) together with the parameters describing image errors (e.g. lens distortion parameters).

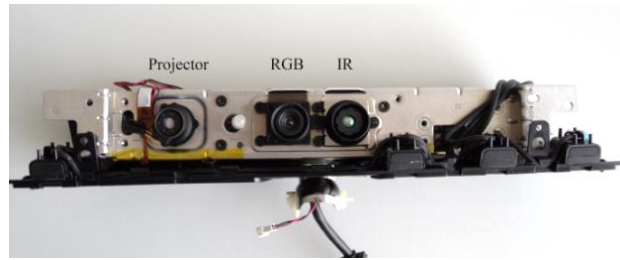


Figure 3.1 – A disassembled Kinect; the system consists of an IR laser projector, an IR and an RGB camera.

According to Luhmann et al. (2014), three calibration techniques can be distinguished: laboratory calibration, test-field calibration and self-calibration. Laboratory calibration was used in the past for the calibration of metric cameras using optical alignment instruments. This method cannot be done by the user, and therefore meets little applications in close range photogrammetry. State-of-the-art close range techniques employ the analytical calibration methods in which the observation of the image coordinates is used to derive the interior orientation parameters using a bundle block adjustment. Moreover, by the inclusion of additional parameters, the position of the perspective center and the lens distortion effects are modeled. The test-field calibration method employs a target field, photographed using a suitable camera configuration, in order to ensure a suitable ray intersection, while filling the maximum image format to assure a small correlation between the estimated parameters. In practice, the test-field might be replaced by the actual object, only if a condition similar to the test-field calibration can be fulfilled, to ensure a suitable ray intersection and small correlation between the estimated parameters (self-calibration).

In the test-field calibration, measured image coordinates and approximate object coordinates are processed using an unconstrained datum bundle adjustment technique (e.g. free net adjustment technique), in order to avoid the effect of possible inconsistencies in the datum information on the estimated unknowns. Moreover, to ensure the maximum accuracy in the estimation of the relative pose between the two cameras, the exterior orientation together with the interior orientation parameters of the IR and RGB images are estimated in one bundle adjustment process. It is necessary to mention that the corresponding image pairs (IR and RGB) used in the bundle adjustment have to be taken synchronously at multiple viewpoints, in order to avoid erroneous measurement of the stereo baseline. The bundle adjustment is based on the well-known collinearity equations (equations (3.4)) which are set for each target point. The collinearity equations are derived from the central projection equations (equations (3.1), see figure 3.2) by solving the point dependent scale factor from the third row and replacing it in the first and second rows.

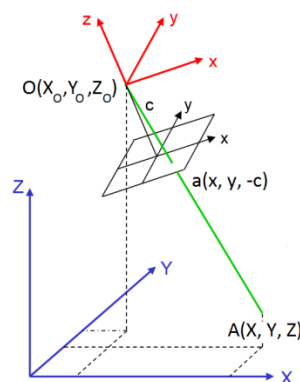


Figure 3.2 – Central projection principle. (adapted from Cramer (2014))

$$\begin{pmatrix} X_A \\ Y_A \\ Z_A \end{pmatrix} = \begin{pmatrix} X_O \\ Y_O \\ Z_O \end{pmatrix} + \lambda_A \cdot \mathbf{R} \cdot \begin{pmatrix} x_a - x_p - \Delta x \\ y_a - y_p - \Delta y \\ -c \end{pmatrix} \quad (3.1)$$

$$\begin{pmatrix} x_a - x_p - \Delta x \\ y_a - y_p - \Delta y \\ -c \end{pmatrix} = \lambda_A^{-1} \cdot \mathbf{R}^{-1} \cdot \begin{pmatrix} X_A - X_O \\ Y_A - Y_O \\ Z_A - Z_O \end{pmatrix} \quad (3.2)$$

$$\lambda_A^{-1} = \frac{-c}{r_{13}(X_A - X_O) + r_{23}(Y_A - Y_O) + r_{33}(Z_A - Z_O)} \quad (3.3)$$

$$\begin{aligned} x_a &= x_p - c \frac{r_{11}(X_A - X_O) + r_{21}(Y_A - Y_O) + r_{31}(Z_A - Z_O)}{r_{13}(X_A - X_O) + r_{23}(Y_A - Y_O) + r_{33}(Z_A - Z_O)} + \Delta x_a \\ y_a &= y_p - c \frac{r_{12}(X_A - X_O) + r_{22}(Y_A - Y_O) + r_{32}(Z_A - Z_O)}{r_{13}(X_A - X_O) + r_{23}(Y_A - Y_O) + r_{33}(Z_A - Z_O)} + \Delta y_a \end{aligned} \quad (3.4)$$

In these equations:

- X_A, Y_A, Z_A are the coordinates of the point A in the world coordinate system;
- λ_A is the scale factor corresponding to point A;
- \mathbf{R} is the rotation matrix from the object to image coordinate system;
- r_{ij} is the $\mathbf{R}(i,j)$ element;
- x_a, y_a are the measured image coordinates for the point A;
- x_p, y_p are the coordinates of the principal point;
- $\Delta x_a, \Delta y_a$ are the correction terms for image coordinates corresponding to point A;
- c is the calibrated focal length;
- X_O, Y_O, Z_O are the coordinates of the camera projection center in the world coordinate system.

According to Guidi and Remondino (2012), for the estimation of the correction terms (additional parameters) $\Delta x, \Delta y$, the model developed by Brown (1971) is proved to be the most effective, in particular for close range sensors. The Brown calibration model which is a physical model, estimates the lens distortion effect in the radial and decentering (tangential) directions by:

$$\begin{aligned} \Delta r_{\text{Radial}} &= K_1 r^3 + K_2 r^5 + K_3 r^7 + \dots \\ r &= \sqrt{(x - x_p)^2 + (y - y_p)^2} \end{aligned} \quad (3.5)$$

$$\Rightarrow \begin{cases} \Delta x_{\text{Radial}} = x \frac{\Delta r_{\text{Radial}}}{r} \Rightarrow \Delta x_{\text{Radial}} = x_d (K_1 r^2 + K_2 r^4 + K_3 r^6) \\ \Delta y_{\text{Radial}} = y \frac{\Delta r_{\text{Radial}}}{r} \Rightarrow \Delta y_{\text{Radial}} = y_d (K_1 r^2 + K_2 r^4 + K_3 r^6) \end{cases} \quad (3.6)$$

$$\begin{cases} \Delta x_{\text{Tangential}} = (1 + P_3 r^2) \cdot (P_2 (r^2 + 2x_d^2) + 2P_1 x_d y_d) \\ \Delta y_{\text{Tangential}} = (1 + P_3 r^2) \cdot (P_1 (r^2 + 2y_d^2) + 2P_2 x_d y_d) \end{cases} \quad (3.7)$$

in which $K_{1,2,3}$ are the distortion coefficients for the radial direction, $P_{1,2}$ are the distortion coefficients for the tangential direction, r is the radial distance reduced to the estimated principal point and x_d, y_d are distorted image coordinates reduced to the principal point.

Besides the Brown's physical model for the estimation of the additional parameters, Tang et al. (2012) prove that there are rigorous and effective mathematical models based on the Legendre polynomials, which are able to compensate distortions of very small magnitude (around 0.05 pixels). Equation (3.8) presents an exemplary model of additional parameters derived based on the Legendre polynomials with 34 unknowns (corresponding to degrees $m=4$ and $n=3$). The maximum order of the polynomial should be chosen by the compromise between the optimal accuracy and reducing over-parametrization.

$$\begin{aligned} \Delta x &= a_1 p_{1,0} + a_2 p_{0,1} + a_3 p_{2,0} + a_4 p_{1,1} + a_5 p_{0,2} + a_6 p_{3,0} + a_7 p_{2,1} + a_8 p_{1,2} + a_9 p_{0,3} + a_{10} p_{4,0} + \\ &\quad a_{11} p_{3,1} + a_{12} p_{2,2} + a_{13} p_{1,3} + a_{14} p_{4,1} + a_{15} p_{3,2} + a_{16} p_{2,3} + a_{17} p_{4,2} + a_{18} p_{3,3} + a_{19} p_{4,3} \\ \Delta y &= a_2 p_{1,0} - a_1 p_{0,1} + a_{20} p_{2,0} - a_3 p_{1,1} - a_4 p_{0,2} + a_{21} p_{3,0} + a_{22} p_{2,1} + a_{23} p_{1,2} + a_{24} p_{0,3} + a_{25} p_{4,0} + \\ &\quad a_{26} p_{3,1} + a_{27} p_{2,2} + a_{28} p_{1,3} + a_{29} p_{4,1} + a_{30} p_{3,2} + a_{31} p_{2,3} + a_{32} p_{4,2} + a_{33} p_{3,3} + a_{34} p_{4,3} \end{aligned} \quad (3.8)$$

In these equations, a_i coefficients are the additional parameters and $p_{m,n}$ represent the series of continuous orthogonal polynomials based on the Legendre polynomials. This family of additional parameters is used where the Brown's model is not sufficiently accurate and a very high accuracy is required. However, this is not the case for the Kinect images, due to the high level of noise and blur contained in image observations. Moreover, in practice, interest points are extracted and matched based on the SIFT or other feature detectors, which deliver an accuracy of about 0.7 pixels (Mikolajczyk and Schmid, 2004). Therefore, image measurements of around 0.5 pixels accuracy will be sufficient in case of using Kinect. Numerical results and evaluations regarding the calibration of the Kinect system are presented in section 6.1.1.

3.1.3. Generation of Colored Point Clouds

As already mentioned, the Kinect system calibration enables a correct registration of RGB and depth values. In the first step, the disparity values have to be converted to depth values. Afterwards, through some transformation steps which are described in this chapter, RGB values are transformed into the IR image space for colorizing the point clouds.

3.1.3.1. From Disparity Image to 3D Point Clouds

In normal stereo photogrammetry, where two identical cameras have parallel axes perpendicular to the baseline, disparity measurements are related to the object distance by the following equation:

$$\frac{H}{b} = \frac{c}{d} \quad (3.9)$$

whereby H is the depth or the object distance, b is the stereo baseline length, c is the focal length of the IR camera and d is the measured disparity. This equation can be derived from the ratios indicated in figure 3.3 or from the collinearity equations, by setting the rotation angles equal to zero. The distance uncertainty with respect to the uncertainty in the disparity measurement is given by:

$$\delta H = \frac{H^2}{b \cdot c} \cdot \delta d \quad (3.10)$$

The equation shows that the distance uncertainty is proportional to the square of the object distance.

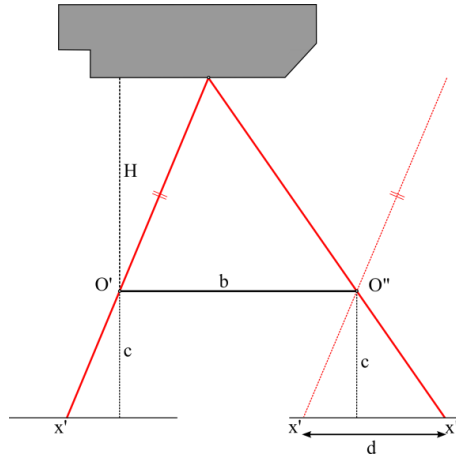


Figure 3.3 – Normal case of stereo photogrammetry. (adapted from Luhmann et al. (2014))

Referring to the equation (3.9), at zero disparity the object distance is infinity, since the rays are parallel. Kinect disparities are not normalized in the same way; they are in the range of $[0, 1023]$ (1 out of the 11 bits is reserved as a validity marker for the data, i.e. it marks the pixels for which no measurement is available (Khoshelham and Elberink, 2012)). The zero disparity does not correspond to an infinite distance, but to the distance to the reference plane (at a known depth) memorized in the device. According to “ROS Kinect calibration” (2011), Kinect disparities are supposed to be denormalized using a linear transformation (consisting of a shift and a scale factor), which can be expressed by:

$$d = \frac{1}{8} \cdot (\text{offset} - d_k) \quad (3.11)$$

in which, d is the denormalized disparity and d_k is the disparity measured by Kinect.

As the image matching algorithm of Kinect has sub-pixel accuracy, the scale factor $1/8$ is considered to convert the measurements to the pixel unit. The offset value and the stereo baseline are computed using a least squares adjustment, having observed some known depths at different distances. By substituting the equation (3.11) in (3.9), H is computed. The 3D coordinates of the corresponding point is then computed by:

$$H = \frac{b \cdot c}{\frac{1}{8} \cdot (\text{offset} - d_k)} \quad (3.12)$$

$$\begin{pmatrix} X \\ Y \\ Z \end{pmatrix} = \begin{pmatrix} H/c & 0 & 0 \\ 0 & H/c & 0 \\ 0 & 0 & -1 \end{pmatrix} \cdot \begin{pmatrix} x \\ y \\ z \end{pmatrix} \quad (3.13)$$

in which, x, y are the coordinates of the point in the IR image space, or equivalently in the disparity image space.

3.1.3.2. Adding Color to the Point Clouds

For colorizing the point cloud, the depth values shall be registered with the RGB image. Figure 3.4 depicts the main transformation steps (T_1 , T_2 , T_3) required to transform a pixel from the disparity to the RGB image space.

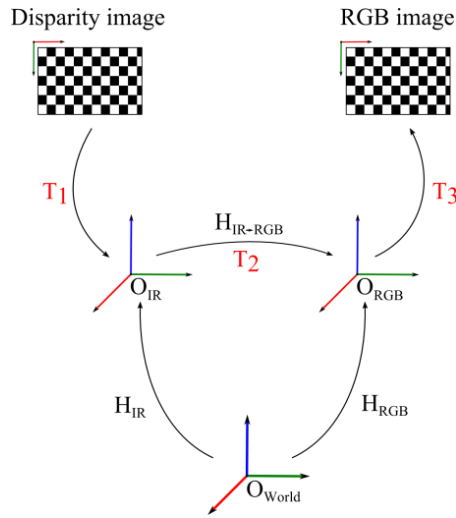


Figure 3.4 – Transformation from disparity to RGB image space.

In the first transformation (T_1), the disparity image is converted to IR camera local 3D coordinates (equation (3.13)). In the second transformation (T_2), 3D coordinates are converted from IR to RGB camera local 3D coordinate system (equation (3.14)):

$$\mathbf{H}_{IR} = \begin{pmatrix} \mathbf{R}_{IR(3 \times 3)} & \mathbf{T}_{IR(3 \times 1)} \\ \mathbf{0}_{(1 \times 3)} & 1 \end{pmatrix}$$

$$\mathbf{H}_{RGB} = \begin{pmatrix} \mathbf{R}_{RGB(3 \times 3)} & \mathbf{T}_{RGB(3 \times 1)} \\ \mathbf{0}_{(1 \times 3)} & 1 \end{pmatrix}$$

$$\mathbf{H}_{IR \rightarrow RGB} = \mathbf{H}_{IR}^{-1} \times \mathbf{H}_{RGB}$$

$$\mathbf{X}_{RGB(hom)} = \mathbf{H}_{IR \rightarrow RGB} \times \mathbf{X}_{IR(hom)} \quad (3.14)$$

where:

- \mathbf{R} and \mathbf{T} are the exterior orientation parameters of the RGB and IR cameras, which have already been computed by the system calibration (section 3.1.2);
- $\mathbf{X}_{RGB(hom)}$ and $\mathbf{X}_{IR(hom)}$ are the homogeneous coordinates of the corresponding point in RGB and IR local 3D coordinate systems, respectively.

Finally, in the last transformation (T_3), using the projective matrix of the RGB camera (equation (3.15)), the corresponding coordinates in the RGB image space are computed (Hartley and Zisserman, 2003):

$$\mathbf{K}_{\text{RGB}} = \begin{pmatrix} c_{\text{RGB}} & 0 & x_p \\ 0 & c_{\text{RGB}} & y_p \\ 0 & 0 & 1 \end{pmatrix}$$

$$\mathbf{P} = \mathbf{K}_{\text{RGB}} \times \mathbf{R}_{\text{IR} \rightarrow \text{RGB}} \times \begin{pmatrix} \mathbf{I}_{(3 \times 3)} & -\mathbf{T}_{\text{IR} \rightarrow \text{RGB}} \end{pmatrix}$$

$$\mathbf{x}_{\text{RGB (hom)}} = \mathbf{P} \cdot \mathbf{X}_{\text{RGB (hom)}} \quad (3.15)$$

In the equations:

- \mathbf{K}_{RGB} is the calibration matrix of the RGB camera;
- \mathbf{P} is the projection matrix of the RGB camera;
- $\mathbf{x}_{\text{RGB (hom)}}$ and $\mathbf{X}_{\text{RGB (hom)}}$ are the homogeneous coordinates of the corresponding point in RGB image and 3D local object coordinates, respectively.

The mentioned transformations enable the registration of each pixel in the disparity image, and therefore a point in the corresponding 3D object coordinates to an RGB value.

3.2. Point Clouds Registration

In section 0, available approaches for the registration of the point clouds in indoor applications were introduced. For the registration of the Kinect point clouds, as mentioned before, SfM and SLAM approaches can be used. Commercial and open-source implementations of some of the solutions are available. Software such as ReconstructMe (“ReconstructMe,” 2015), Skanect (“Skanect by Occipital,” 2015), FARO SCENECT (“SCENECT,” 2015) and KinFu Large Scale (Rusu and Cousins, 2011) enable the user to easily scan the objects or scenes without requiring knowledge about photogrammetry, computer vision and robotics. The user usually interacts with the software front-end, and cannot manipulate parameters to deal with challenging scenes with poor texture or geometrical information. To deal with such issues, one may use or customize available SfM or SLAM implementations to adapt the localization method with the application.

3.2.1. Point Clouds Registration Based on RGB and Depth Information

This study uses the free software VisualSFM – the implementation of an SfM method to orient RGB images captured by the Kinect system (Wu, 2013; Wu et al., 2011). Similar to all SfM methods, VisualSFM uses point features to incrementally estimate the scene structure and camera poses. The solution is then merged into a bundle adjustment for the global optimization of this estimation. As a result of this process, 3D coordinates of point features are derived in a 3D local coordinate system up to the scale factor. The scale factor is estimated by the best fitting of the 3D local coordinates with the corresponding 3D object coordinates of matched point features at each range image frame, which is then averaged over all frames. For the best fitting of the 3D point features at each range image frame, having more than 3 points, a least squares adjustment can be performed based on the 3D similarity (Helmert’s 7-parameters) transformation:

$$\mathbf{X}_{\text{Object}} = \lambda \cdot \mathbf{R} \cdot \mathbf{X}_{\text{Local}} + \mathbf{T} \quad (3.16)$$

In this equation:

- $\mathbf{X}_{\text{Object}}$ and $\mathbf{X}_{\text{Local}}$ are the 3D coordinates of point features in the object (metric) and local coordinate systems;
- λ is the scale factor;
- \mathbf{R} is the rotation matrix applied to the local coordinates;
- \mathbf{T} is the translation vector from the centroid of rotated and scaled local to the centroid of the object coordinates.

As the model is not linear regarding the unknown parameters λ , \mathbf{R} and \mathbf{T} , initial values and iteration are required to estimate the unknown parameters. To avoid this issue, closed-form solutions to the least squares problem is proposed by Horn (1987) and Sanso (1973), which are based on the unit quaternions for the representation of rotations (see appendix A).

The RGB camera orientation parameters in the metric space can be used directly for the registration of the corresponding point clouds, since the relative orientation of the RGB and IR camera is fixed. Figure 3.5 depicts an example in which the point clouds collected from 10 viewpoints are aligned using the mentioned approach.

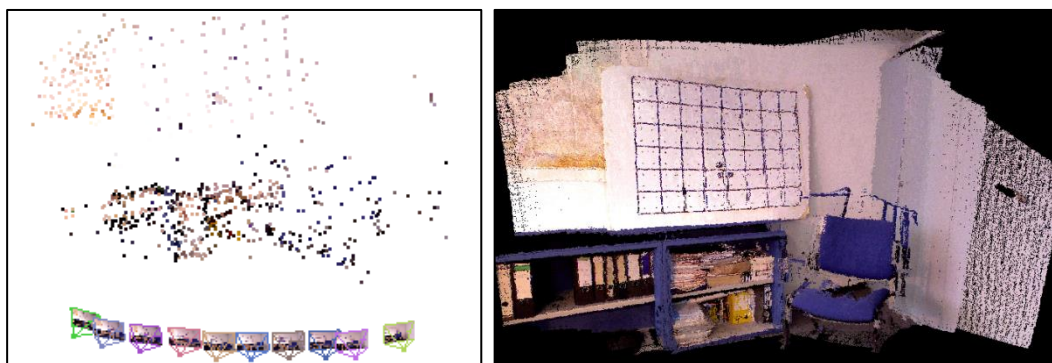


Figure 3.5 – Oriented images and the sparse point cloud corresponding to point features (left); aligned point clouds corresponding to the color images (right). Images are oriented using the VisualSFM software.

3.2.2. Point Clouds Registration Based on an Indoor Positioning Solution and Available Coarse Indoor Models

Vision-based and depth-matching-based registration approaches for the estimation of the sensor pose rely on the existence of sufficient well distributed features of interest, as well as suitable geometry of the scene to constrain the sensor 6 DOF. Therefore, such approaches fail in scenarios with poor texture, or scenes with insufficient geometric information. This issue can be handled for instance by integrating inertial solutions into the system. For example, ZEB1 mobile mapping system (by CSIRO) uses a 2D laser range finder supported by a low-cost MEMS IMU for the localization and mapping purpose. In the robotics community, visual and inertial information are merged together for the localization purpose using visual-inertial SLAM methods (for example see (Leutenegger et al., 2013)). However, in order to avoid drift error, the existence of visual constraints in keyframes is inevitable.

This study presents a new complementary approach for the registration of collected point clouds in extreme scenarios, in which the abovementioned methods fail, due to having poor texture and symmetrical geometrical structure (e.g. hallways). For this purpose, the point cloud registration task is supported by an indoor positioning method implemented at the Institute for Photogrammetry, together

with information extracted from available coarse models. Figure 3.6 depicts the overview of this approach, which is described in detail in following sections.

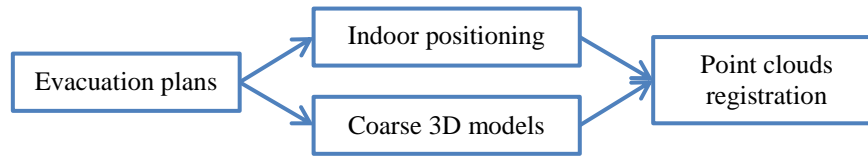


Figure 3.6 – Flowchart of the proposed approach for the registration of the point clouds: evacuation plans support the indoor positioning by map matching, and at the same time, are used to generate coarse indoor models. The user’s track and the information extracted from the coarse indoor model enable the registration of point clouds.

3.2.2.1. Indoor Positioning Method Based on a Foot Mounted MEMS IMU

In recent years, indoor positioning has increasingly been focused by the robotics and computer vision communities, and various approaches are proposed to solve this problem. As stated by Peter et al. (2010), most of the approaches either use an extra infrastructure such as WLAN networks or RFID beacons, or require a high quality indoor model. Therefore, low-cost sensor systems such as MEMS IMUs have been focused to overcome the limitations. However, such systems suffer from large drifts shortly after the data collection starts. To improve the accuracy, Godha and Lachapelle (2008) suggest the use of zero-velocity updates algorithm (ZUPT) to reduce the problem of error accumulation over time and to maintain the accuracy bounds for longer periods. In this approach, the MEMS IMU is mounted on the user’s foot, and therefore the foot dynamics enable the use of frequent zero-velocity updates.

Although zero-velocity updates significantly reduce the accumulation of the drift error, still this effect is considerable in longer tracks. Therefore, Peter et al. (2011, 2010) further improve the accuracy of navigation using the information extracted from the available coarse indoor models, assuming the most parts of the user’s track is parallel or perpendicular to the main direction of the building. This study uses their implemented software for the derivation of the user’s track.

3.2.2.2. Generation of Coarse Indoor Models

In Peter et al. (2010), a new approach for the extraction of course indoor models from available evacuation plans is presented. In many countries, existence of such plans is compulsory for the public buildings such as hospitals, universities, hotels, etc. The coarse models support the aforementioned indoor positioning method, as well as point cloud registration, as will be shown in the following sections. The procedure for the generation of such models is summarized in section 4.2.3.

3.2.2.3. Data Collection

For the data collection purpose, the user employs a foot mounted MEMS IMU and starts walking from the position where the evacuation plan is photographed into the corridor, while holding a Kinect system and capturing the range and MEMS IMU data, simultaneously. The user’s track as well as the coarse indoor model is then derived using the aforementioned methods. Afterwards range images have to be pre-processed and finally transformed into the world coordinate system using a rigid-body transformation. The details are described in the following sections.

3.2.2.4. Pre-Processing of the Point Clouds

In this step, point clouds are levelled in the horizontal plane (to compensate the sensor tilt) and the heights are modified (using a shift in the vertical direction), so that the ground parts of the point clouds lay at a same level. For this purpose, first the normal vectors of range images are analyzed in order to find the ground points and to estimate the point clouds tilts regarding the horizontal plane. Points are segmented as ground points, if the angular difference between their normal vector and the vertical axis is less than a threshold (e.g. 45° which is a quite tolerant threshold). The segmentation is refined iteratively by compensating the tilt and removing outliers. The point cloud of the walls can also be grouped using a similar procedure, which is required by the next steps.

3.2.2.5. Extraction of 3D Rigid Transformation Parameters

In this step, the user's track is analyzed in order to estimate the orientation of the point clouds considering the captured timestamps (see figure 3.7). As the tilt of the system is already compensated and the heights of the point clouds are equalized in the pre-processing step, the registration process only consists of a rotation around the vertical axis as well as a translation in 2D space. The coordinates of the track points are directly considered as 2D translations. Rotations are computed, assuming the sensor is oriented towards the direction of the next track point. Equations (3.17) and (3.18) show the rotation angle α and translation components (X_T , Y_T) for the registration of the point cloud corresponding to the i^{th} track point. Figure 3.7 depicts the registration of two exemplary point clouds of the hallway using only position traces. As it is visible in this example, the point clouds are coarsely aligned; the alignment will be refined in the next steps using the information extracted from the coarse model.

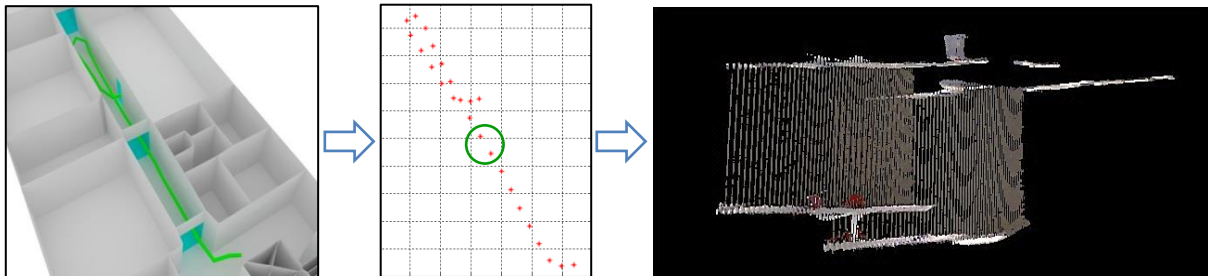


Figure 3.7 – Initial point clouds alignment using position traces. Left to right: coarse model together with the aligned user's track, position traces and top view of two initially registered point clouds.

$$\alpha_i = \arctan \left(\frac{Y_{\text{World}_{i+1}} - Y_{\text{World}_i}}{X_{\text{World}_{i+1}} - X_{\text{World}_i}} \right) \quad (3.17)$$

$$\begin{aligned} X_{T_i} &= X_{\text{World}_i} \\ Y_{T_i} &= Y_{\text{World}_i} \end{aligned} \quad (3.18)$$

3.2.2.6. Improving the Registration Using the Coarse 3D Model

The registration can be further refined using the information extracted from the coarse indoor model. For example in this scenario, enforcing the parallelism of detected walls in the point clouds and the corresponding walls in the coarse indoor model is suggested. However, it should be mentioned that this refinement strategy is only possible in case the coarse model is not subject to significant changes; only slight changes in the room dimensions or the verification of available coarse models is possible by this solution. The following steps describe this constraining procedure in detail.

Generation of 2D orthographic projected image: To imply this constraint, the problem is first reduced to two dimensions by projecting the point clouds onto a horizontal plane. A 2D grayscale orthographic projected image (2D histogram) is then computed from the projected points, using the same procedure as mentioned in section 5.2.1. The grayscale image is then converted to a binary image by setting a threshold (figure 3.8). Binarization also removes the ground and ceiling points as well as small features existing in the scene, as they correspond to smaller gray values.

Morphological image processing: As depicted in figure 3.8, the traces of walls in the projected image are shapes which are not necessarily straight lines. In order to robustly estimate straight lines using the Hough transform (see appendix D), the trace has to be first pre-processed. For this purpose, the shape is converted to a closed structure by filling the holes using a morphological closing algorithm (dilation followed by erosion). This also removes some of the remaining noise in the binary image. The shapes are thinned to one pixel width elements passing through the middle of the shapes using the morphological skeletonization (see figure 3.9). Since a similar process is used in section 0, for more details please refer to this section.

Estimation of straight lines: After the estimation of the skeleton of the walls trace, straight lines can be estimated using a Hough transform (see figure 3.10). A similar procedure is done for the estimation of straight lines in the 2D coarse model (the corresponding parts of the coarse model are selected considering a buffer around the track points).

Line matching and constraining: To impose the constraints, the corresponding lines estimated in the projected image and the 2D coarse model shall be found and enforced to be parallel. The corresponding lines (walls' projection) then can be assumed as the closest line segments having the most similar orientation (see figure 3.11). This assumption is valid due to the already existing coarse registration of the point clouds with the coarse model. Having found the corresponding line segments, the mean difference between the corresponding orientations is considered as the correction to the orientation of the corresponding point cloud in the horizontal plane. Figure 3.12 depicts the registration results after the constraining process.

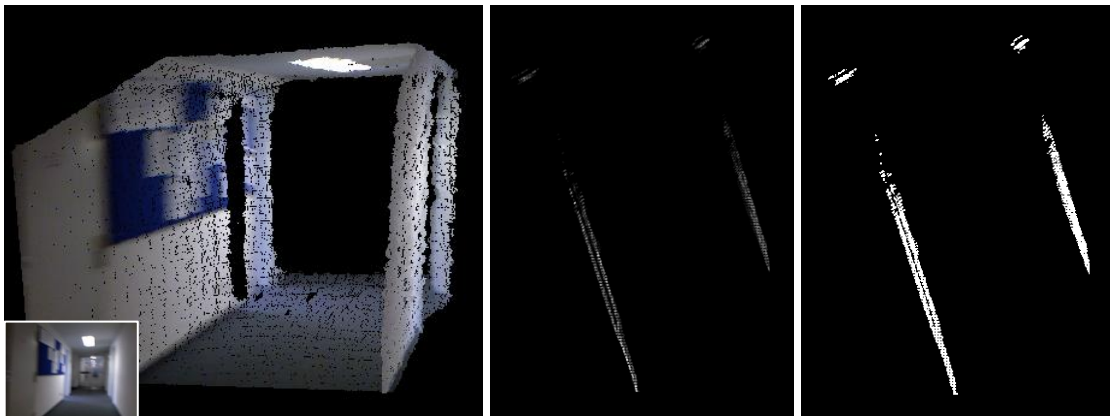


Figure 3.8 – A single point cloud and the corresponding 2D grayscale and binary images.

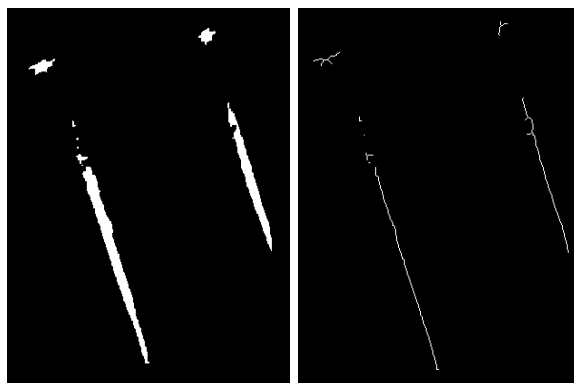


Figure 3.9 – Polygon closing (left) and skeletonization (right).

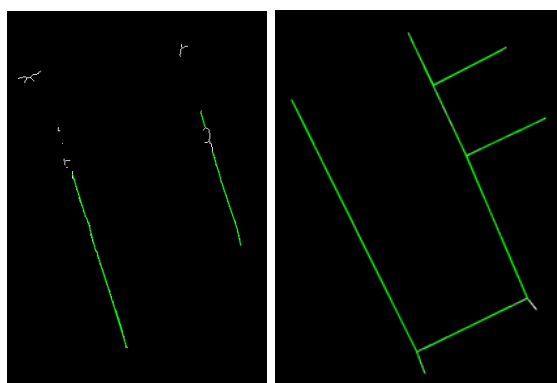


Figure 3.10 – Estimated Hough lines in the orthographic projected image and the coarse model.

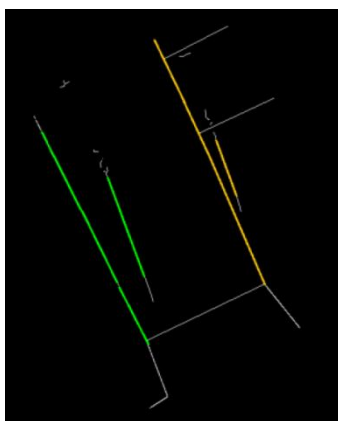


Figure 3.11 – Corresponding line segments in a point cloud and the coarse model.

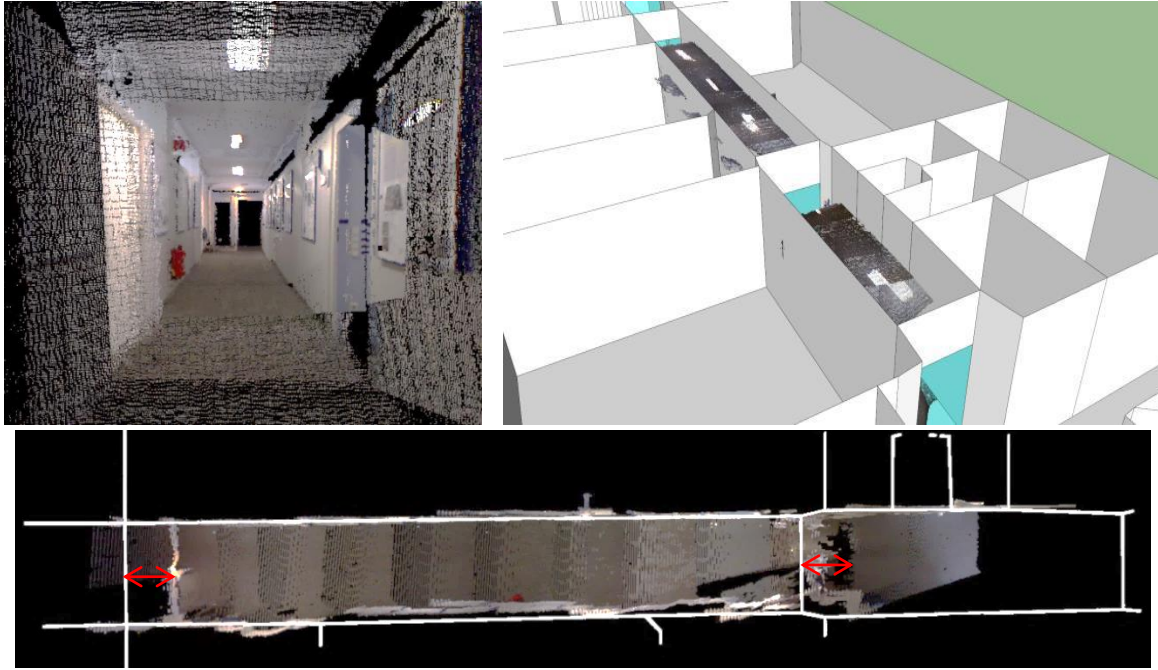


Figure 3.12 – Registered point clouds of the hallway after the constraining process.

3.2.2.7. Accuracy Analysis of the Registration Approach

The accuracy of this registration approach is directly related to the accuracy of the positioning method. As it is marked in figure 3.12 (bottom), the registered point cloud has a shift with respect to the coarse model. The reason is the existence of errors in the estimation of the user's first track point, which is in fact the location that the user takes photograph of the evacuation plan.

The internal accuracy (precision) of the registration approach is estimated by measuring and comparing the 3D coordinates of some corresponding features in the consecutive point clouds (equation (3.19)). This includes the error of the positioning method, measuring the coordinates of the features (due to the noise of the range images), and errors due to the change in the relative pose of the Kinect with respect to the foot-mounted MEMS IMU at different measurement epochs. The results are presented in figure 3.13.

$$\sigma_{j \rightarrow j+1} = \frac{\sum_{i=1}^{n_{j,j+1}} \sqrt{(X_{i,j+1} - X_{i,j})^2 + (Y_{i,j+1} - Y_{i,j})^2 + (Z_{i,j+1} - Z_{i,j})^2}}{n_{j,j+1}} \quad (3.19)$$

In the abovementioned equation, $\sigma_{j \rightarrow j+1}$ is the alignment accuracy between two epochs, $n_{j,j+1}$ is the number of common matches between the two consecutive scans and $(X_{i,j}, Y_{i,j}, Z_{i,j})$ are the coordinates of the i^{th} point in the j^{th} scan. The estimated accuracies in the case study are generally better than 10cm, which seems rational regarding the mentioned sources of errors. However, in order to achieve higher accuracies, one may benefit from the combination of all the available observations, i.e. inertial, vision and depth measurements. The fusion of such measurements can be realized for instance by SLAM methods; for example (Leutenegger et al., 2013) tightly combine visual and inertial measurements and integrate them in SLAM, or (Endres et al., 2012) present an RGB-D SLAM approach that benefits from the scale information and 3D features extracted from depth images.

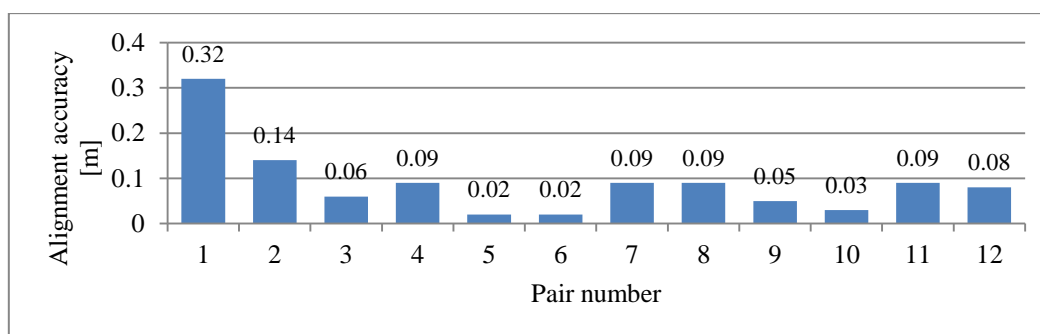


Figure 3.13 – Estimated precision of the registration in the sequence of scan positions.

3.3. Kinect SWOT Analysis

In this section, strengths, weaknesses, opportunities and threats of Kinect as a sensor system for point cloud collection are summarized.

Strengths: The low price and accessibility of Kinect enable the wide usage of this sensor by many researchers. Kinect streams the range data and RGB data in 30Hz; the small size and weight of this sensor in comparison with TLS and indoor mobile mapping systems make it very flexible and popular for scanning of objects as well as indoor scenes. The Kinect high data acquisition rate makes the data collection task very fast in comparison with the laser scanners. Moreover, available open-source drivers and software simplify the interaction and data acquisition with the device.

Weaknesses: As will be shown in section 6.1.2, the quality of the range data depends on the object distance. The sensor delivers range data with centimeters accuracy. Although Kinect supports range measurements within the range of 0.5 to 6m, in order to avoid having a noisy point cloud the practical object distance shall be less than the theoretical limit, depending on the required accuracy in each application. Considering the relatively small viewing angle of the system ($57^{\circ}\text{H}\times 43^{\circ}\text{V}$), the point cloud registration is a challenge in scenes having insufficient visual or geometrical features.

Opportunities: Considering the price, availability, size, weight and accuracy of the delivered data, Kinect is a suitable alternative to available active range measurement systems. Having fused useful sensors, Kinect is becoming increasingly popular for many researchers focusing on 3D object reconstruction, indoor mapping, SLAM, robotics, etc. Moreover, it can be potentially used for crowdsourcing in 3D mapping of the building interiors that fulfills the LOD4 completion of CityGML representation of urban objects.

Threats: Since the release of the Kinect, RGB-D cameras have become very popular; many companies are developing consumer-grade RGB-D cameras with more functionality (e.g. integrating SLAM methods for the automatic point cloud registration). An example is the Structure Sensor that collects and aligns the data in real-time, and provides a high-level SDK to enable a feasible development of indoor and AR applications (“structure.io,” 2014). Another example is the Google Project Tango that integrates the RGB-D sensor into Android platforms, and aligns the collected point clouds in real-time using visual-inertial odometry techniques. Moreover, the users are able to develop indoor applications using the SDK (“ATAP Project Tango,” 2015, “Tango Concepts,” 2015).

4. Overview of Available Indoor Modeling Approaches

Indoor geometric modeling or representing the 3D shape of building interiors in terms of surfaces and volumes plays an important role in cost reduction and delivering high quality supports in many indoor applications such as supporting BIMs, interior architecture, risk management, security planning, etc. This task has been focused by researchers during the last two decades – specially in the last few years – due to advances in data collection platforms and vision algorithms, as well as requirements raised from a new range of applications. Due to the complexity of the reconstruction process, the automation of this task is still an ongoing research topic.

Currently, the process of indoor modeling is widely performed in a manual or semi-manual fashion, either by means of fitting geometric primitives to different parts of the point cloud (e.g. planes, spheres, cones and cylinders), or by means of interactive recognition of features of interest based on multiple view geometry techniques. Therefore, the operator's qualification can have a large influence on the quality of a 3D model (El-Hakim and Beraldin, 2006). Although the modeling of single objects can be fairly a quick task, still modeling of an average-sized building can be very tedious and may take several months (Panushev and Brandt, 2007), which is often the bottleneck in the generation of an as-built BIM creation project (Tang et al., 2010). Therefore, the need for the automation of the modeling process is obvious.

The automation of the modeling process is a challenging task due to several reasons. First, there are often unrelated objects in the scene such as furniture, which have to be removed before the modeling process. Second, the geometry of the object can be very complex, and therefore the modeling tool should be general enough to be able to deal with such cases. Third, the visual texture of the interiors might be too poor to successfully apply vision algorithms such as the SfM method, in order to recover camera poses. Fourth, visibility and map connectivity are often too challenging in floor plans containing interconnected rooms, since the room connections appear only in a small part of an image which can result in a weak connection geometry (Furukawa et al., 2009a). To solve each of these issues, assumptions have to be made, which consequently scale down the generality of the solution. This chapter presents an overview about state-of-the-art approaches for the automatic and semi-automatic modeling of building interiors.

4.1. Classification of Available Modeling Approaches

Due to the availability of different data acquisition techniques, data processing algorithm and accuracy requirements, the variety of reconstruction approaches is very large. According to comprehensive reviews given by Remondino (2003), Remondino and El-Hakim (2006) and Tang et al. (2010), the approaches can be classified based on many different criteria. The criteria can be for instance the type of the input information, the type of the measurements, the spatial and mathematical representation format of the outputs, used assumptions, or the level of automation.

Type of the input information: As the first and main classification criterion, the approaches based on the source of input information can be divided into two main categories: iconic (bottom-up modeling) and symbolic (top-down modeling). Iconic approaches generate models based on real measurements and observations, while symbolic approaches rely on hypotheses derived from the indoor reconstruction grammar, statistics and semantics.

Type of the measurements: Iconic reconstruction approaches rely on two main types of observations and measurements. They either recover 3D models from 2D images based on single and multiple view geometry (image-based), or from depth information derived from laser scanners, range cameras or dense image matching techniques (range-based).

Spatial representation: Another classification can be done according to the spatial representation of the output model. The output model can be represented either surface-based or volumetric. The volumetric representation (including solid geometric primitives and voxel representation) is more suitable for closed surfaces and objects. However, surface-based approaches (e.g. boundary-based representation) do not distinguish between closed and open surfaces. Most of the modeling approaches are categorized in this class. Moreover, it should be noted that some representations may belong to both classes; for example a geometric primitive can be considered as a surface, or at the same time, as a volume.

Mathematical representation: A further classification can be done according to the mathematical representation of the output model. Parametric approaches use a small number of parameters to represent a shape, and therefore require smaller storage volumes and computational complexities. In contrast, despite the high storage requirements of non-parametric approaches (such as triangular meshes), they are more flexible to represent complex geometries (Tang et al., 2010). However, the complexity of the resulting model is reduced using region growing algorithms based on the surface normal vectors (for example see (Hähnel et al., 2003)).

Used assumptions: The approaches can also be classified based on the assumptions regarding the object geometry and topology. Assumptions such as Manhattan-world scenario in most of the man-made scenes not only guarantee constructing a topologically correct model, but also make the reconstruction procedure easier and more robust (Budroni and Böhm, 2009). Other assumptions regarding the object geometry enable automatic fitting of geometric primitives to the segmented point clouds.

Automation level: The final classification is based on the level of user interactions during the reconstruction process.

Choosing the correct reconstruction approach depends on the application. For example, parametric volumetric approaches are most relevant to BIMs, but surface-based approaches are more common (Tang et al., 2010). In fact, although parametric volumetric approaches are more intuitive for the manipulation by the user (Kemper and Wallrath, 1987), they are less flexible due to the limited size of primitives libraries (Rottensteiner, 2000). Moreover, surface-based approaches enable efficient

representation of partially occluded objects (Walker, 1989). This study deals with the representation of the rooms main structures (walls); they can be simply represented by planar surfaces. Due to this and aforementioned reasons, here, only parametric surface-based approaches are focused. Readers interested in the field of automated reconstruction of volumetric model of indoor environments are referred to the works presented by Jenke et al. (2009), Oesau et al. (2014), as well as Xiao and Furukawa (2012).

The remainder of this chapter introduces state-of-the-art indoor reconstruction approaches, based on the source of the input data, which is the most general criterion according to the abovementioned classification scheme.

4.2. Iconic Approaches

Automatic and semi-automatic iconic (bottom-up) approaches for the reconstruction of geometric models use different sources of data, such as photographs, point clouds (collected by laser scanners, range cameras and dense image matching techniques) or available architectural plans to derive geometric models.

4.2.1. Image-Based Modeling

Image-based modeling is the process of reconstructing 3D models of scenes from measurements made on a single or multiple 2D images. According to Yu et al. (2011), the process includes detection, grouping and extraction of nodes, edges or faces, and interpreting them as 3D clues.

4.2.1.1. Modeling Based on Single View Geometry

Besides multiple view geometry in which 3D information is extracted from motion and parallax, in special cases, single view metrology can offer solutions to infer 3D information from single images (Criminisi et al., 1999, 1998; Hartley and Zisserman, 2003). Recovering 3D information from a single image is applicable, in cases where multiple views are not available, or the texture in images are too poor in multiple views for a successful camera pose estimation using SfM methods, or the baseline in multi-ocular systems is too short in comparison with the object distance. Such systems make use of geometric properties invariant to perspective projection, such as vanishing points and lines, straight lines, parallel lines and right angles (Criminisi et al., 1999). In practice, systems based on this approach need some prior knowledge about the scene geometry to enable simplifications and therefore automation of the modeling process. Figure 4.1 shows an example in which the 3D model is reconstructed using a single perspective image, from a scene containing three dominant and mutually perpendicular planes (building façades and the ground plane). The parallel lines in three main directions determine three vanishing points. This together with the estimated camera calibration and vanishing lines of planes which are not orthogonal, enable the reconstruction of 3D textured models (Hartley and Zisserman, 2003).

Assumptions which are valid in most indoor scenarios (e.g. existence of constrained geometries such as planes and straight lines, as well as relationships such as perpendicularity and parallelism) make the automatic estimation of the geometric invariants more feasible. For example in Delage et al. (2006), it is assumed that the scene is a “floor-wall” geometry. Their algorithm then recognizes the floor-wall boundary in the image, and recovers 3D information based on Bayesian methods, in which visual cues are combined with a prior knowledge about the scene geometry, such as main wall directions and the

way they connect to each other. Geometrical constraints similar to Manhattan-world geometry for man-made scenes are also used by Coughlan and Yuille (2003), Delage et al. (2006), Han and Zhu (2009), as well as Huang and Cowan (2009), in the field of single view 3D reconstruction. Figure 4.2 depicts an example in which the 3D model of a corridor section is automatically reconstructed from a single perspective cue, based on the extraction of geometric invariants (vanishing points, straight lines, etc.). Although this example presents a fully automated process of indoor reconstruction, assumptions such as existence of floor, ceiling and walls, as well as absence of windows and decorations under the horizontal line are necessary.



Figure 4.1 – 3D reconstruction based on a single perspective image. Top: original image (the Fellows quad, Merton College, Oxford); Bottom: 3D model from different views. (from Hartley and Zisserman (2003))

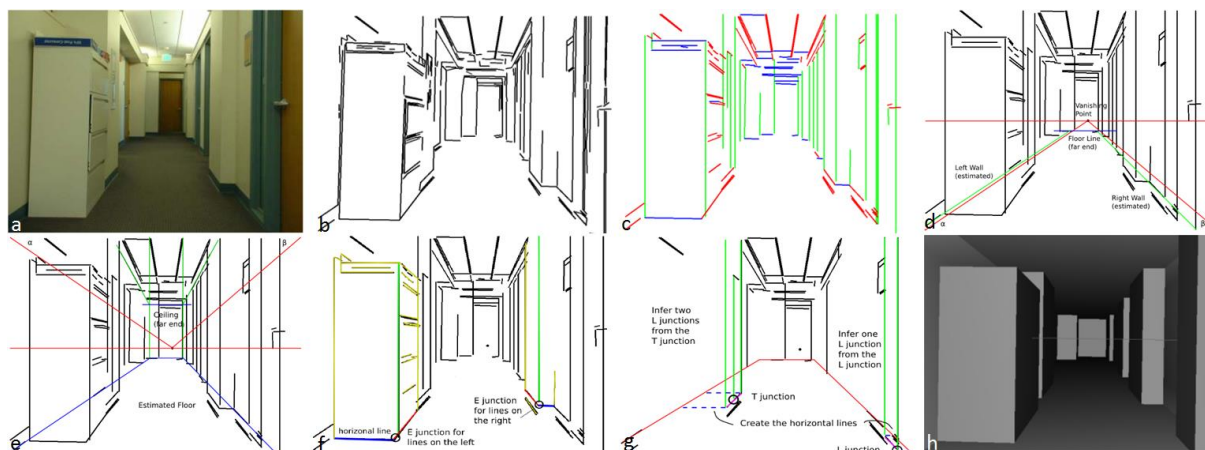


Figure 4.2 – Extraction of geometric invariants and 3D reconstruction: a) taken photograph, b) Canny edges, c) extracted lines, d) floor detection, e) ceiling detection, f, g) junction detection, h) resulting 3D model. (from Huang and Cowan (2009))

4.2.1.2. Modeling Based on Multiple View Geometry

3D reconstruction using photographs is more efficient and reliable using multiple view geometry, in comparison with single view geometry. Promising outcomes have been resulting using computer vision techniques during the last two decades in this field. In this modeling approach, the camera pose is estimated using corresponding points or line features across images. In the next step, the 3D model is generated either automatically having made some assumptions regarding the scene geometry, or in an interactive way by the user drawings. In the latter case, vanishing points and lines are turned to be powerful tools for 2D-to-3D applications that enable accurate sketching of polygonal faces in a single image, without the need for refinement in another image to build up a globally consistent model (Sinha et al., 2008).

The automation of the modeling process versus accuracy and generality trade-off is a challenge, and the correct decision depends on the application. As mentioned by El-Hakim (2002), in traditional modeling which is a widely used method, the focus is on the accuracy without a high level of automation. In such approaches, data acquisition and registration by photogrammetric and computer vision techniques are followed by an interactive drawing by the user. Although efforts are made for the automation of the whole modeling process, the solutions still may fail in new environments, in which the standard assumptions are not valid anymore, due to the scene complexity, or fragility of algorithms and vision techniques (e.g. demanding accurate point or line correspondences) (Shum et al., 1998). Therefore, the most impressive results are achieved by the semi-automated systems in which the user is in the processing loop (El-Hakim, 2002). Currently, although improvements and progresses are made in the automation of the modeling process, still user interaction is necessary to achieve a robust and general solution. Recent works have shown that the interaction can be very limited, simple and smart, by making some assumptions about the scene geometry, as well as making use of geometric invariants.

The semi-automated approach presented in Shum et al. (1998) makes use of panoramic image mosaics to efficiently cover the scene. It is one of the earliest works that uses regularities in man-made scenes as constraints in the modeling process. The problem of image registration in this case is decoupled into a zero baseline problem (for photos taken with a rotating camera) and a wide baseline stereo or SfM problem. Therefore, the camera pose for each mosaic is computed under the assumption of having some lines with known directions (e.g. horizontal or vertical lines). The baselines between the panoramic images can be recovered having some known points and using robust computer vision approaches. The modeling part of this system is an interactive process, in which the user draws the lines and polygons in one panorama, and completes it by projecting the current model onto the new panorama and recovering the new parts of the model subject to the constraints derived from the scene regularities.

The approach presented by El-Hakim (2002), in contrast, uses a small number of perspective images from widely separated views (e.g. photos taken by tourists), and automatically deals with occlusions and unmarked surfaces. In this approach, image registration and segmentation are carried out by the user in an interactive way. This is followed by an automatic corner detection and correspondence. In this approach, in average, 80% of the points are generated automatically, by applying an edge detector and sampling new points on the edges.

In the interactive solution proposed by Sinha et al. (2008), the 3D model is reconstructed from a collection of unordered photographs. In this approach, camera poses are estimated using SfM methods. This process also delivers a sparse 3D point cloud which is later used (together with vanishing directions) in the modeling step for the estimation of plane normal vectors and depths. Vanishing points are estimated automatically, by the automatic estimation of lines in the images. The system then

uses this geometrical information for the upcoming interactive modeling steps. The modeling process includes drawing the 2D outline of the planar sections over the photographs, which are automatically converted to 3D polygons. By projecting the image onto the created 3D surfaces, the model not only becomes photorealistic, but the user can also easily edit the sketches or draw lines which are observed even in one image. Figure 4.3 shows the described system in use for generating photorealistic 3D models.



Figure 4.3 – An interactive system interface for generating 3D photorealistic models from unordered photographs. Top (from left to right): input photographs, 2D sketching of polygons, geometric model and textured model. Bottom (example in an indoor scene, from left to right): input photograph, overlay of the model on the photo and geometric model. (from Sinha et al. (2008))

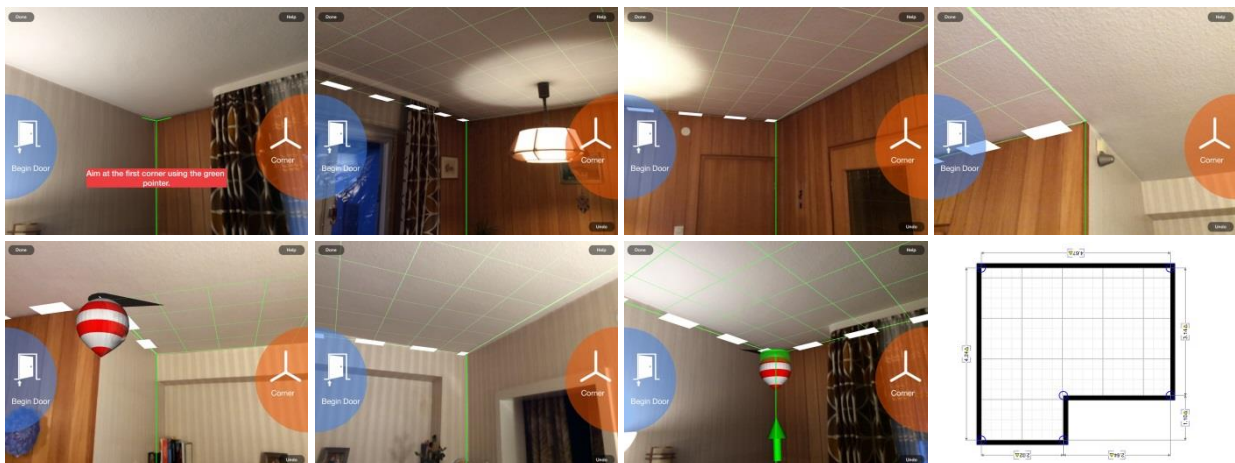


Figure 4.4 – Exemplary data acquisition and the resulting 3D model using a smartphone application MagicPlan (“Sensopia Inc.,” 2014), supported by Augmented Reality.

In another form of user interactions, Augmented Reality systems are used to fulfil some constraints during the data acquisition, as well as guiding the data acquisition task. Figure 4.4 illustrates an exemplary data acquisition process and the resulting indoor model using a smartphone application (“Sensopia Inc.,” 2014) supported by Augmented Reality. In this application, the user stands on a single position inside the room, and takes photographs of only the room corners, while interactively coincides the corners with markers indicated on the device screen. However, this application does not rely only on photos, and also benefits from other device’s sensors such as compass and gyroscope to recover a 2D plan.

User interactions are replaced by making assumptions about the scene geometry in Furukawa et al. (2009a), in order to achieve a fully automated approach for indoor reconstruction based on state-of-the-art computer vision algorithms. In this work, similar to the work presented by Sinha et al. (2008), camera poses and image registration is performed based on the SfM method. The approach then imposes Manhattan-world constraint on the scene, which is typical for many indoor scenes. Based on this assumption, in the next step, a stereo algorithm specifically designed for Manhattan-world scenes is used to derive axis-aligned depth maps from the images (Furukawa et al., 2009b). Afterwards, the depth map and the sparse point cloud resulting by the SfM method are merged to extract a simplified axis-aligned mesh model. After some refinement steps applying on the vertex positions up to sub-voxel accuracy constrained with Manhattan-world assumption, the 2D plan is computed. Examples of a floor plan and a 3D model generated by this approach are depicted in figure 4.5. In this example, a simple and consistent model is generated from a sparse multi-view stereo point cloud and a noisy depth model, thanks to the refinement steps and the Manhattan-world constraining.

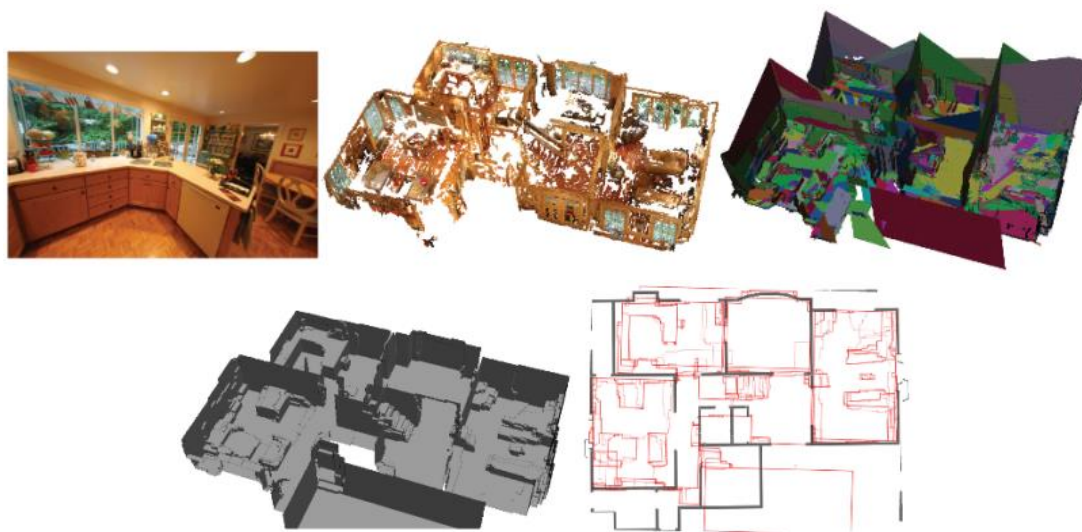


Figure 4.5 – Input, interim and final results for indoor reconstruction from a sample dataset, using the approach described by Furukawa et al. (2009a). From left to right and top to bottom: Input image, textured points, Manhattan-world depth map, final 3D model and generated floor plan. (from Furukawa et al. (2009a))

4.2.2. Range-Based Modeling

Range-based approaches for modeling of building interiors use geometrical information collected by laser scanners, range cameras and dense image matching to represent the indoor space in terms of surfaces and volumes. In general, this process consists of different phases, such as data acquisition, data pre-processing (including registration, outlier and noise removal, furniture removal, etc.), segmentation of the point clouds and geometric modeling (line or plane fitting, topological corrections, possibly extraction of semantics such as openings, etc.). In this chapter, the special focus is on the geometric modeling process.

Fitting planes and other geometric primitives to collected point clouds is the main approach developed for the reconstruction of building interiors from measured point clouds. Although in commercial solutions such as Cyclone (“Leica Cyclone,” 2014) the fitting is fulfilled in a semi-automatic manner, there are researches pointing to the automation of this process. In Toldo and Fusiello (2008), a novel and robust algorithm for fitting of geometric primitives to point clouds containing noise and outliers is presented. The algorithm (so called J-Linkage) is based on a random sampling scheme (as in RANSAC (Fischler and Bolles, 1981)) and Jaccard distance, and automatically groups the point cloud into corresponding clusters considering the preference set of each point, i.e., the set of models to be satisfied by the point within a tolerance. In other words, the models (characteristic functions) can be considered as conceptual representations of the points; therefore, the points are clustered in a conceptual space. Figure 4.6 shows an exemplary output of this algorithm applied on a room point cloud, using the implementation provided by Toldo and Fusiello (2014). The algorithm is robust in fitting applications, due to using powerful statistical tools; however, it still cannot be considered as a sufficient solution for the geometric modeling of the building interiors, as it does not control the topological correctness of the generated model. Another example of primitive shape detection using RANSAC is given by Schnabel et al. (2007).

The plane fitting task is fulfilled by the linear and rotational plane sweeping algorithm in Budroni and Böhm (2009). In their approach, the room is considered to be a Manhattan-world scenario, and therefore, the main wall directions are perpendicular. A main direction in this approach is recovered by the analysis of the number of points laid on the rotating sweep plane located at different random positions. The walls are then identified based on a linear sweep along the main room direction, followed by a cell decomposition process. This process, however, requires the acquisition of ceiling and floor points. Floor and ceiling are identified by a linear plane sweep in the vertical direction, and the analysis of the point height histogram. Existence of noise, outliers and clutter has no impact on the output, as far as they do not gain the peaks in the resulting histograms. The proposed algorithm is robust in applications satisfying the Manhattan-world constraint. Figure 4.7 shows the 3D model reconstructed by this approach, for the same dataset used in the previous example.

The Manhattan-world assumption is ruled out, and therefore wall detection becomes more general in the approach presented by Previtali et al. (2014). In this approach, besides the geometric reconstruction, semantic information such as location of doors and windows are recovered, assuming a known location of the laser scanner. For this purpose, the approach first detects and segments the planes constituting the room outer shell, based on the RANSAC algorithm and some topological measures. By recovering the ceiling and floor points based on the height histogram analysis of horizontal plane segments, a first floor plan is inferred by projecting the ceiling or floor points onto a horizontal plane, and a follow-up cell decomposition process. The floor plan then supports the extraction of walls amongst all the vertical segments (including those produced by clutter), by finding the vertical plane segments belonging to the boundary of the floor plan. To detect doors and windows, openings inside the walls are looked for. Holes produced by clutter and occlusions are distinguished

from doors or windows using a ray-tracing algorithm (similar to Adan and Huber (2011)), assuming doors or windows are not occluded in the point clouds, as well as the scanner position is known. Doors are distinguished from windows, if their corresponding holes intersect the ground. Figure 4.8 depicts an example of a reconstructed 3D model based on the mentioned approach for a scenario with an arbitrary shape. It should be noted that although this approach is compatible with more general room shapes, the collection of ceiling or floor points is still necessary for the cell decomposition process. While this is not an issue for data acquisition with TLS, indoor mobile mapping systems can face problems regarding data acquisition of such featureless and broad surfaces.

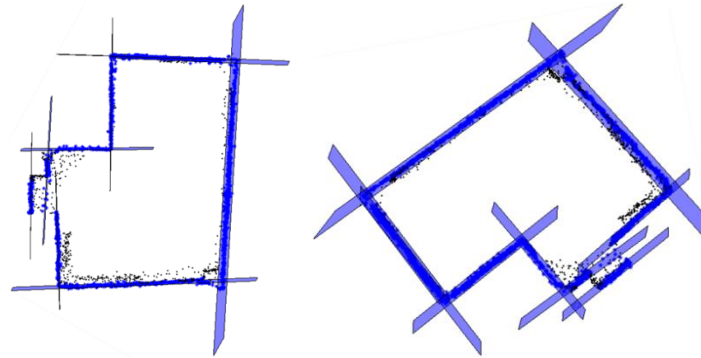


Figure 4.6 – Plane fitting to a sample room point cloud using the algorithm presented by Toldo and Fusiello (2008).

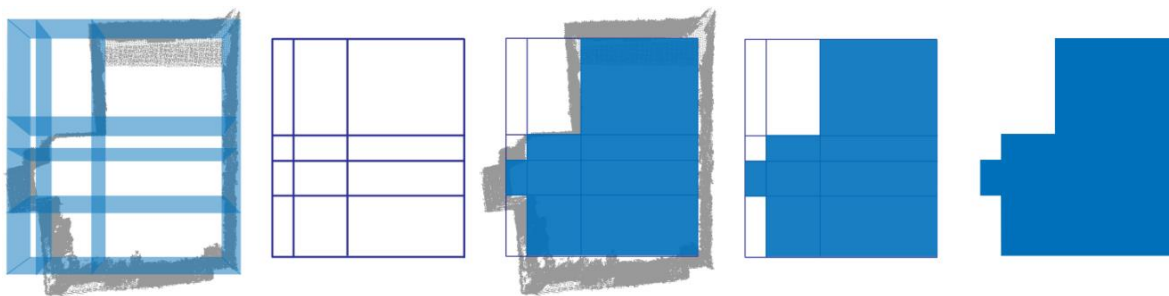


Figure 4.7 – 3D reconstruction using the plane sweep followed by a cell decomposition process. (from Budroni (2013))

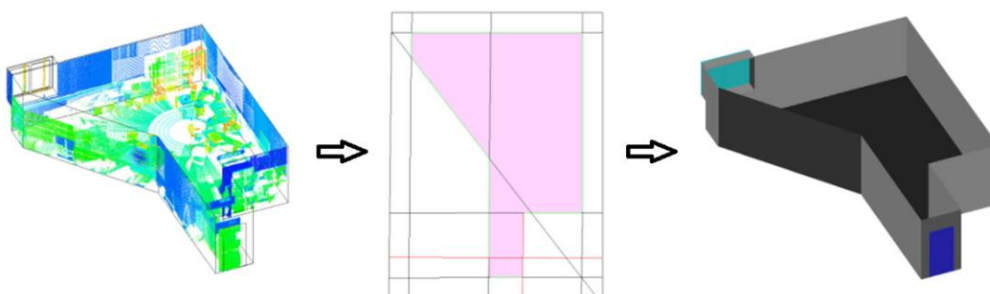


Figure 4.8 – Sample 3D model with semantic information automatically derived from a laser scanner point cloud. From left to right: laser point cloud, binary occupancy map (cell decomposition) and 3D model with distinguished door and window features. (adapted from Previtali et al. (2014))

There are also approaches that focus on the reconstruction of 2D floor plans which are then convertible to 3D models by a simple extrusion. Besides that, in many applications, a 2D floor plan is the required output. A related work in this field is presented by Okorn et al. (2010). This approach recovers the 2D plan of the building interiors from a given 3D point cloud of the facility, based on the projection of the points onto a horizontal 2D plane. The projection of the points forms a histogram

from the point density, which is used for the extraction of line segments corresponding to walls using a Hough transform. In this approach, clutter is removed based on the point height histogram. Moreover, it is taken into account that walls have a higher intensity in the 2D point density histogram. Figure 4.9 shows an exemplary output of this algorithm for one floor of a building. Although many of the line segments are correctly assigned by this approach, still the resulting 2D plan does not represent a topologically correct model. Moreover, this approach does not deal with occlusions.

The aforementioned approach is semantically enriched in Adan and Huber (2011) by detection and modeling of wall openings, and filling the occluded regions. In this approach, first, walls are detected using a Hough transform just similar to that described in Okorn et al. (2010). Wall occlusions are then classified into occupied, empty or occluded, using a ray-tracing algorithm, assuming that the 3D data is obtained from fixed and known locations. In the next step, door and windows are detected using a learning-based method that extracts and analyzes rectangular openings. Finally, occlusions not within openings are reconstructed based on a hole-filling algorithm (see figure 4.10).

The approach presented by Valero et al. (2012) improves the geometric modeling of the works presented by Okorn et al. (2010), as well as Adan and Huber (2011), using a more robust wall detection algorithm supported by some topological analyses. They firstly use a similar algorithm to derive the room's boundary in 2D using the Hough transform. Due to the high density and low level of noise in the input data collected by the laser scanner, each wall is represented by a corresponding edge in the extracted room's boundary, which is equivalent to a vertical plane in 3D. This supports the segmentation of points into individual walls by the analysis of the point-to-plane distances. A boundary representation model (planar surfaces) is then generated by the calculation of the best plane fit to the segmented points. Finally, the intersections between the planes are computed, considering the topological relationship between the already estimated boundary edges in the 2D projected image (figure 4.11, top right). The process steps are depicted in figure 4.11 for a sample room point cloud. It can be observed that for a successful process, having a dense point cloud of the room ceiling or floor is necessary to robustly estimate the room's boundary.



Figure 4.9 – 2D floor plan from point density histogram. From left to right: 2D point density histogram, estimated Hough lines and overly with ground truth (labeling based on detected lines): green and blue line segments are modeled by the algorithm, while red segments are missed. (adapted from Okorn et al. (2010))

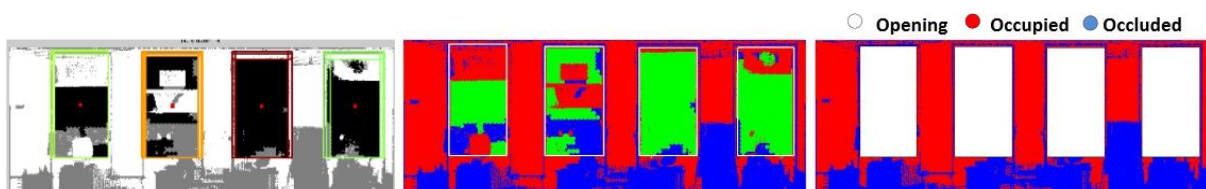


Figure 4.10 – Opening detection. From left to right: opening detection using a machine learning model, openings superimposed on a 2D projection image and final marked out openings. (from Adan and Huber (2011))

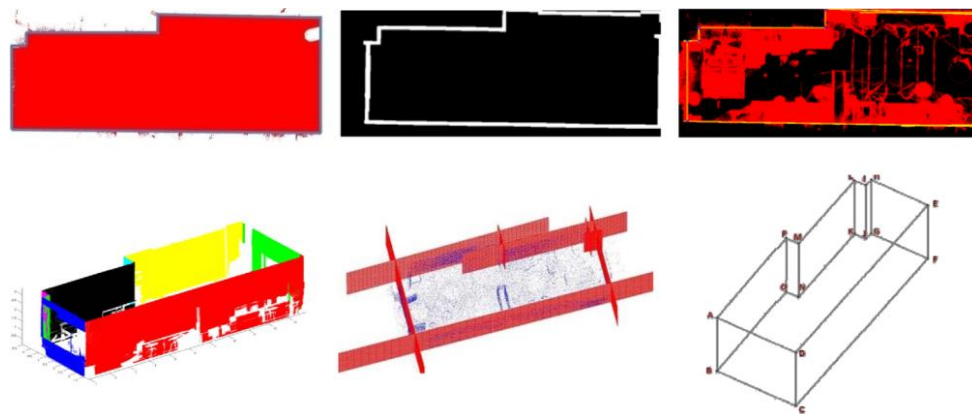


Figure 4.11 – From point cloud to a boundary representation model. From left to right and top to bottom: projection of the points onto a horizontal plane, detected edges, boundary detection using the Hough transform, point cloud segmentation, estimation of best plane fits and the final boundary representation model. (adapted from Valero et al. (2012))

4.2.3. Modeling Based on Architectural Drawings

Architectural drawings are essential for the design and construction of buildings. They are made according to a set of conventions including symbols and annotations. Graphics recognition techniques for the analysis of available 2D architectural floor plans can deliver geometric and semantic information to reconstruct 3D models. Such approaches for 3D modeling can be classified as iconic, if the underlying floor plan represents the as-built state, and therefore indirectly require the real measurement of the building interiors. But on the other hand, they might be considered as symbolic, if they are linked to an as-designed plan, which does not necessarily represent the as-built status.

The complexity of such modeling approaches depends on the provided input information, which can be of different level-of-details, as well as very different formats, ranging from CAD documents to scanned paper drawings. For instance the systems developed by Horna et al. (2007), Lewis and Séquin (1998) and Lu et al. (2007, 2005) take the floor plans in digital version as input, and focus on derivation of geometrical features, eventually semantic information and topological correction. But on the other hand, many floor plans are recorded as paper documents or scanned images. Therefore, the other category of approaches, such as those presented by Ah-Soon and Tombre (2001, 1997) and Dosch et al. (2000), try to extract geometric and semantic information using a raster-to-vector conversion process, supported by image processing and pattern recognition techniques. Another challenge in this modeling approach is differences in drawing conventions, as well as the architects' creative way of generalization and representation. Therefore, user interaction in the analysis of the drawings becomes unavoidable, due to the limited size of the predefined symbols and libraries.

According to a survey study presented by Yin et al. (2009), most of the available approaches in this field share a similar pipeline, however, they are different in terms of employed algorithms and strategies dealing with different process steps. In general, the main pipeline consists of image parsing (for the extraction of semantic information through text extraction and symbol detection), derivation of geometrical information (including noise removal, image processing, template matching and detection of architectural components such as walls, windows and the outer building shell), as well as topological corrections.

This section describes in detail the approach presented by Peter et al. (2010), in which 3D indoor models are extracted from photographed evacuation plans. The resulting 3D model will later serve as the case study in demonstration of the capability of our reconstruction approach in the refinement of

available coarse floor models (see chapter 7). The existence of evacuation plans is compulsory in many countries for public buildings such as hospitals, universities, hotels, etc. Therefore, the accessibility to these maps makes this approach more suitable for 3D modeling by the mass (crowdsourcing). The approach first enhances the photograph to compensate for bad light condition to increase the image quality using automatic white balancing and Wallis filtering (Wallis, 1976). Afterwards, a binarization process is carried out using a single threshold so that the image can be segmented into closed polygons for further topological analyses, such as distinction of rooms and single stairs. The stair candidates are also used for the estimation of the floor height considering a standard value for a single stair's height. The main lines in the image are then estimated in order to identify the building boundaries, using the Canny edge detector (Canny, 1986). Matching the identified boundary of the building with the available outer shell contour extracted from city maps further enables the derivation of geo-referenced metric models as well as computation of projective transformation parameters to convert the image coordinates into the world coordinate system. It additionally enables the removal of the perspective distortions caused by photography and cropping the image. Since parts of the plan might be occluded by symbols, symbol areas have to be detected and removed. Symbol areas are detected by template matching considering the image legend for the plan. This technique is replaced in their follow-up work (Peter et al., 2013b) by a more general and efficient method called Color Structure Code segmentation, in which symbols are detected based on their color properties ("Color Structure Code," 2014). The image is then vectorised by the estimation of the skeleton of the cleaned binary image. The occluded lines (by symbol areas) then have to be bridged by the prolongation of free end node edges identified in the vectorised image. The mentioned image processing steps are depicted in figure 4.13. The resulting vectorised image, which is now the 2D floor plan of the building, is further refined by detection of doors, using the indoor positioning system described in section 3.2.2.1. Doors are detected by finding the intersection of the user's track as well as evacuation routes and existing walls within an appropriate intersection angular range. The 2D plan is finally converted to a 3D model by an extrusion, having the floor height available (see figure 4.14). The initial point of the user's track, which is required for indoor positioning, can be computed by detection of the "you are here" symbol using template matching. However, the distance between user to the evacuation plan can be computed only by having the plan dimensions or by map matching of the user's route. Additionally, the user is able to collect geo-referenced semantic information in an OpenStreetMap-like fashion, i.e. collection of geo-tagged photos which will be added to the map in a post-processing step, e.g. location of fire extinguishers, doors, windows, room number, etc. The mentioned steps are summarized and depicted in figure 4.12.

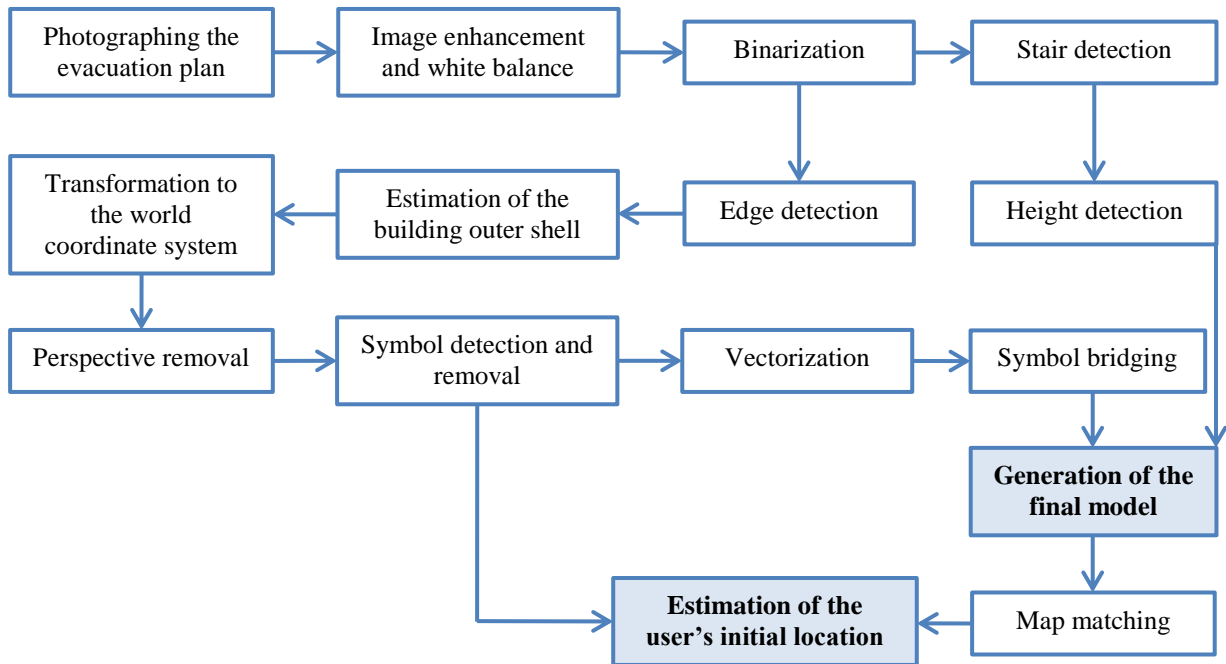


Figure 4.12 – The main procedure to convert photographed evacuation plans to 3D models.

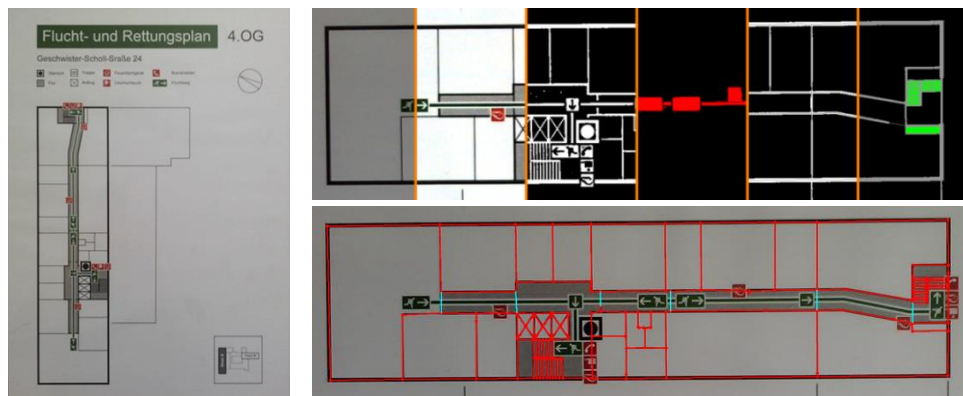


Figure 4.13 – Left: a photographed evacuation plan; Upper right: image processing steps (left to right): original image, color enhancement, binarization, symbol detection using color segmentation or template matching, symbol bridging and vectorization, and stair detection (green); Lower right: vectorized floor plan. (adapted from Haala et al. (2011), Peter et al. (2013b) and Peter et al. (2013b))

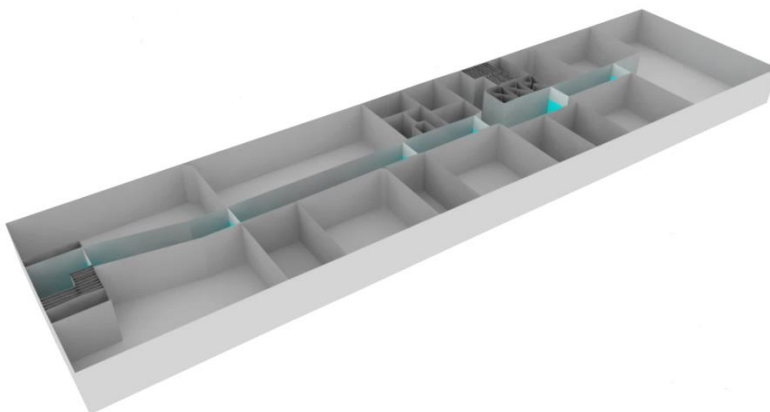


Figure 4.14 – Generated 3D indoor model corresponding to figure 4.13.

4.3. Symbolic Approaches

Symbolic (top-down) approaches can recover geometric models based on hypotheses, in case of having incomplete or erroneous data, where the iconic modeling approaches fail or deliver invalid results. The hypotheses are derived based on the knowledge inferred from the rules governing the regularities and relationships in the arrangement of structure elements. It is similar to a language's grammar, in which words are put together according to grammar rules to construct a sentence. A shape grammar rule governing a special design principle can be derived, for example, from the analysis of a bottom-up modeling process, where the data is of sufficient accuracy and density to deliver valid results.

Grammar-based approaches have successfully been used in the reconstruction of LOD3 models, by the integration of façade models to available LOD2 building models (e.g. see (Becker, 2009; Müller et al., 2006)), as well as in indoor applications that reconstruct LOD4 models, according to CityGML representation standard (e.g. see (Becker et al., 2013; Gröger and Plümer, 2010; Khoshelham and Díaz-Vilariño, 2014; Philipp et al., 2014)). This section shortly introduces available grammar-based approaches used in indoor applications.

In grammar-based modeling, mainly spatial grammar rules (particularly split rules) are used to reconstruct the more complex shapes from basic geometric primitives (e.g. splitting boxes and faces to their constructive sub-spaces) (Müller et al., 2006; Wonka et al., 2003). However, it does not guarantee the topological correctness of the models caused for instance by gap or overlap of the constructive elements. This problem is addressed by Gröger and Plümer (2010), and a solution is presented by explicit constraining based on topological concepts (such as adjacency, parallelism and perpendicularity), setting up a rout graph as a benchmark for the consistency (coincidence of doors) and use of semantics (such as distinction of rooms, hallways, staircases, as well as doors and ceilings floors and walls). Such criteria define a limited number of rules to subdivide the space and reconstruct the building interiors in more detail and rich semantics. The work is the first grammar-based approach adapted for indoor applications, however, the grammar rules have to be defined manually for every case study.

Grammar rules are derived automatically from observations in Becker et al. (2013), so that it becomes flexible to support the reconstruction of more indoor scenarios with arbitrary shapes. Their grammar design assumes building floors are composed of two parts: a hallway part which is designed for a convenient access to rooms, and a non-hallway part consisting of individual rooms mostly arranged in a linear sequence parallel to the hallway. Therefore, their grammar is a combination of two separate rules: a simulation of plants growth pattern (a so-called Lindenmayer system) for the hallways part, and split rules for the reconstruction of rooms.

To create an instance of an individual grammar which is able to reproduce a specific building interiors, observations are required. A grammar instance can be generated for example from an available floor plan or a collection of odometry data. In the example provided by Peter et al. (2013a), the indoor model derived from a photographed evacuation plan yields a high level grammar instance using the reverse modeling process. In Becker et al. (2013) and the corresponding extended work (Philipp et al., 2014), the hypotheses about the indoor geometries are generated from the observation of 250 odometry traces collected by a foot mounted MEMS IMU (see figure 4.15). By means of constraints derived from the trace data, door locations are estimated. It is assumed that each room has only one door, which is the intersection of a trace with the corresponding wall. Therefore, it can also be assumed that walls can be located only between the door locations. In their example, 116 rooms are reconstructed from the trace data with an average width error of around 2 meters. Moreover, the room

sizes are estimated based on the grammar and the probabilities assigned to them, together with constraints, conjointly.

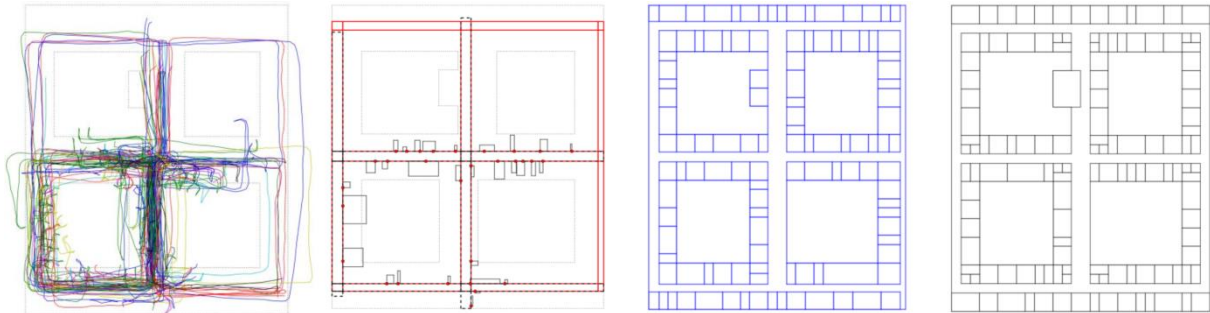


Figure 4.15 – Grammar-based reconstruction of an indoor scene based on the observation of 250 odometry traces. From left to right: position traces, estimated door locations and hypothesized hallways (rooms are reconstructed only from traces; without the use of hypotheses), complete model with hypothesized rooms and the ground truth. (adapted from Becker et al. (2013))

In Khoshelham and Díaz-Vilariño (2014), the shape grammar is derived based on an architectural indoor design concept known as Palladian grammar (Stiny et al., 1978). The grammar rules in their work are automatically learnt from an available point cloud of the scene. The point cloud is first aligned with the main axes of the coordinate system based on the analysis of normal vectors. Floors are then distinguished based on the analysis of the point height histogram. Finally, grammar rules are defined and adapted automatically to each case study, based on the analysis of the x- and y-coordinates for each floor to find peaks corresponding to the location of walls and size of subspaces. This grammar-based learning approach, however, is only valid for Manhattan-world scenarios. Moreover, existence of ceiling points is necessary for the points-on-ceiling test that excludes invalid subspaces made by the integrating cell decomposition step. Figure 4.16 depicts the results of this reconstruction approach for a sample point cloud.



Figure 4.16 – Grammar-based reconstruction based on grammar rules derived from the point cloud. From left to right: collected point cloud, cuboid placement (top-view) with points-on-ceiling constraining and cuboid placement without points-on-ceiling constraining. (adapted from Khoshelham and Díaz-Vilariño (2014))

5. Automatic Reconstruction of Indoor Spaces

In the previous chapter, state-of-the-art approaches for the reconstruction of building interiors were presented. The chapter started with image-based approaches, and showed that a robust modeling using images needs user interaction. In other words, automation versus accuracy is a trade-off in image-based modeling. Although such approaches are very well suited for crowdsourcing applications due to availability, portability and the low-cost of cameras, for modeling of large interior spaces they become labor intensive tasks and nowadays, they are often not considered as optimum solutions.

Due to advances in the technology and production of range imaging systems in the last few years, range cameras have become very low-cost, accessible and portable, and therefore very popular for the collection of geometric information. In fact, although image-based approaches have been most economical and flexible for a long time (Remondino and El-Hakim, 2006), systems based on range measurements are becoming the standard solutions for the modeling of building interiors. However, reconstruction from point clouds is a very hard and nontrivial problem in case of having incomplete or noisy data. Moreover, existence of clutter and the complexity of the object geometry make the automation of the modeling process very challenging. Therefore, fully automated approaches are based on special assumptions and constraints to deal with the issues. However, new approaches have to be developed in longer terms to model finer details and more general shapes, and to be flexible enough in new and different environments (Tang et al., 2010).

In comparison with the mentioned range-based approaches, the approach presented in this work aims at modeling more general shapes of building interiors with fewer assumptions (e.g. no Manhattan-world constraint) and a high level of automation. This is fulfilled by transforming the modeling task from 3D to 2D space by projecting the points onto a horizontal plane, which enables the topological correction of the reconstructed model using morphological image processing techniques, topological analysis in 2D and graph analysis algorithms. The transformation to 2D will preserve the important information necessary for the modeling of the main structure elements such as walls and doors. Besides robustly dealing with a high level of input data noise, this approach also deals with occlusions to some extent. Significant occlusions caused by windows are handled in section 7.2, and the corresponding gaps are reconstructed using a learning-based approach, employing the information extracted from available coarse indoor models. Moreover, opposed to most of the modeling approaches mentioned in the previous chapter, the collection of the ceiling or floor point cloud is not necessary in this approach, since no cell decomposition is required. Collecting the entire ceiling or floor data can be a challenge for mobile mapping systems, due to the poor texture and 3D information of such flat surfaces required for the registration of captured data from different viewpoints.

This chapter explains in detail the presented reconstruction approach consisting of point cloud pre-processing and geometric modeling steps, using a pilot study which is affected by point clouds misalignment errors, noise, small and large gaps, and at the same time has an arbitrary shape (in contrast with Manhattan-world scenarios).

5.1. Point Cloud Pre-Processing

Pre-processing of the point cloud in this work includes outlier removal, downsampling, noise removal, point cloud leveling and finally furniture and clutter removal.

5.1.1. Outlier Removal

In comparison with TLS, data collected by range cameras contain more noise as well as outliers due to measurement errors. This affects the accuracy of further processing steps which include normal vector estimation and estimation of walls. In the first pre-processing step, outliers are removed using a statistical outlier removal filter implemented by the Point Cloud Library (PCL) (Rusu and Cousins, 2011). The filter works based on the distribution of the distances between the neighboring points. The mean distance to K-nearest neighbors is computed at each point. Assuming a Gaussian distribution for the distances, points corresponding to the mean distances outside of an interval defined by the global mean and standard deviation are removed using a one-tailed normal distribution test. Figure 5.1 depicts the mean distances computed for an exemplary scene. In this example, outliers are removed based on a 1σ one-tailed normal distribution test:

$$\text{dist} \sim N(\mu, \sigma^2) \Rightarrow P(\text{dist} \leq \mu + \sigma) = 84.1\% \quad (5.1)$$

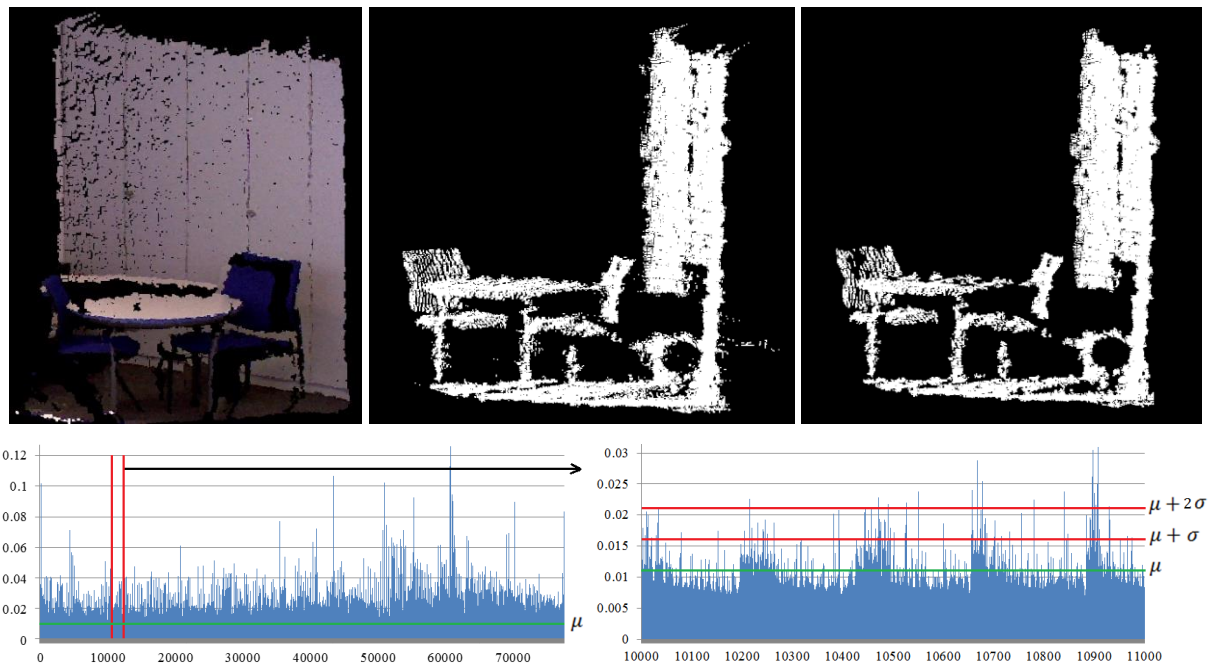


Figure 5.1 – Top: statistical outlier removal (9K out of 73K points are removed, equivalent to the 1σ confidence level normal distribution one-tailed test); Bottom: corresponding mean distance (in meters) to the 20 nearest neighbors versus point index (mean: 0.011m, standard deviation: 0.005m).

5.1.2. Downsampling

Point clouds collected by range cameras are usually very dense. The number of points is increased very fast soon after data acquisition starts; each range image frame captured by Kinect (for Xbox 360) delivers $640 \times 480 \approx 300\text{K}$ 3D points, or $1920 \times 1080 \approx 2\text{Mio}$ points by Kinect V2. Reconstruction programs therefore can face difficulties handling a large number of points collected from large spaces. In order to efficiently manage the memory, as well as achieve a uniform point density, the registered point cloud is downsampled by a voxel grid filter implemented by the PCL software library, in which points are replaced by the centroid of the corresponding bounding voxel generated by an Octree data structuring process (see figure 5.2). The voxel size can be set based on the overall noise of the registered point cloud (e.g. 3-5cm in case of using Kinect), or for example the maximum allowed tolerance specified by the adapted standard for building reconstruction (e.g. surface flatness tolerance suggested by DIN 18202 standard).

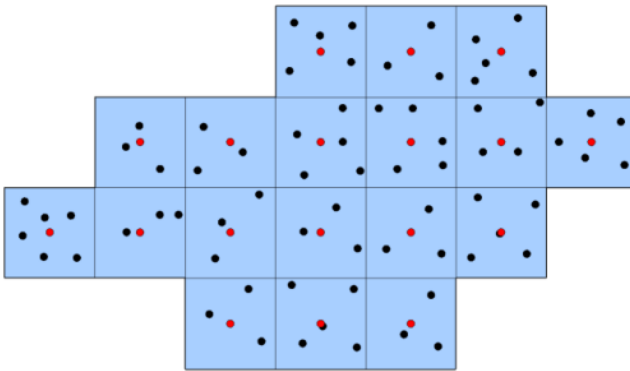


Figure 5.2 – Voxel grid filtering: points inside each voxel are replaced by the centroid of the corresponding voxel (red points).

5.1.3. Noise Removal

Noise in the point cloud causes erroneous object fitting or feature extraction. Although the wall estimation algorithm used in the following modeling process is capable of dealing with noise in the point cloud to some extent, noise removal significantly improves the accuracy of feature detection in modeling. The point cloud is smoothed using the moving least squares approximation algorithm, originally introduced by Lancaster and Salkauskas (1981), and implemented by the PCL software library. As described by Nealen (2004), the idea of the moving least squares algorithm is to start with a weighted least squares surface estimator (a degree n polynomial) for an arbitrary fixed point, in which weights are proportional to the neighboring points distance within a given radius. The point is then moved over the entire parameter domain, where a weighted least squares fit is estimated for each point individually, in order to estimate the overall surface. The global function $f(x)$ is obtained from a set local functions $f_x(x)$ that minimize the following cost function:

$$f(x) = f_x(x), \sum_{i \in I} \theta \cdot \|x - x_i\| \cdot \|f_x(x_i) - f_i\|^2 \rightarrow \min \quad (5.2)$$

in which θ is the weight function tending to zero at infinity distance. During the process, small holes can be filled by resampling techniques, e.g. based on a higher order polynomial interpolation. This can further remove the “double walls” artifacts caused by erroneous registration of multiple scans. Figure 5.3 depicts an example in which an overall noise of 34mm is reduced to 25mm by local plane fitting using a moving least squares process within the search radius of 15cm.

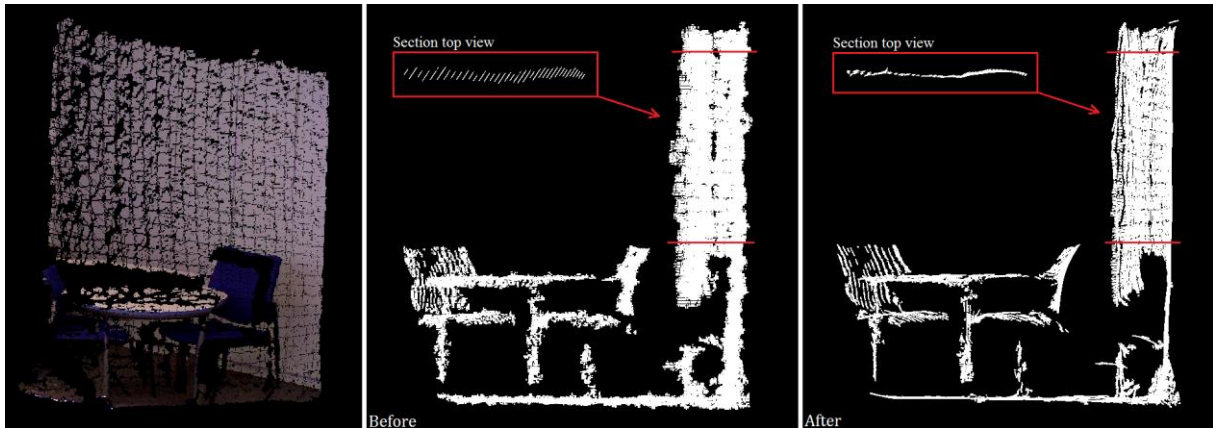


Figure 5.3 – Before and after noise removal. In the cross section before the noise removal, the limited resolution of Kinect disparity measurements is noticeable as a stripe pattern.

5.1.4. Leveling the Point Cloud

The resulting point cloud has to be leveled for the upcoming processing steps, i.e. generation of the point height histogram and projection of points onto a horizontal plane. The leveling is performed by the analysis of the point cloud normal vectors. Since most of the surfaces in man-made scenes are aligned either horizontally or vertically, it is possible to cluster the normal vectors into two main groups. Assuming the vertical axis of the point cloud's local coordinate system is inclined less than 45° with respect to the vertical axis of the world coordinate system, the group of horizontal and vertical surfaces can easily be distinguished, as they constitute a difference of 90° . The average of the normal vectors corresponding to horizontal (or alternatively vertical) surface points is then used to find the tilt, and thus level the point cloud. This procedure is an iterative process; in each step, after leveling the point cloud based on the estimated tilt, the classification of horizontal and vertical surface points is updated based on the new (recently transformed) normal vectors. Figure 5.4 depicts an example of a normal vector histogram for a sample point cloud after leveling.

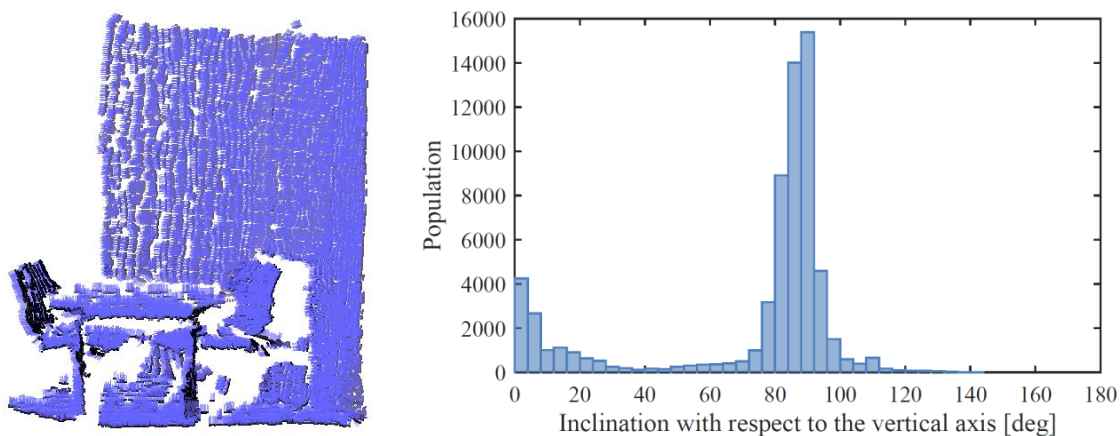


Figure 5.4 – Left: computed point normal vectors. Right: histogram of the inclination of the normal vectors with respect to the vertical axis after leveling the point cloud.

5.1.5. Height Estimation and Furniture Removal

The room height information enables the extrusion, and therefore conversion of generated 2D to 3D models. After leveling the point cloud, it is possible to estimate the room height by the analysis of the point height histogram. The floor and ceiling can be distinguished in the histogram by the identification of the smallest and largest local maxima, even if only small parts of them are captured (see figure 5.5). The number of histogram bins is corresponding to the voxel size used in the previous downsampling process. Therefore, the histogram values correspond to the surface area instead of the number of points, if the point cloud is downsampled by the voxel grid filter.

As was mentioned before, the presented 2D modeling approach is based on the projection of the points onto a horizontal plane. Therefore, similar to Okorn et al. (2010), in order to remove furniture and clutter, a cross section of the 3D point cloud which is less affected by clutter is selected. By doing so, no important information is lost, as the remainder of points corresponding to walls will provide the required information about the room shape. The height range can be selected based on a typical height of the furniture (points with heights less than e.g. 1 – 1.5m) as well as lights or ceiling fans (points laid within e.g. 0.5m under the ceiling). Figure 5.6 depicts an example of furniture removal using this concept for a sample room. It should be noted that in practice the furniture removal process is recommended to be performed supervised (or in an interactive way), since the existence of possible remaining clutter may have a large impact on the subsequent modeling steps, unless the modeling parameters are selected manually.

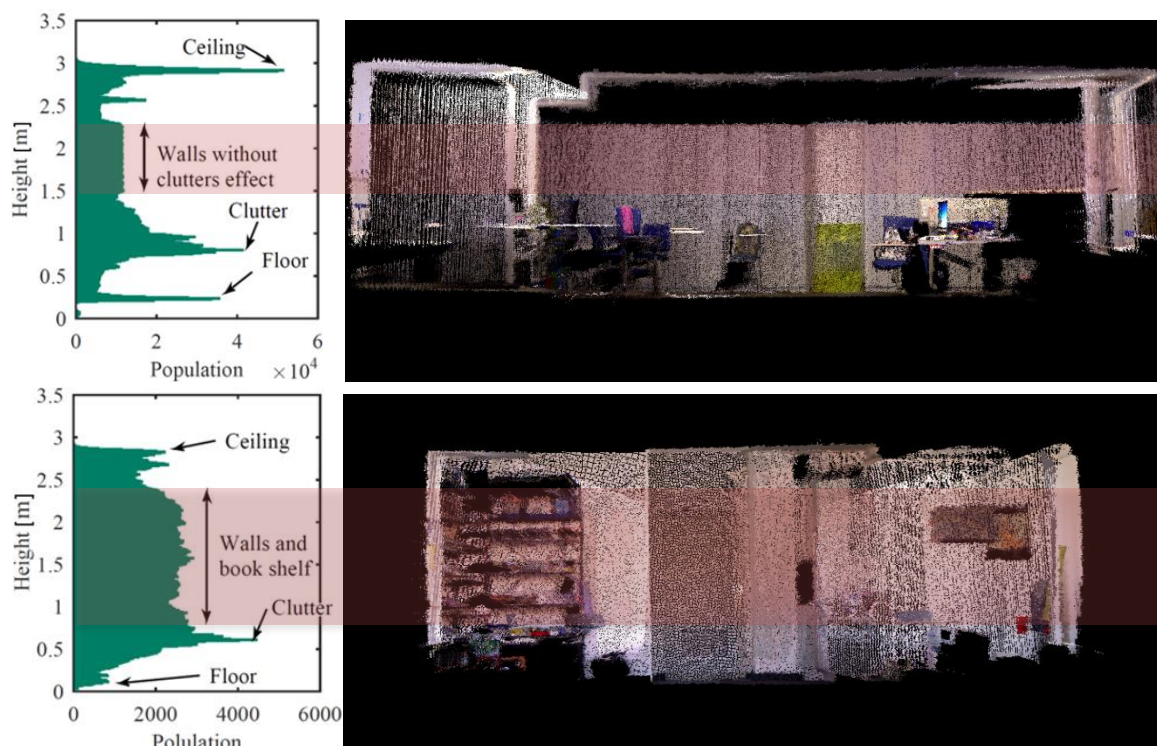


Figure 5.5 – Point height histograms and the corresponding point clouds.

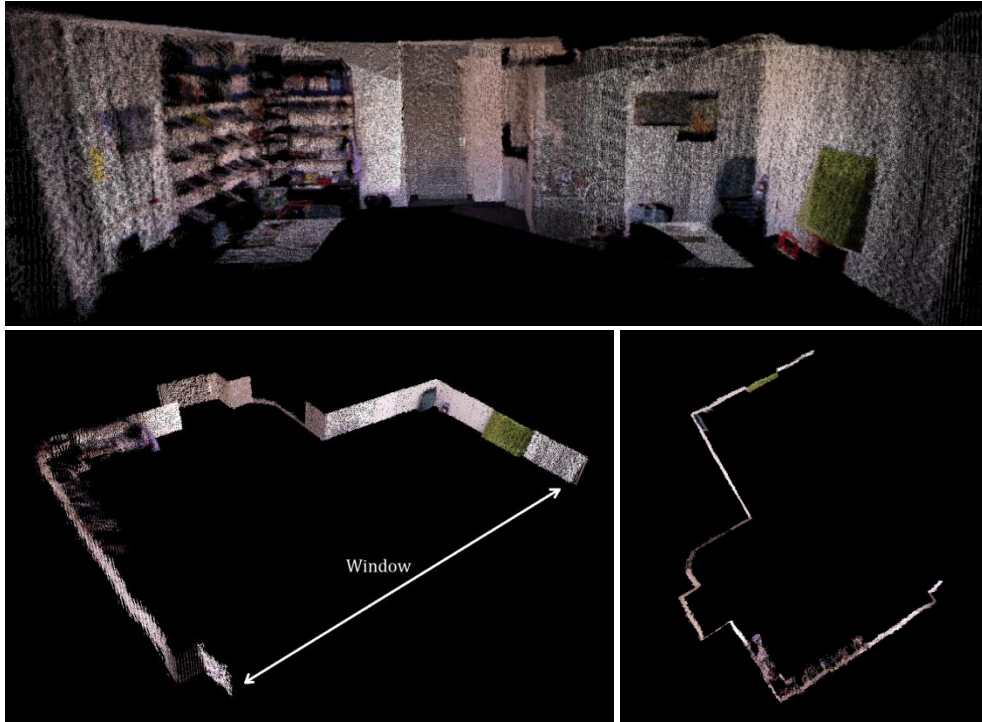


Figure 5.6 – Furniture removal based on a selective height filter. The top view of the filtered points (bottom-right figure) delivers information about the room shape geometry.

5.2. Reconstruction of Geometric Models

The mentioned pre-processing steps enable the 2D geometric modeling of individual rooms based on the orthographic (top-down) projection of resulting points onto the ground plane. Further modeling steps extract lines corresponding to walls and main structure elements within the 2D orthographic projected image and apply topological corrections.

5.2.1. Generation of Orthographic Projected Image

For the orthographic projection of points onto a horizontal plane (e.g. the ground plane), one can simply neglect the point heights in the corresponding leveled point cloud, generate a 2D grid with a predefined resolution and finally count the number of the points falling inside each grid cell. Alternatively, similar to Okorn et al. (2010), this task can be fulfilled more efficiently by counting the number of voxels above each 2D grid cell (the voxel grid has been already generated in the previous downsampling pre-processing step). The grid size has a direct effect on the accuracy of the final model, and therefore shall not be larger than the overall noise of the point cloud. The 2D grayscale orthographic projected image is computed based on the number of points inside (or alternatively the number of voxels above) the grid cells, using the following equation:

$$I(m,n) = \frac{N(m,n)}{N_{\max}} \times G \quad (5.3)$$

in which, $I(m,n)$ is the gray value of the grid cell at row m and column n , $N(m,n)$ is the number of the points inside (or voxels above) the corresponding cell, N_{\max} is the maximum value of $N(m,n)$ over the entire grid and G is the number of gray levels.

5.2.2. Binarization

This study only deals with modeling of flat surfaces; curved surfaces are not considered here. The modeling of such surfaces is fulfilled by the extraction of lines in the orthographic projected image corresponding to walls and main structure elements in 3D, using the Hough transform. Line extraction algorithms use binary images as input; therefore, the grayscale projected image has to be converted to a binary image. The binarization process may also remove the noise and clutter remaining from the pre-processing step, by choosing a correct threshold that removes lower gray values. The threshold can be chosen based on probabilistic approaches, having the average and standard deviation of the gray values. For example, assuming a Gaussian distribution for the gray values, a 95% confidence interval is defined by pixels having gray values larger than the threshold I_T equals to $\mu - 1.65\sigma$.

$$I \sim N(\mu, \sigma^2) \Rightarrow P(\mu - 1.65\sigma \leq I) = 95\% \quad (5.4)$$

A more perceptible threshold can be defined based on the ratio between the maximum possible height of remaining clutter and the height range of the selective height filter (equation (5.5)). The threshold gives the optimum results in case of having a uniform distribution of points, which is already fulfilled in the downsampling processing step.

$$I_T = G \left(1 - \frac{H_{\text{noise}}}{H_{\text{filter}}} \right) \quad (5.5)$$

In this equation, I_T is the grayscale intensity threshold, H_{noise} is the maximum possible height of remaining clutter, H_{filter} is the height range of the selective height filter and G is the number of gray levels. Figure 5.7 depicts the grayscale and binary orthographic projected images for an exemplary dataset. In this example, the binarization threshold is computed from equation (5.5), assuming H_{noise} being 5% of H_{filter} .



Figure 5.7 – Grayscale and binary orthographic projected image for a sample point cloud.

5.2.3. Morphological Image Processing

As depicted in figure 5.8, due to remaining noise in the range measurements, erroneous alignment and leveling of the point cloud, the projection of walls onto the ground plane is represented by shapes which are not necessarily straight lines, and have widths more than one pixel size. Therefore, in order to reduce the risk of ambiguous estimation of lines within the binary image by the Hough transform, the skeleton of the shapes is first extracted and considered for the line estimation. However, this process requires closing small holes inside the shapes in order to avoid obtaining unrealistic skeletons.

In mathematical morphology, a binary image A is closed by a structure element B (e.g. a 3×3 kernel), using a dilation followed by an erosion, as denoted by the following equation:

$$A \bullet B = (A \oplus B) \ominus B \quad (5.6)$$

where \oplus and \ominus correspond to the dilation and the erosion operators, respectively. In morphological image processing, closing (that removes small holes) and opening (that removes small objects) operators are the basics of the noise removal process.

After the closing process, shapes are thinned to one pixel width elements passing through the middle of the shapes using the morphological skeletonization, which is based on morphological opening (an erosion followed by a dilation). The algorithm iteratively erodes the image to remove the boundaries (while preserving end points), until the remaining structure has only one pixel width (Zhang and Suen, 1984). Figure 5.8 depicts the results of the mentioned morphological image processing steps for the previous example.

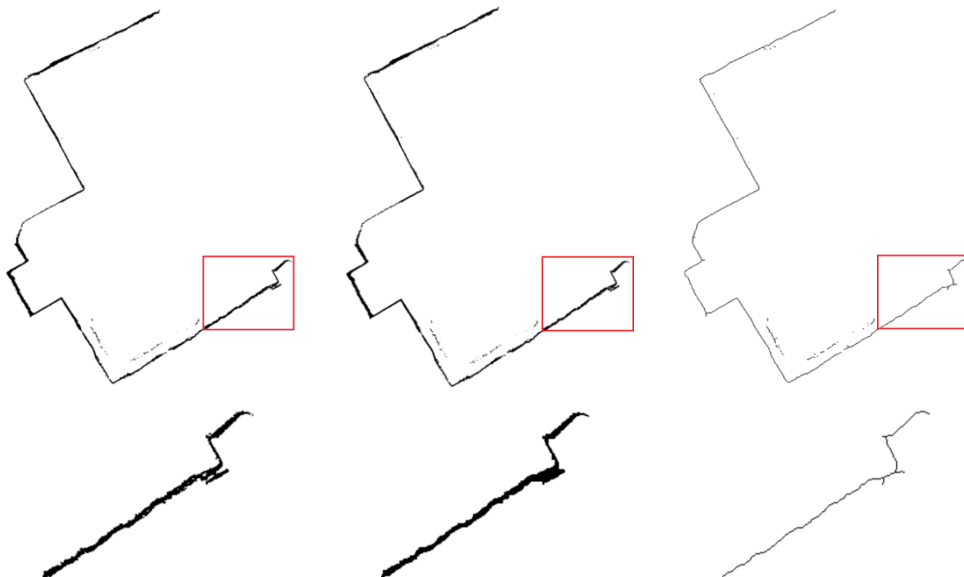


Figure 5.8 – Left to right: binary projected image, morphological closing and skeletonization.

5.2.4. Estimation of the Lines Representing the Walls in 2D

5.2.4.1. Line Extraction

The skeletonized image is appropriate for the extraction of straight line by means of the Hough transform (Duda and Hart, 1972; Hough, 1962). The idea of the Hough transform is to find all potential lines passing through each point, and select the candidates based on a voting procedure carried out in a parameter space. This work uses a variant of the Hough transform called progressive probabilistic Hough Transform (Matas et al., 2000), implemented by the OpenCV free software library (Bradski, 2000). This variant is an optimization to the standard Hough transform in speed and performance, by minimizing the number of points used in the voting process, while maintaining false positive and false negatives detection rates at the same level of the standard Hough transform. More details are provided in appendix D.

In the Hough transform process, parameters such as minimum allowed number of votes, minimum line length and maximum allowed line gap between points on the same line can be set. However, the parameters have to be suitable enough, so that small structures are not generalized during the line extraction process. Figure 5.9 depicts an example, in which the Hough lines are extracted from the skeletonized image in the previous example. In this example, parameters are selected as follows: minimum votes of 15 pixels (equivalent to 15cm) on a line, minimum line length of 15 pixels and maximum allowed line gap of 20 pixels (equivalent to 20cm). Although such kind of parameter selection results in the extraction of multiple smaller line segments for each wall, it will preserve almost all significant details and avoids the generalization. The effect of parameter selection on modeling results, as well as the stability of the selected parameters from one example to another is presented in the next chapter.

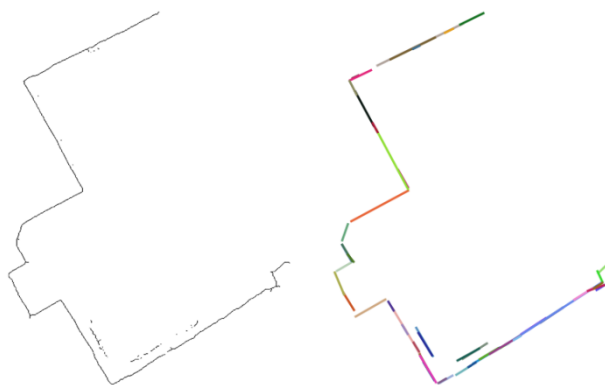


Figure 5.9 – Extraction of Hough line segments in a skeletonized image.

5.2.4.2. Clustering and Averaging the Line Segments

After the line extraction process, multiple smaller line segments corresponding to each wall have to be identified and averaged. The suggested identification process consists of three hierarchical clustering steps, in which line segments are grouped based on their orientation, distance to the centroid of the image and connectivity, respectively.

The first clustering step groups the line segments based on their orientation. Since the modeling approach is not limited to Manhattan-world scenarios, it takes into account all possible orientations

distinguished by a small threshold (angular resolution of the model). The threshold, however, shall be able to tolerate the noise in the orientation of the extracted line segments. Various solutions are proposed for clustering; here the K-means algorithm suggested by Lloyd (1982) is used, which is the most common in the computer science community. The algorithm groups n observations (x_1, x_2, \dots, x_n) into K sets $\{S_1, S_2, \dots, S_K\}$, so that the sum of the squared Euclidean distances between the observations and the nearest cluster centroid (mean) is minimized:

$$\sum_{i=1}^K \sum_{x \in S_i} \|x - \bar{x}_i\|^2 \rightarrow \min \quad (5.7)$$

The solution to the abovementioned equation is an iterative refinement process, in which two steps are repeatedly performed after each other. In the first step, each observation is assigned to the corresponding cluster with the smallest distance to its mean, so that the equation is satisfied. In the next step, a new centroid is computed and assigned to each cluster. The process is iterated until no more change is observed. In this approach, the initial set of centroids is usually selected randomly, and is updated during the process.

The number of clusters has to be pre-defined for the clustering algorithms. Estimation of the optimum number of clusters depends on the noise, distribution, as well as the resolution of the data, and therefore might be sometimes an ambiguous problem. However, in general there are different criteria that suggest the optimum number of clusters based on statistical approaches, many of which are summarized in Kodinariya and Makwana (2013). For instance, using the ‘‘elbow methods’’ (Thorndike, 1953), one can start the algorithm with one cluster, and increase the number of clusters until no more meaningful cluster is found (the corresponding chart has an elbow shape). This can be measured by the sum of the squared errors within the groups, or by the percentage of the explained variance (a goodness of fit index, equation (5.8)). In the previous example, as depicted in figure 5.10, having more than 3 clusters does not reduce the sum of squared errors within the clusters dramatically, nor does it increase the explained variance significantly. In this example, having 2 clusters results in a Manhattan-world scenario (97.5% percentage of explained variance). However, adding the 3rd cluster, takes the line segment with 70° orientation (highlighted in the figure) into account as well (99.5% percentage of explained variance). The percentage of explained variance is high in both cases, and both results are acceptable, depending on the required details and the modeling accuracy.

$$\text{Explained variance} = \frac{\text{Between groups variance}}{\text{Total variance}} = \frac{\frac{1}{(K-1)} \cdot \sum_{k=1}^K N_k \cdot (\bar{x}_k - \bar{\bar{x}})^2}{\frac{1}{(N-1)} \cdot \sum_{k=1}^K \sum_{i=1}^{N_k} (x_{k,i} - \bar{\bar{x}})^2} \quad (5.8)$$

In this equation, \bar{x}_k is the centroid (mean) of the k^{th} cluster, $\bar{\bar{x}}$ is the grand mean, N_k is the number of observations in the k^{th} cluster, K is the total number of clusters, $x_{k,i}$ is the i^{th} observation in the k^{th} cluster and N is the total number of observations. The between groups variance measures the variation of group means with respect to the grand mean; increasing the number of clusters, makes the between groups variance closer to the total variance. The explained variance in fact measures how good all the variances are explained, i.e. how good the predicted values fit the outcomes, in multivariate statistics.

In the next step, using a similar clustering process, line segments within each orientation cluster are grouped based on their distance to the origin of the projected image, so that the parallel line segments are distinguished (see figure 5.11). The distance threshold will be set automatically based on the

number of estimated clusters, or alternatively one can set it to a fix value depending on the modeling accuracy.

Line segments on the same direction are not necessarily adjacent; this can be caused by the situation where simply walls are nonadjacent, or due to occlusions in the point cloud that represents the same wall in multiple segments. The two cases are distinguished in the presented approach based on a tolerance according to the maximum expected size of occlusions in the data (except for the large occlusions caused by doors or windows). Therefore, a further clustering process is required to group (distinguish) the line segments laid on the same direction, but separated with a distance larger than the threshold. The threshold is set to 0.5m in the example depicted in figure 5.11.

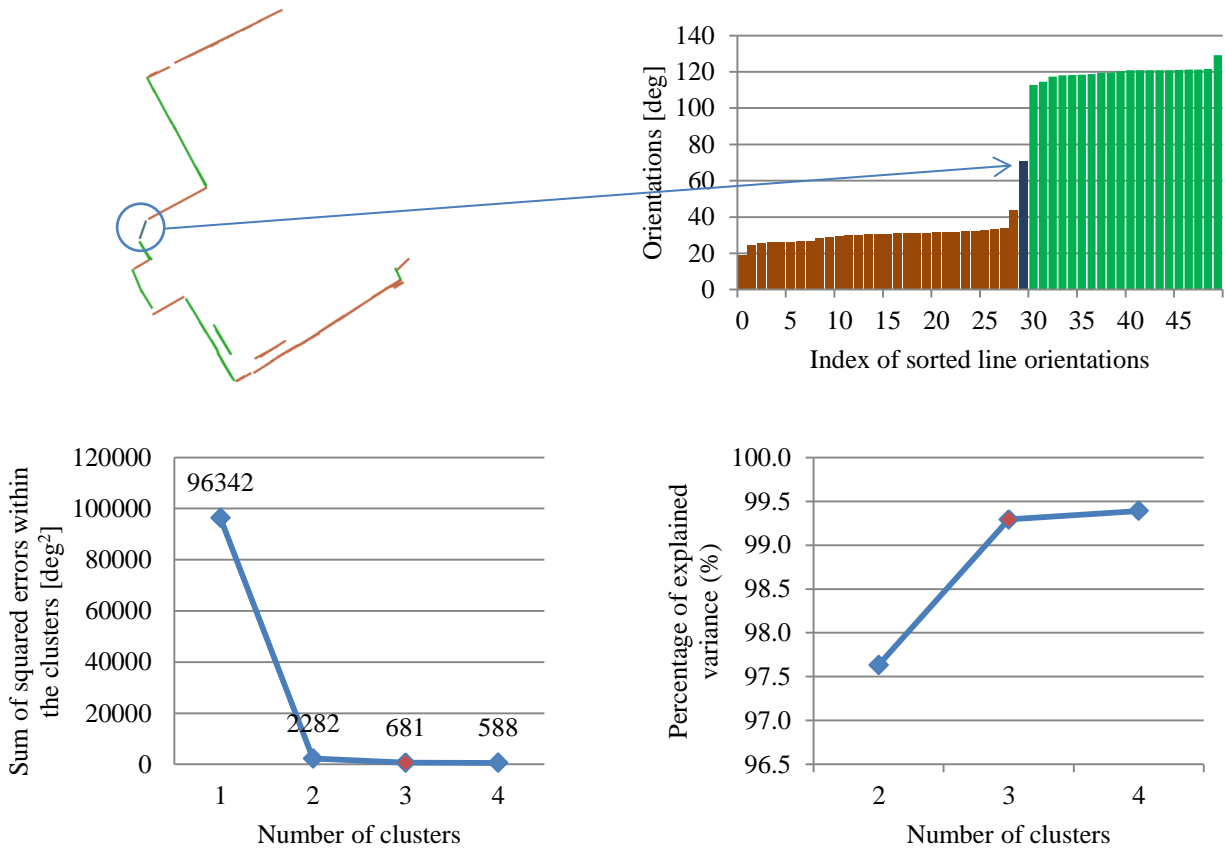


Figure 5.10 – Clustering the orientation of lines by the K-means algorithm.

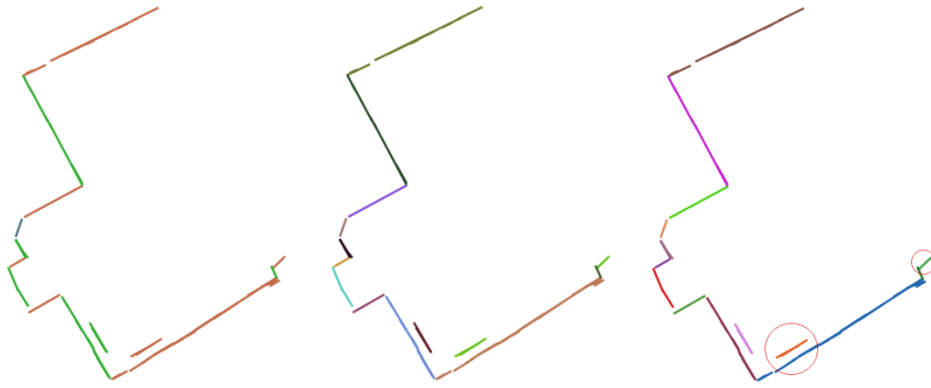


Figure 5.11 – Clustering the line segments (groups are distinguished by colors). Left to right: clustering based on the orientations, distinguishing parallel line segments laid on the same direction and finally distinguishing nonadjacent line segments laid on the same direction.

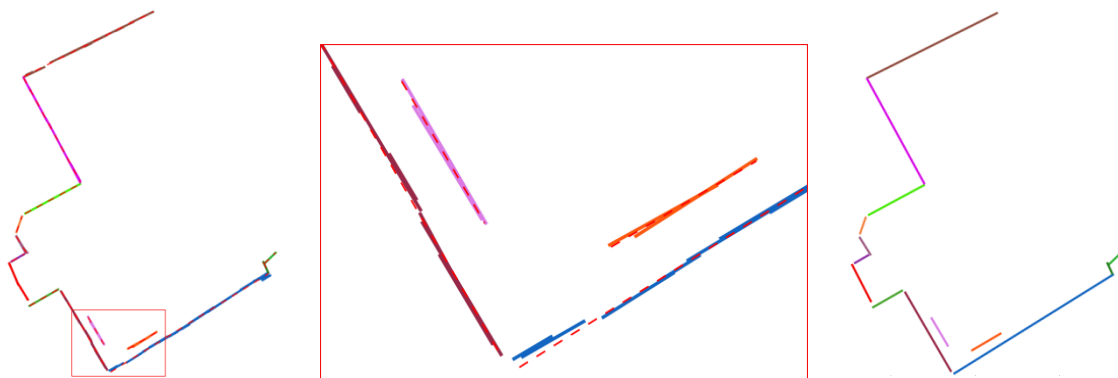


Figure 5.12 – Averaging the line segments corresponding to individual walls.

After the assignment of the line segments to individual wall groups, they can be averaged within the groups. Averaging is realized by sampling the line segments (converting them to points), calculating the linear regression passing through the samples and cropping the resulting line according to the start and end points in the samples. Figure 5.12 depicts the averaging results for the same example.

5.2.5. Topological Corrections

Due to the erroneous point cloud alignment and the remaining noise as well as occlusions in the projected image of walls, the resulting model depicted in figure 5.12 does not necessarily fulfill a topologically correct geometry. The line segments do not meet each other at the end points. Moreover, the angles between the adjacent line segments (walls) are sometimes clearly inaccurate. Therefore, the following topological corrections are proposed for a robust reconstruction from noisy or occluded data.

5.2.5.1. Refinement of the Orientation of Line Segments

Although the proposed approach is not limited to Manhattan-world scenarios, still in many man-made scenes walls can be recognized that are aligned parallel or perpendicular to each other. Therefore, the proposed reconstruction approach suggests the detection of such cases, and enforcing perpendicularity or parallelism to the line segments whose orientations make a difference of 0 or 90 degrees within a tolerance. This will correct most of the small orientation errors. For this purpose, the line segments are first clustered based on their orientation, similar to the algorithm mentioned in section 5.2.4.2, and with the same estimated number of clusters. An analysis of the angular differences is then performed

on the cluster means (rather than individual line segments). The orientation of the line segments within the same groups are equated to the corresponding group mean, in order to fulfill parallelism. In the next step, cluster means making a difference of 90 degrees within a tolerance are identified, and are similarly corrected in order to make an exact difference of 90 degrees (see equations (5.9)). The tolerance is defined by the maximum standard deviation within the groups, or the angular resolution of the model. The cluster members are then updated by the same correction applied to their corresponding mean. Figure 5.13 depicts the results of this process for the same example.

$$\Delta\alpha = -\frac{(\alpha_2 - \alpha_1)}{2} \quad (\text{parallel case})$$

$$\Delta\alpha = \frac{90 - (\alpha_2 - \alpha_1)}{2} \quad (\text{perpendicular case})$$

$$\alpha_{2(\text{corrected})} = \alpha_2 + \Delta\alpha$$

$$\alpha_{1(\text{corrected})} = \alpha_1 - \Delta\alpha \tag{5.9}$$

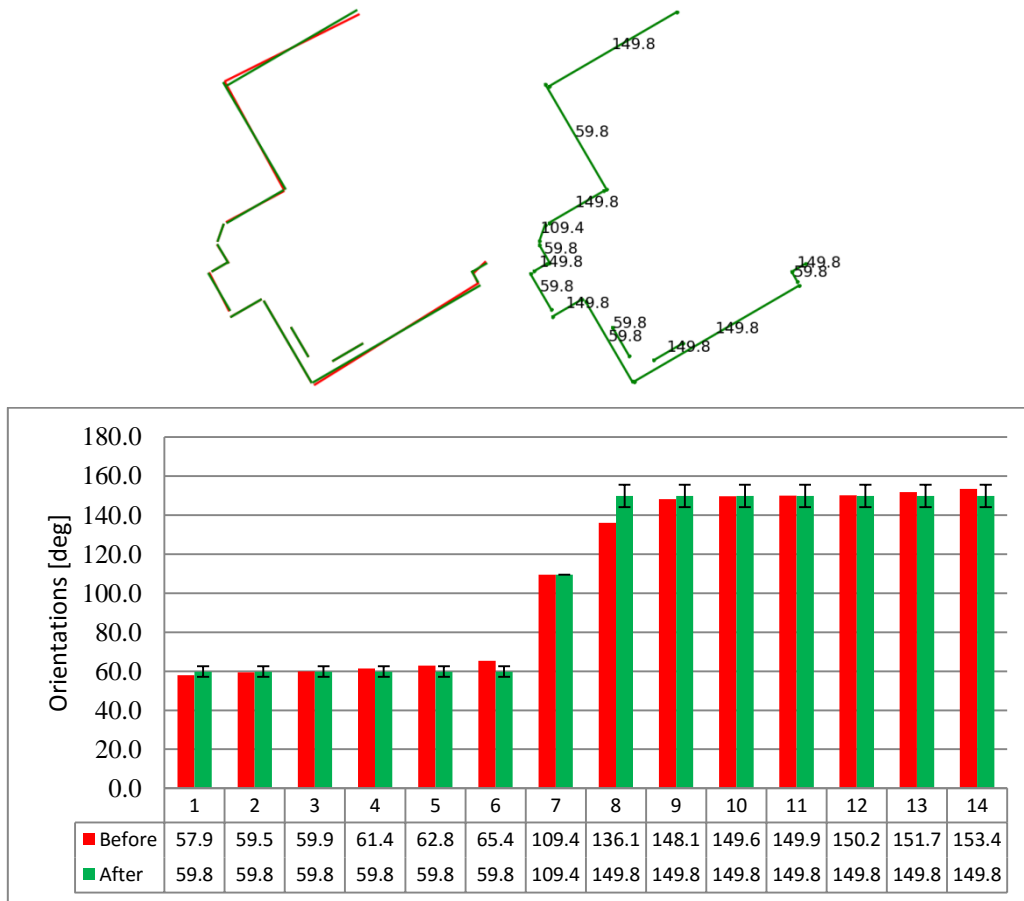


Figure 5.13 – Top: overlaying the model states before (red) and after (green) the angular refinement (left); results after the angular refinement (right). Bottom: orientations before (red) and after (green) the angular refinement, annotated by the standard deviations corresponding to each of the 3 clusters.

5.2.5.2. Extension and Trimming

In this step, the intersections of line segments are analyzed. As depicted in figure 5.13, line segments do not meet each other at the intersection points (walls junctures). This issue can be resolved by the extension or trimming of the line segments within a given threshold. Similar to the last clustering step in section 5.2.4.2, the threshold can be set to the maximum expected size of occlusions in the data (except for the large occlusions caused by doors or windows). Figure 5.14 depicts the possible errors, which may occur in the intersection of two line segments.

The extension and trimming is performed firstly in the original direction for all the line segments, in order to find valid intersections (figure 5.14 a-c). In the next step, possible existing free end points are detected, and line segments are additionally extended in the perpendicular direction at these points, in order to be connected to available structure elements (figure 5.14 d). The latter step can be more general in order to include the case depicted in figure 5.14 (e), if the perpendicular extension or trimming is performed continuously, while the line segment is being extended gradually along its original direction, until the first intersection is found. The proposed algorithm results in a model whose components are connected, and at the same time, the connections fulfill a correct topology. It should be mentioned that for the simplification of the analysis (e.g. finding free end points, etc.), and also for further usages mentioned in chapter 7, the model is converted to a graph whose edges and nodes are the line segments and the corresponding end points. Figure 5.15 depicts the result of the presented algorithm applied to the output of the previous example. In this example, the maximum expected size of occlusions (threshold for extension and trimming) is assumed to be 0.5m. More experimental results are presented in the next chapter.

As it can be seen in figure 5.15, the extension process in the original direction may generate additional invalid line segments (the extension in the perpendicular direction may not cause this problem, as it connects the free end points to the available structure elements). Invalid line segments are detected by analyzing the overlap of the line extensions with the range data. In more detail, a line segment is marked as invalid if it is made by an extension in the original direction, and at the same time, has an insufficient (e.g. less than 50%) overlap with the point cloud resulting from the pre-processing step. It should be mentioned that for a valid overlap analysis, the angular refinement applied in the previous step has to be taken into account, which means, inverse corrections regarding the equations (5.9) has to be applied temporarily for this analysis step (see figure 5.16). Based on this approach, invalid line segments are detected and removed in the presented example, as depicted in figure 5.17. This results in the final 2D model fulfilling a topologically correct geometry.

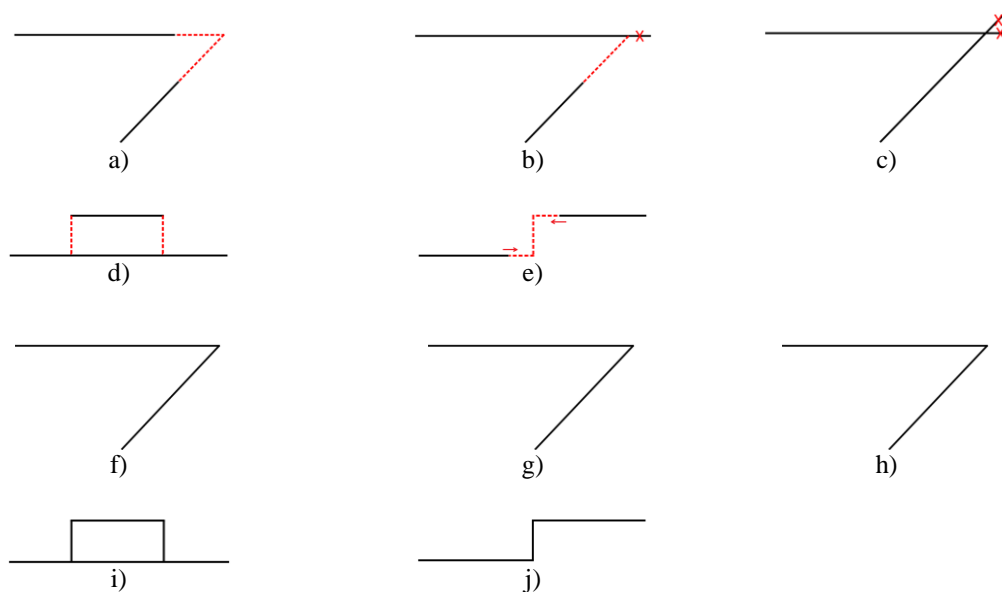


Figure 5.14 – Finding the correct intersections and connections. (a-e): input line segments (black solid lines); (f-j): corresponding topological corrected outputs.

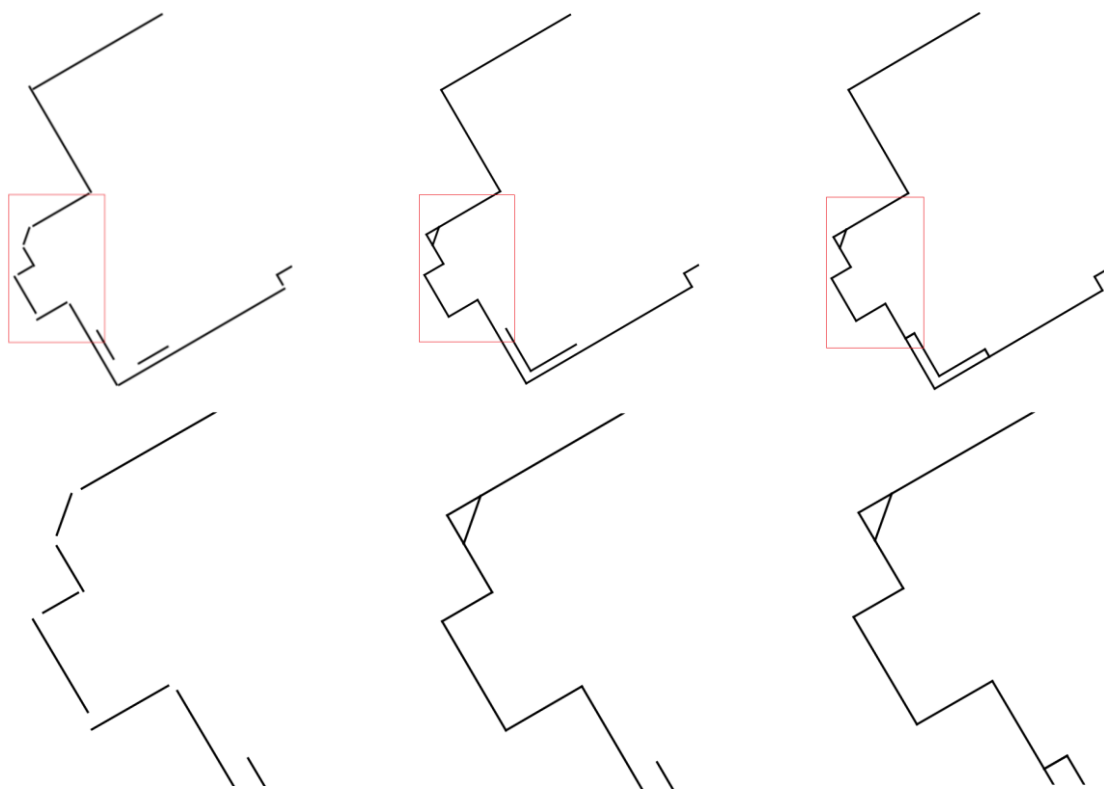


Figure 5.15 – Left to right: before extension and trimming, extension and trimming in the original direction, and extension of free end points in the perpendicular direction.

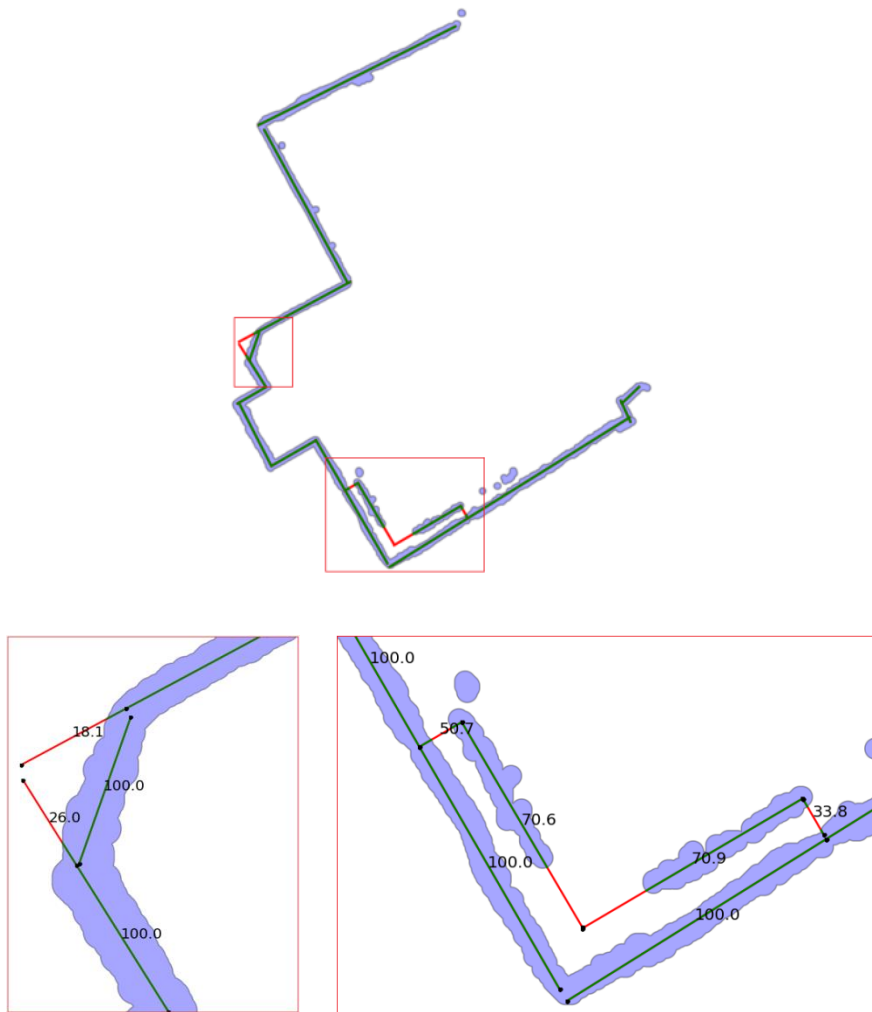


Figure 5.16 – Analyzing the overlap of the line segments with the range data (the overlap percentage is annotated for the zoomed-in parts).

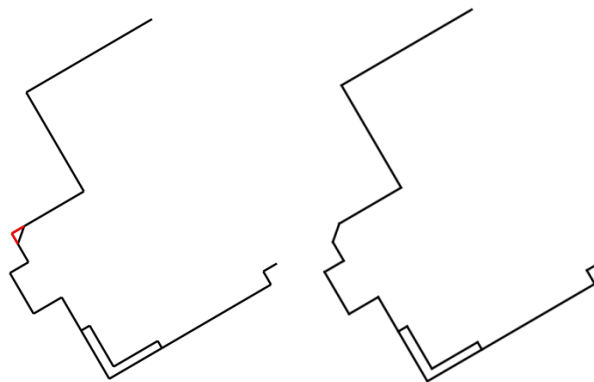


Figure 5.17 – Left: line segments are marked as invalid (red), if they are made by an extension in the original direction, and at the same time, have less than 50% overlap with the range data; Right: the topologically correct 2D model is generated after removing the invalid line segments.

5.2.6. 2D to 3D Conversion of Reconstructed Models

In the last step the reconstructed 2D model is converted to 3D by extruding the line segments in the vertical direction, using the height of the room computed in section 0. Figure 5.18 depicts the 3D model generated from the 2D model of the previous example, by an extrusion of 2.65m.

Evaluation of the reconstruction approach in different scenarios, accuracy analysis of the reconstructed models, reconstruction of gaps caused by large occlusions such as doors and windows, and finally fusion of the reconstructed 3D models with available coarse indoor models are presented in the next chapters.

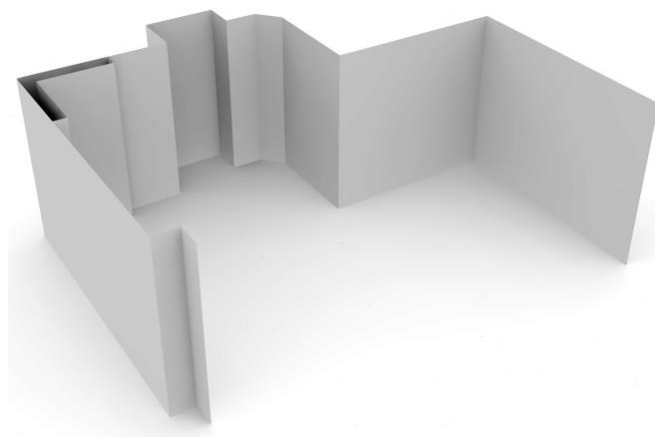


Figure 5.18 – Final 3D model resulting from the extrusion of the corresponding 2D model.

6. Experimental Results and Analysis

This chapter evaluates the performance and accuracy of the developed system for the automatic reconstruction of indoor spaces, explained in the previous chapter. It starts with the system calibration and accuracy analysis of the range measurements by Kinect, and then continues with the performance evaluation of the modeling approach in different scenarios.

6.1. Kinect System Calibration and Accuracy Analysis

6.1.1. System Calibration

As already mentioned in section 3.1.2, for colorizing the point clouds derived by the Kinect range measurement system, as well as making use of the information provided by the RGB camera for the alignment of the point clouds, it is necessary to perform a pixel-to-pixel registration of the RGB and depth values. The registration is possible having the system calibration parameters available.

The system calibration is composed of the optical calibration of the IR and RGB cameras together with the estimation of their relative orientation, using a bundle block adjustment. In order to ensure the maximum accuracy, a planar test-field with no control point was captured from eight positions by the IR and RGB cameras synchronously, using a similar configuration recommended by Wester-Ebbinghaus (1981) and Luhmann et al. (2014). In this configuration, corresponding images are taken perpendicularly and obliquely with a relative orientation of 90° around the optical axis, as depicted in figure 6.1. Measured image coordinates together with approximate object coordinates are processed within a bundle adjustment in order to estimate the interior and exterior orientation parameters for both cameras. In the test-field calibration, it is suggested to define the datum using an unconstrained technique, e.g. using a free net bundle adjustment, in order to prevent the effect of possible inconsistencies in the datum information on the estimated unknown parameters.

The target points in the test-field are usually circular, in order to provide a radial symmetry. Circular targets are very suitable for the manual and automatic measurements and are invariant to rotation and scale. Luhmann et al. (2014) suggest a minimum diameter of the targets to be at least 5 pixels in the taken images. Moreover, considering the fact that the distortion parameters are dependent on the object distance (Dold, 1997), the distance to the test-field shall be chosen as similar as possible to the object distances in real applications. Therefore, the actual size of the targets can be computed having the scale of the images and the pixel size. In this study, the approximate object distance in the practical measurements is about 3m, which results in 5mm Ground Sampling Distance (GSD). Therefore, the target diameter shall be at least 25mm. Centers of the targets are automatically detected based on pattern matching techniques used by the Australis software (Photometrix) which is employed here for the performance of the calibration task.

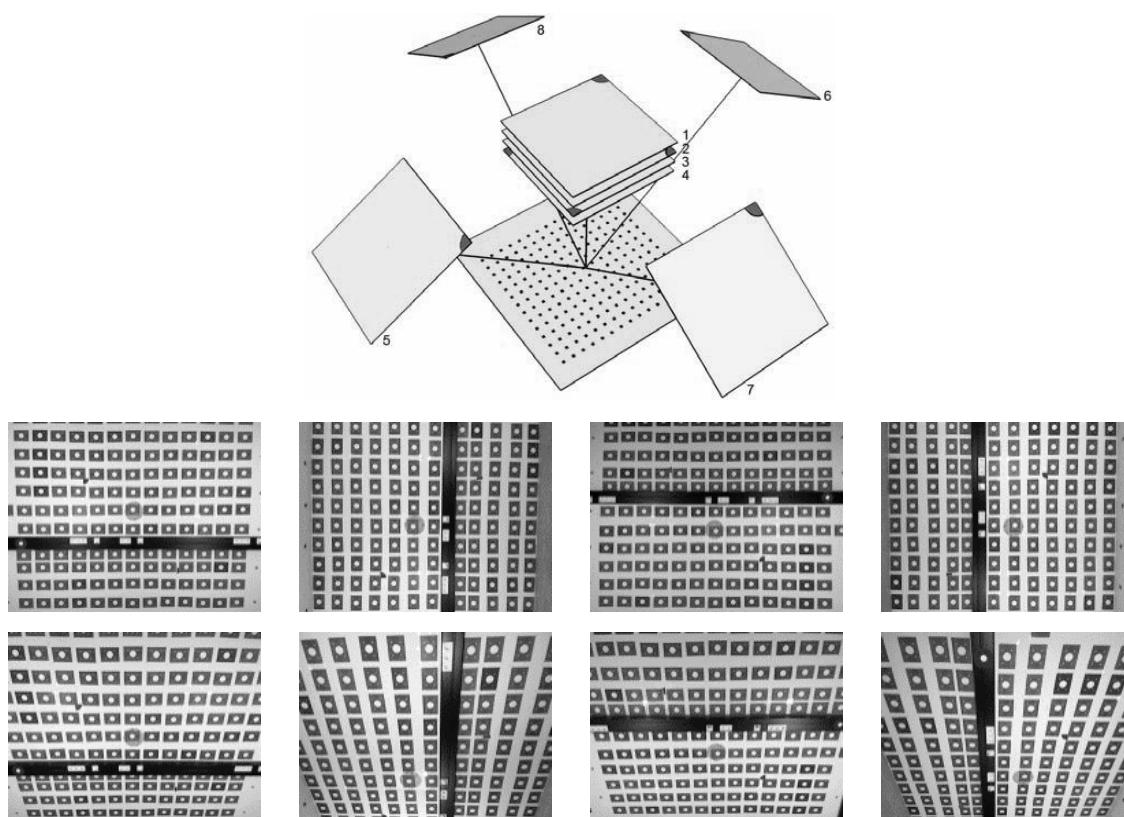


Figure 6.1 – The calibration test-field and the image configuration used for the system calibration (only images corresponding to the IR camera are depicted in this figure).

Calibration Results and Evaluations

Using the mentioned image configurations and the test-field setup, the parameters of the interior and exterior orientations are estimated based on the mathematical model mentioned in section 3.1.2. The interior orientation parameters as well as the lens distortion curves are presented in table 6.1 and figure 6.2, assuming the pixel size of $1\mu\text{m}$ for both IR and RGB cameras. The selected pixel size has no effect on the calculations, as far as the focal length and other camera intrinsic parameters are also expressed in pixels.

The RMS of image coordinates residuals after the adjustment for the IR camera is around 0.13 pixels, and for the RGB camera around 0.08 pixels (without Brown's additional parameters, the RMS for both cameras is around 0.4 pixels after the adjustment). The estimated RMS values for both cameras show that the Brown's model has been able to sufficiently model the lens distortion parameters. The term "sufficiently" is deduced regarding the fact that in practical applications, image space observations will not be of higher accuracy than the estimated RMS values, due to the following reasons:

- a) The light condition in practice is not necessarily as ideal as the condition in which the camera is calibrated, and therefore measurements are subject to motion blur and more noise.
- b) The calibration task uses tie points which are signaled by well-defined circular targets, and are detected using pattern recognition techniques. In practice, interest points are extracted and matched typically based on the SIFT or other feature detectors, which expected to deliver an accuracy of about 0.7 pixels, according to the investigations made by (Mikolajczyk and Schmid, 2004).
- c) It should be also considered that the noise of the Kinect range measurements is in the order of centimeters, which is more than the Kinect cameras GSD (5mm at 3m distance).

Therefore regarding the mentioned reason, in applications using Kinect, an accuracy of around 0.5 pixels for image space observations is already sufficient. For this reason, there is no need to use more accurate and advanced calibration models, e.g. those introduced by Tang et al. (2012), as mentioned in section 3.1.2.

The relative orientation of the IR and RGB sensors is computed using the exterior orientation of the cameras estimated in the adjustment, by averaging the transformation matrices estimated at each camera position (i.e. averaging the $\mathbf{H}_{\text{IR} \rightarrow \text{RGB}}$ matrix in equation (3.14)). The resulting relative orientation parameters are presented in table 6.2.

It should be mentioned that the actual size of the IR sensor is 1280×1024 pixels, but due to the bandwidth limitation of the USB connection, the output of the IR camera as well as the disparity image are cropped to 640×480 pixels. Moreover, the disparity image has a shift of 4 pixels with respect to the IR image in the x direction, due to the application of a correlation window (9×9 pixels) in the calculation of disparity values (Khoshelham and Elberink, 2012). This value has to be considered in calculations in which RGB values have to be assigned to depth values.

Parameter		IR Camera		RGB Camera	
		Adjusted value	Std. Dev.	Adjusted value	Std. Dev.
Focal length	c	585.7 [pix]	6.6e-001 [pix]	521.9 [pix]	6.0e-001 [pix]
Principal point offset	x_p	0.6 [pix]	1.2e-001 [pix]	-0.3 [pix]	1.1e-001 [pix]
	y_p	-9.1 [pix]	3.5e-001 [pix]	-16.5 [pix]	3.2e-001 [pix]
Radial lens distortion parameters	K_1	3.75303e-001	6.7e-003	-6.63541e-001	7.401e-003
	K_2	-3.94502e+000	8.612e-002	6.59073e+000	1.082e-001
	K_3	1.37589e+001	3.608e-001	-2.02217e+001	5.147e-001
Decentering lens distortion parameters	P_1	2.60056e-004	1.084e-004	5.79941e-004	1.191e-004
	P_2	2.51454e-003	1.041e-004	-1.13229e-003	1.141e-004
Image coordinates residuals (RMS)		0.13 [pix]	N. A.	0.08 [pix]	N. A.

Table 6.1 – Adjusted parameters of the IR and RGB cameras, assuming a pixel size of 1 μ m for both sensors. Radial and decentering distortion parameters are computed assuming the measurement unit is millimeters.

Parameter	Value	Std. Dev.
ΔX [mm]	23.9	1.4
ΔY [mm]	1.2	1.4
ΔZ [mm]	0.7	2.3
Δ Heading [deg]	-0.2	1.4
Δ Elevation [deg]	-0.1	1.5
Δ Roll [deg]	0.1	0.6

Table 6.2 – Relative orientation of the RGB camera with respect to the IR local camera coordinate system. Only ΔX is significant.

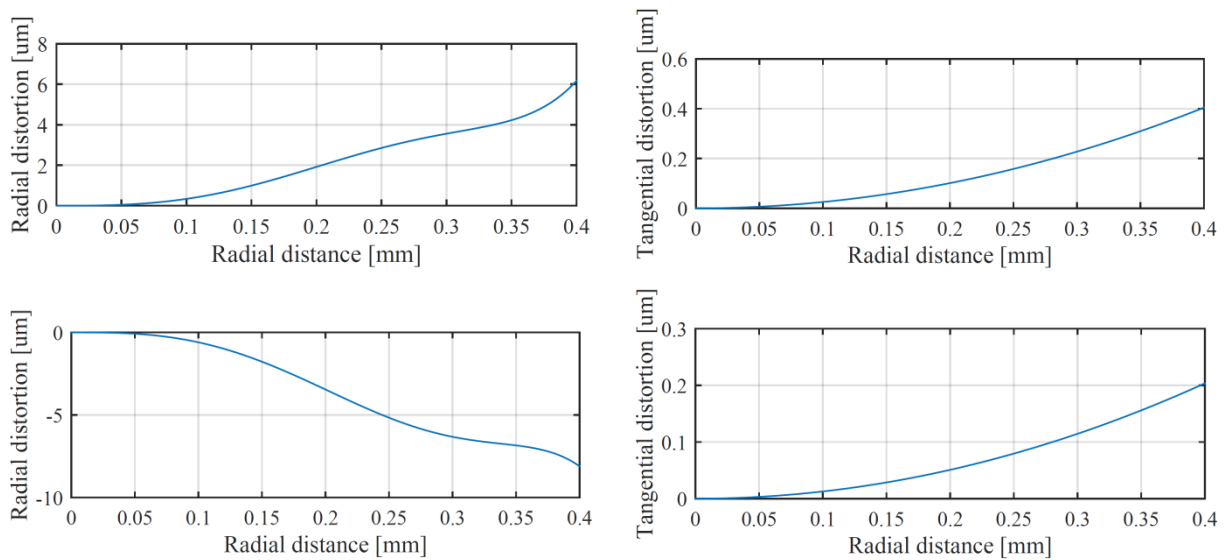


Figure 6.2 – Radial and tangential distortion curves for the IR (top) and RGB (bottom) cameras, assuming a pixel size of $1\mu\text{m}$ for both sensors.

6.1.2. Accuracy of Kinect Range Measurements

As already mentioned, Kinect range data is computed from disparity measurements. The IR laser beamer projects a semi-random (but known) speckle pattern on the object surface. The reflection of the pattern is then recorded by the IR camera in 30 frames per second. The disparity measurements are realized by the cross-correlation of the reference and collected patterns. In practice, the accuracy of the measurements is affected by factors such as:

Existence of other sources of light: Any interference in the infrared component (e.g. existence of sun light) can significantly disturb the pattern matching, and therefore reduces the quality of range measurements (figure 6.3).

Object properties: Smooth surfaces such as mirrors result in the specular diffusion of the incident light, and therefore no speckle pattern can be observed by the IR camera. Moreover, black objects can partly to entirely absorb the incident laser pattern.

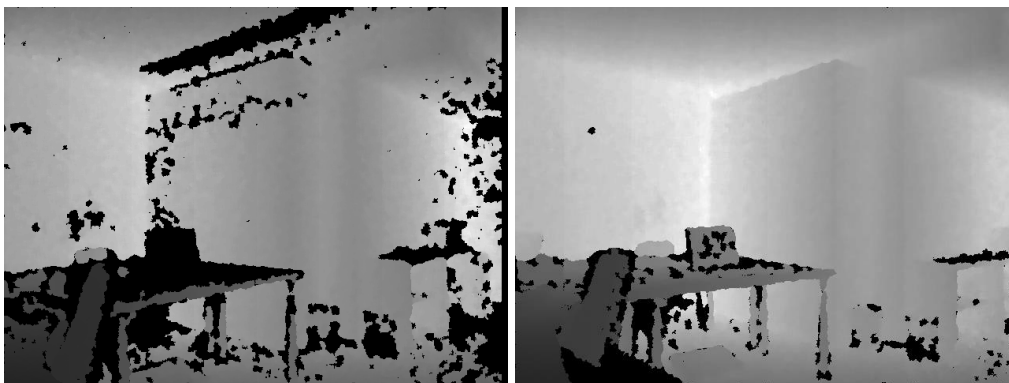


Figure 6.3 – Range measurement with (left) and without (right) the existence of the sun light.

Object distance: Increasing the object distance increases the GSD of the IR camera pixels; this consequently reduces the sensitivity of the detection of surface variations.

Moreover, since Kinect is a triangulation system with parallel axes and a fix baseline (the distance between IR camera and laser projector is approximately 7.5cm), the precision of the range measurements is decreased by increasing the object distance. In this case, as also mentioned by Menna et al. (2011), the theoretical precision (as a measure of uncertainty) of the 3D coordinates of an object point located on the xy plane (normal to the optical axis of the sensors at the distance H) is related to the object distance by the following relationships (see figure 3.3):

$$\sigma_{XY} = \mu \frac{H}{c} \quad (6.1)$$

$$H = \frac{b \cdot c}{d} \Rightarrow \sigma_H = \frac{H^2}{b \cdot c} \cdot \sigma_d \quad (6.2)$$

where μ is the pixel size of the IR camera, c is the focal length of the IR camera, b is the baseline between the IR camera and the laser projector and σ_d is the precision of the measured parallax (disparity). Equation (6.2) shows a quadratic relationship between object distance and the range measurements precision (internal accuracy). Similar to Khoshelham and Elberink (2012), this effect is verified by a plane fitting test for the data captured from a planar object located at different distances, perpendicular to the optical axis of the sensor (see figure 6.4). In this test, the RMS of fitting errors is considered as a measure for the precision of the range data at the measured distance, as the points have approximately the same perpendicular distance to the sensor. However for this test, points are selected from an area in the middle part of range images. The reason for this selection is the existence of a radial error pattern in the range images, whose intensity is increased towards the image corners. The intensity of this error pattern also depends on the object distance, which may imply the unmodeled radial lens distortion of the IR camera as well as the IR laser projector in the image matching algorithm. The reason for this assumption is that the radial lens distortion causes shifts within the image plane that affects the computation of disparity values and therefore the range measurement accuracies as a function of the squared object distance. The effect is visualized in figure 6.5 that depicts the noise of range images acquired from a planar object (filling the whole image frame) at three different distances. The figure further depicts the existence of a vertical stripe pattern. The number of vertical stripes varies at different distances, which seems to be related to the image matching algorithm used by Kinect (more details cannot be provided, since the algorithm used by PrimeSense technology is not disclosed).

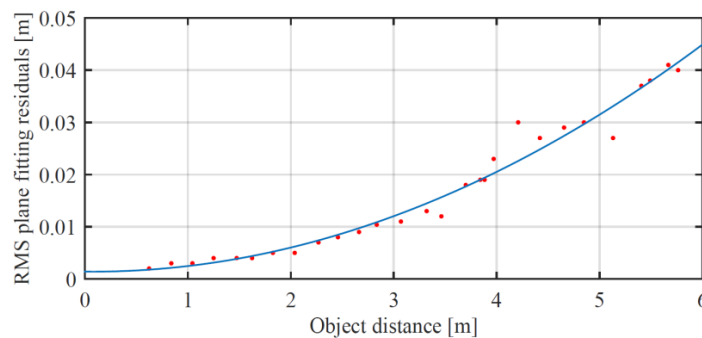


Figure 6.4 – RMS of plane fitting residuals at the central part of the range image at different distances with a second order polynomial fit.

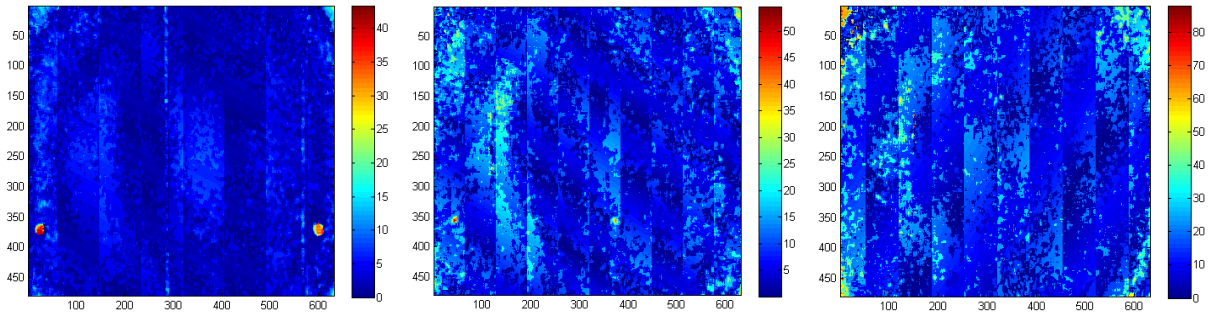


Figure 6.5 – Left to right: noise of the range data throughout the whole image format, at 1m (RMS: 3mm), 1.8m (RMS: 7mm) and 2.6m (RMS: 15mm) distance, respectively.

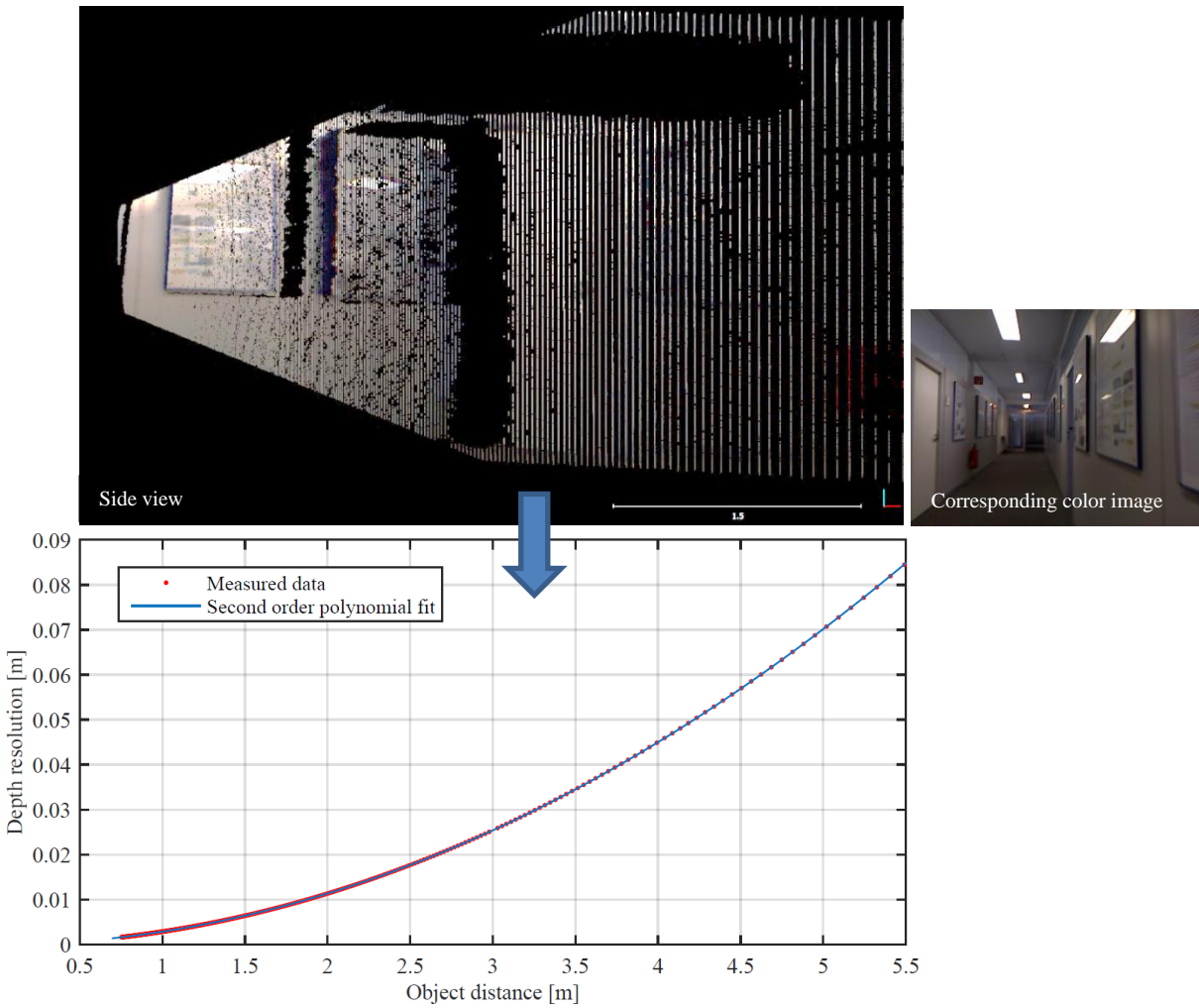


Figure 6.6 – Depth resolution of Kinect at different object distances with a second order polynomial fit.

Equation (6.2) can also explain the depth quantization effect observed in Kinect range measurements. As mentioned before, according to Khoshelham and Elberink (2012), Kinect disparity measurements are stored as 11 bit integers, where 1 bit is reserved for marking the pixels for which no measurement is available. Therefore, disparity values are quantified based on 1024 levels. The depth resolution is then defined as the difference between the depth values corresponding to two consecutive disparity levels, which is proportional to the squared object distance H (σ_d , b and c are constant). This effect is visualized for the sample point cloud depicted in figure 6.6. The figure shows that at the distance of 5.5m, one can expect a depth resolution (quantization) of more than 8cm.

6.2. Evaluation of the Reconstruction Approach

In chapter 5, an approach for the automatic reconstruction of indoor spaces was introduced, and different steps were presented using an exemplary case study. This section aims at the evaluation of the reconstruction approach by the assessment of the robustness and efficiency of the approach in different scenarios. The robustness and efficiency can be described by the stability of the selected parameters in different noise levels and different room shapes. It further continues with the accuracy analysis of the reconstructed models, based on a comparison between resulting 3D models and the point clouds collected by a highly accurate TLS.

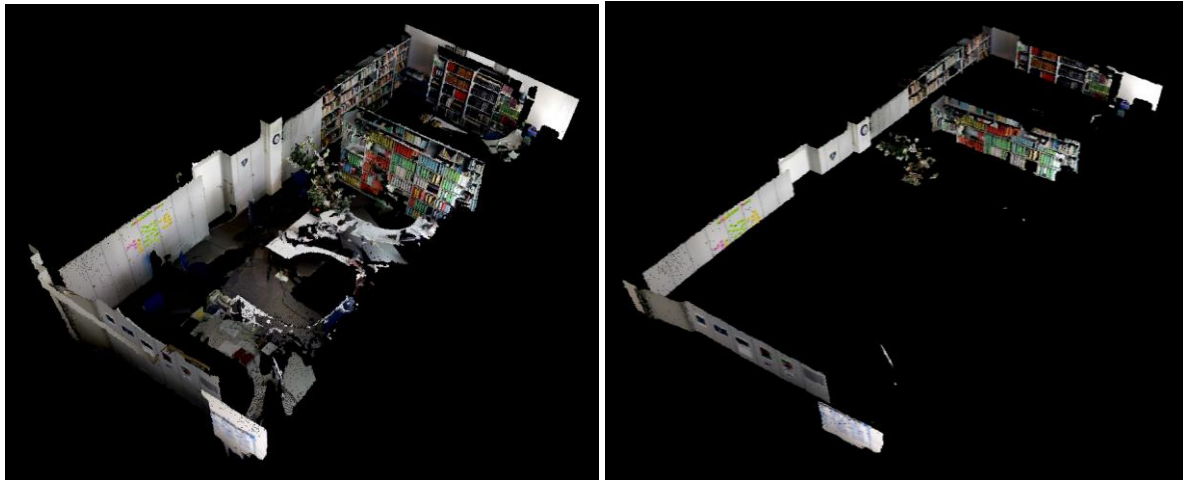
6.2.1. Parameter Selection in Different Scenarios

The proposed reconstruction approach consists of several parameters and thresholds which have to be set in different processing steps, from the point cloud pre-processing to final topological corrections. Criteria for parameter selection were suggested during the presentation of the modeling process in the previous chapter, which are summarized in table 6.3. The criteria mainly provide correct values for the parameters; however, for some processing steps supervision (the user verification) might be required, such as the furniture removal (section 0) and the binarization of the orthographic projected images (section 5.2.2).

In the furniture removal process, although a selective height filter (see table 6.3) typically delivers satisfactory results, the effect of remaining clutter cannot be compensated by the modeling process, if a detailed modeling of indoor spaces is demanded. The remaining clutter can be removed manually, however, it can be very time consuming and tedious in case of dealing with a large number of rooms. Alternatively, one can remove the effect of the remaining clutter by setting a suitable threshold in the binarization process. In this study, according to equation (5.5), the binarization threshold is defined based on the ratio between the maximum possible height of remaining clutter and the height range of the selective height filter. Figure 6.7 depicts an example, in which the effect of remaining clutter is removed by changing the binarization threshold as a function of $\alpha = H_{\text{noise}} / H_{\text{filter}}$. Selection of a correct value for α is verified by the user; the parameter is increased until no more clutter is observed by the user. Moreover, as the core of the modeling process, the Hough transform parameters should be noticed and selected correctly. The parameters are expressed as the minimum allowed number of votes (β_1), the minimum allowed length of the line (β_2) and the maximum allowed gap (β_3). In this example, the parameters are set to the same values used by the pilot study in the previous chapter.

Processing step	Parameter/Threshold	Selection criterion
Outlier removal	Mean distance to K-nearest neighbors	Standard deviation of distances (1σ or 2σ normality test)
Downsampling	Voxel size	Noise of the point cloud (e.g. 3-5cm in case of using Kinect) or flatness tolerance based on DIN 18202
Noise removal	Search radius and the degree of the local fitting polynomial	Noise of the point cloud (for Kinect, a local plane fitting with a radius search of 10-15cm delivered the optimum results in all of the examples)
Leveling the point cloud	Clustering threshold for finding horizontal or vertical surface points	$\pm 45^\circ$ tolerance, which is almost always fulfilled
Furniture removal	Height range of the selective height filter	Typically a range of [1.5m, 2.5m] gives the optimum results. Supervision is recommended due to the possible existence of large clutter such as plants, etc.
Generation of the orthographic projected image	Grid size	Noise of the point cloud (e.g. 3-5cm in case of using Kinect)
Binarization	Grayscale intensity threshold	Based on the ratio between the maximum possible height of remaining clutter and the height range of the selective height filter (case dependent, supervision is recommended)
Polygon closing	Dilation and erosion kernel size	Experience shows that a 3×3 kernel size delivers optimum results. Larger kernel size may wrongly attach the adjacent structures.
Line extraction using the Hough transform	Minimum votes, minimum length of the line and maximum gap	Noise of the computed structure skeletons (expected deviation from straight lines), grid (pixel) size of the orthographic projected image and the modeling accuracy
Clustering and averaging the line segments	Maximum allowed gap in the connectivity clustering	Case dependent. In the presented examples, observed occlusions and gaps are mostly up to 0.5-1m.
Parallelism and perpendicularity	Maximum allowed misalignment in the line orientations	Maximum standard deviation within the orientation clusters, or the required angular resolution in modeling
Line extension and trimming	Extension and trimming threshold	Maximum allowed gap (see above)
Removing invalid generated line segments	Minimum allowed overlap between the candidate lines and the point cloud	Noise of the point cloud and the modeling accuracy; an overlap threshold of 50% (a preservative choice) was qualified in all of the presented examples

Table 6.3 – Parameters and their selection criterion in different modeling steps.



Furniture removal by means of a selective height filter: $1.5\text{m} < h < 2.5\text{m}$ (data collected by a DPI-7 sensor system). Ceiling points are removed for visibility purposes.

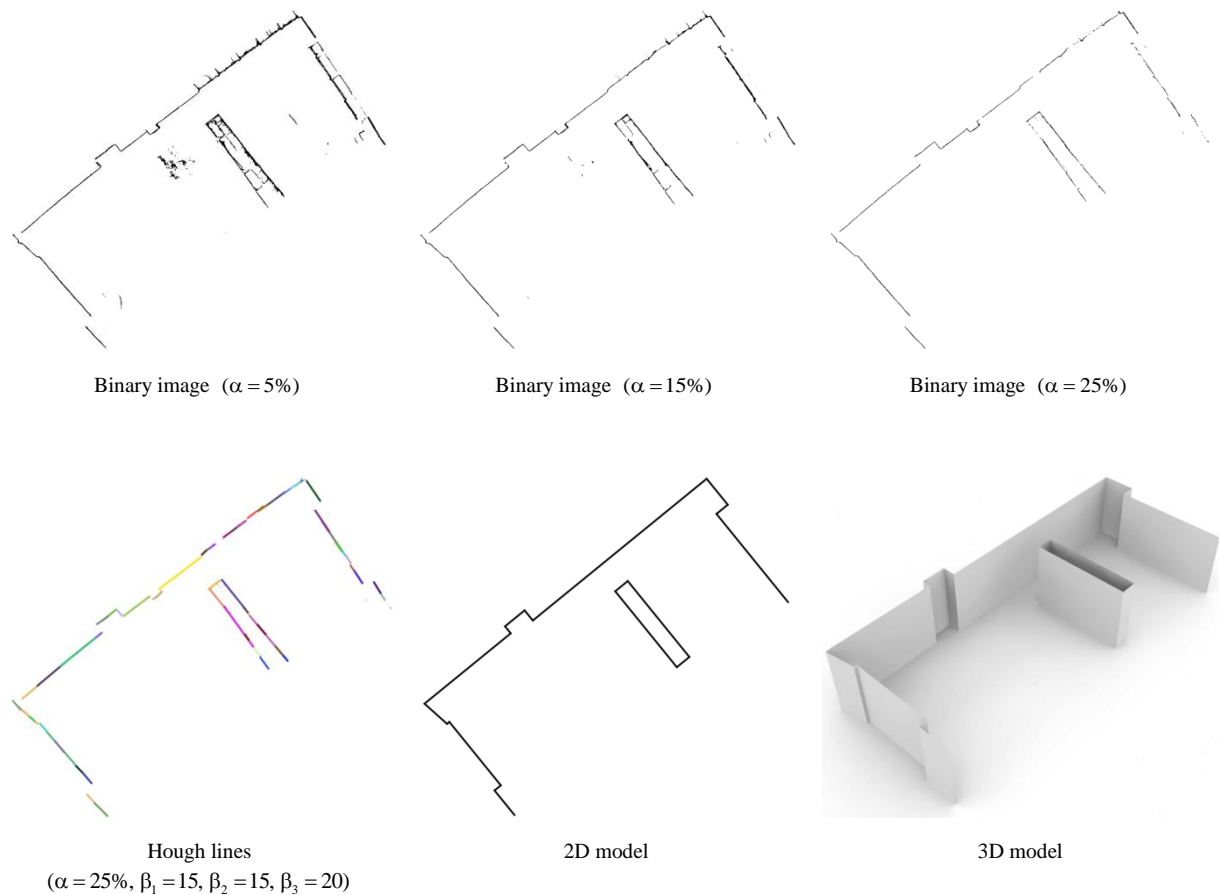


Figure 6.7 – Top: furniture removal by means of a selective height filter. Middle: removing the effect of remaining clutter by adjusting the binarization threshold. Bottom: line extraction and modeling provides satisfactory results only for $25\% < \alpha < 30\%$.

The quality (signal to noise ratio) of the binary orthographic projected image has a direct effect on the line extraction process using the Hough transform. In other words, the Hough transform parameters may vary from one example to another, depending on the quality of the skeletonized image derived from the binary image. In figure 6.8 (b), line extraction and modeling results are compared for different binarization thresholds and different Hough transform parameter sets for an exemplary point

cloud depicted in figure 6.8 (a). This will gain a clearer perception regarding the stability of the Hough transform parameters in different scenarios. In this example, furniture and clutter are completely removed using a selective height filter. Therefore, the binarization threshold does not play an important role here. As it can be seen in this example, the reconstruction results are valid for all the 3 choices of the Hough transform parameter sets. However, a simultaneous increase in α and the Hough transform parameters makes the line extraction more sensitive, i.e. a smaller amount of lines are extracted from the skeleton. In this case, the extension-trimming threshold shall be increased in order to compensate the effect of missing line segments.

The efficiency and robustness of the proposed reconstruction approach is further assessed for different types of sensors and room shapes, as depicted in appendix E figures. The point clouds in the presented examples are collected by 4 different sensors based on different measurement principles and therefore different range measurement accuracies: Kinect (active triangulation system), Kinect V2 (TOF camera), DPI-7 (active triangulation system) and Leica HDS3000 (TLS). In these examples, some user interactions (or verifications) were necessary in the furniture removal process, mostly for the verification of the range of the selective height filter and setting the binarization threshold α . However, Hough transform parameters were fixed in all of the presented examples, which shows the stability of the line estimation algorithm and parameters in different cases. The reason is that the input orthographic projected images have a similar quality, thanks to the pre-processing step. It should be mentioned that due to the existence of relatively larger occlusions in the point cloud of examples depicted in figures E.1 and E.2, the extension-trim threshold had to be increased in such examples, in order to reconstruct the gaps. The remaining parameters were selected based on the criterions suggested in table 6.3, and stayed untouched in different examples.

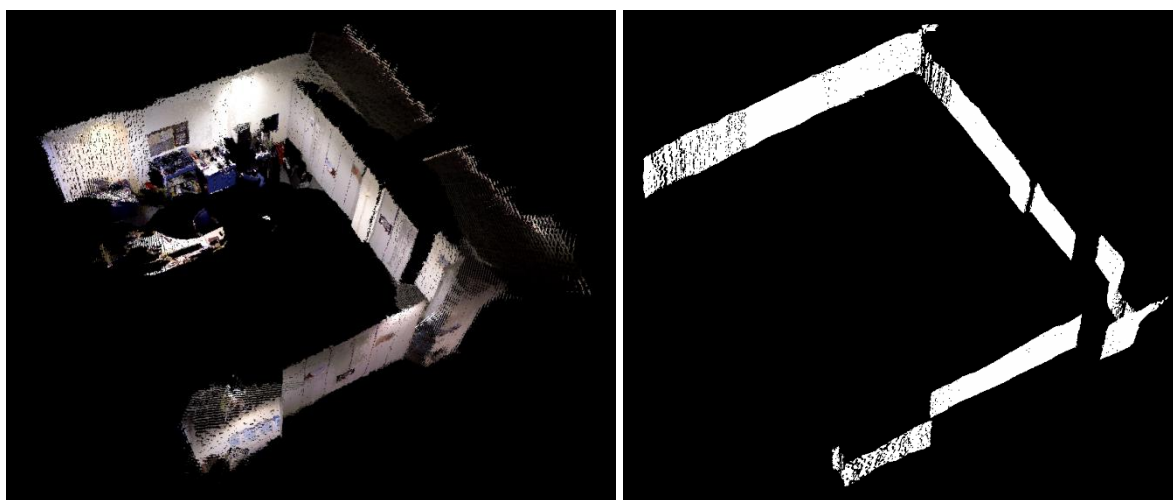


Figure 6.8 (a) – Furniture and clutter removal using a selected height filter ($1.5\text{m} < h < 2.5\text{m}$) for a sample room point cloud captured by Kinect.

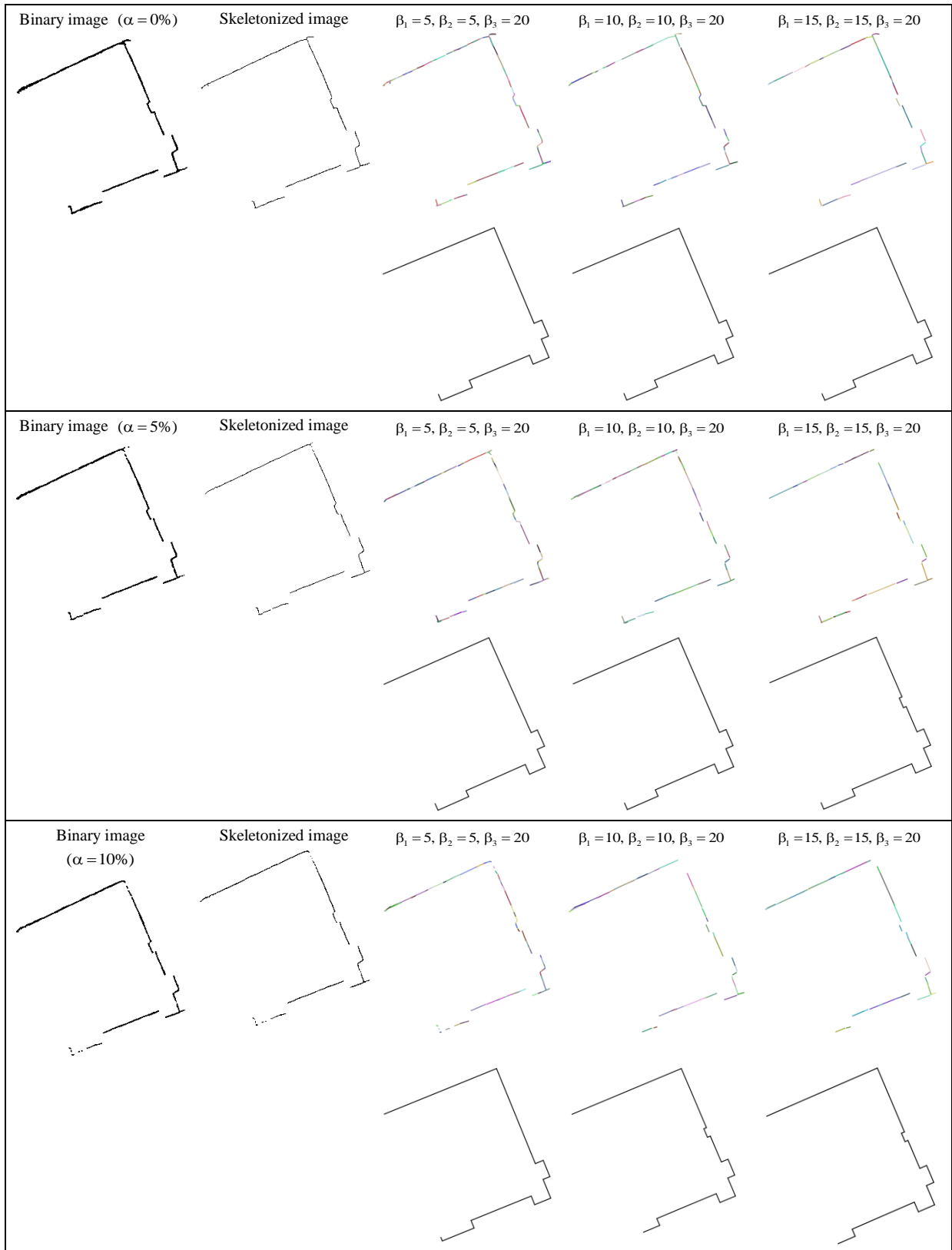


Figure 6.8 (b) – Line extraction and modeling results for different qualities of the binary image and different Hough transform parameters for the example depicted in figure 6.8 (a).

6.3. Quality of the Reconstructed Models

After presenting the modeling approach and its performance evaluation, the accuracy of the reconstructed models is investigated by comparing them with reference data. The comparison represents errors in the range measurement and alignment, as well as the error committed in representing interior structures by means of planar surfaces using the described modeling strategy. The reference data is obtained by means of a high-accuracy laser scanner (Leica HDS3000), with 1cm sampling distance, 4mm single point range measurement accuracy (1-50m distance, one sigma) and 2mm surface modeling accuracy (one sigma) (“Leica HDS3000 Product Specifications,” 2015). This accuracy is one order of magnitude better than the noise of the registered point cloud obtained by low-cost range cameras; therefore, the TLS data can be assumed accurate enough to serve as reference in this comparison.

The results of comparison for an exemplary 3D model reconstructed from Kinect point clouds are depicted in figure 6.9. In this example, the accuracy measure is the distance between the TLS point cloud and the 3D model. Since the TLS point cloud is registered in a different local coordinate system, the point cloud is registered to the 3D model using the ICP algorithm. The comparison shows an overall mean difference of 0.030m with a standard deviation of 0.027m and a maximum of 0.137m. However, as depicted in figure 6.9 (c), for different walls, different accuracies can be estimated (see table 6.4). This effect can also be observed in figure 6.9 (d), in which 3 Gaussian fits can be distinguished visually. Since the Kinect point cloud has a noise level of approximately 3cm at 3m distance, the remaining error is assigned to the point cloud registration process. However, it should be noted that the averaging concept, which is the basis of the modeling process, together with suggested topological corrections to some extent have reduced the effect of range measurement and registration errors on the final results.

In order to distinguish the data collection and modeling errors, a similar comparison is made between the 3D model of the same room, reconstructed from the TLS point cloud, and the point cloud itself. Figure 6.10 depicts the results of this comparison. The comparison shows an overall mean difference of 0.007m with a standard deviation of 0.006m and a maximum of 0.040m. In this case, the modeling accuracy is estimated from:

$$\begin{aligned}
 \sigma_o^2 &= \sigma_D^2 + \sigma_M^2 \\
 \Rightarrow \sigma_M^2 &= \sigma_o^2 - \sigma_D^2 = (7\text{mm})^2 - (2\text{mm})^2 \\
 \Rightarrow \sigma_M &\approx 6.7\text{mm}
 \end{aligned}
 \tag{6.3}$$

where, σ_o is the overall accuracy, σ_M is the modeling accuracy and σ_D is the accuracy of the data collected by the TLS. It should be noted that the modeling accuracy can be controlled by the parameters presented in table 6.3. The most affective parameter in the modeling process is the voxel size in the downsampling process (for the quantization of the input point cloud), as well as the pixel size of the orthographic projected image. In this example, both of the parameters are set to 1cm, which is consistent with the estimated overall mean difference (7mm).

It is necessary to mention that according to Tang et al. (2010), the modeling accuracy and level-of-detail required for a particular application are still open questions, however, there exist guidelines for the accuracy tolerances suggested e.g. by the U.S. GSA (“U.S. General Services Administration,” 2009). According to this guideline, the accuracy tolerance may range from 3mm to 51mm, and artifact sizes may range from 13mm to 152mm.

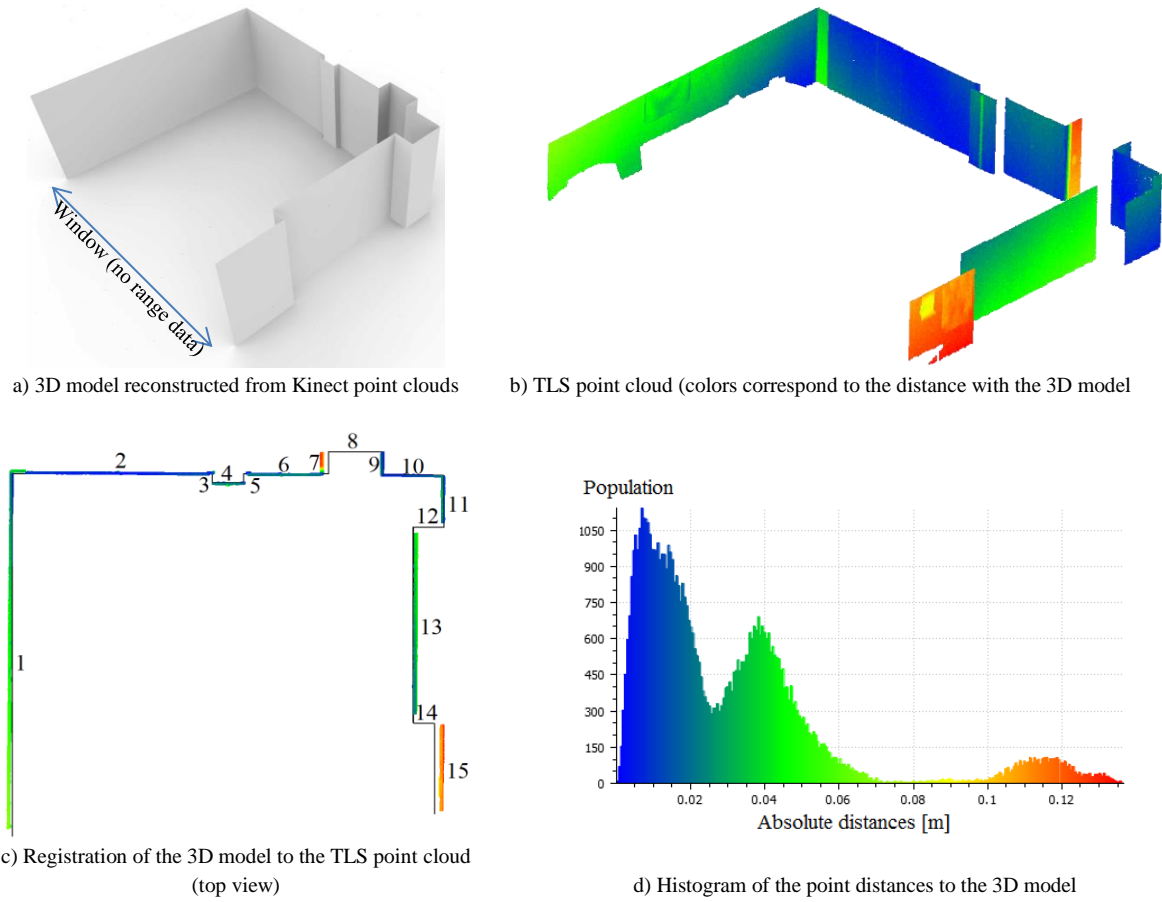


Figure 6.9 – Comparing a 3D model reconstructed from Kinect point clouds with a TLS point cloud.

Wall number	1	2	3	4	5	6	7	8	9	10	11	12	13	14	15
Mean distance [mm]	36	10	-	17	-	16	87	-	11	8	16	-	40	-	118
Standard deviation [mm]	14	7	-	6	-	4	4	-	6	4	5	-	8	-	10

Table 6.4 – Point distances calculated for each wall (corresponding to figure 6.9).

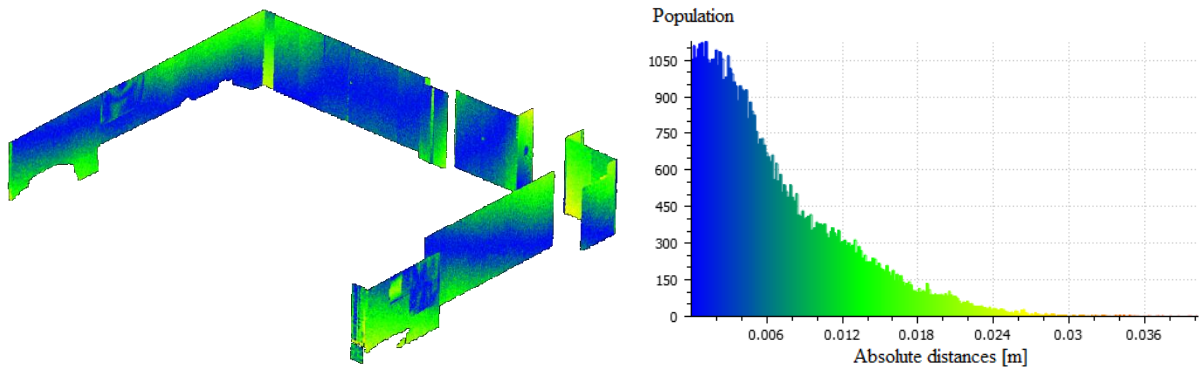


Figure 6.10 – Comparing a 3D model reconstructed from TLS point cloud with the corresponding point cloud.

7. Application in the Refinement of Available Coarse Floor Models

In the previous chapter, the performance of the presented approach for the automatic reconstruction of individual room models was demonstrated. As an application, this chapter demonstrates how the reconstructed room models can be used in the refinement of available coarse floor models. Available floor models may need a refinement or an update due to generalizations in the reconstruction process, or recent changes in the building interiors such as the addition of new elements (e.g. large cupboards, partitions, etc.). The refinement is demanded by many applications, for instance interior design, safety and security planning, indoor navigation, etc. Using low-cost sensor systems such as Kinect for the data collection makes the performance of this task faster and more efficient.

The proposed refinement approach is presented using an example, in which a coarse floor model (figure 7.1) is automatically derived from a photographed evacuation plan using the work of (Peter et al., 2013b) (see section 4.2.3 for more details). The refinement approach firstly registers the detailed model of individual rooms with the coarse model. The models are then merged together, and finally possible gaps within the detailed models are automatically reconstructed using a new learning-based approach employing the information inferred from the coarse model. Similar to the reconstruction strategy mentioned in chapter 5, the algorithms of this process are designed for the 2D case; results are converted to 3D in the very last step using a simple extrusion. The process is presented in the following sections in more detail.

Assumption: While the approach deals with changes inside the room models, it excludes three special scenarios in which a room is split, multiple rooms are merged, or a room is enlarged.

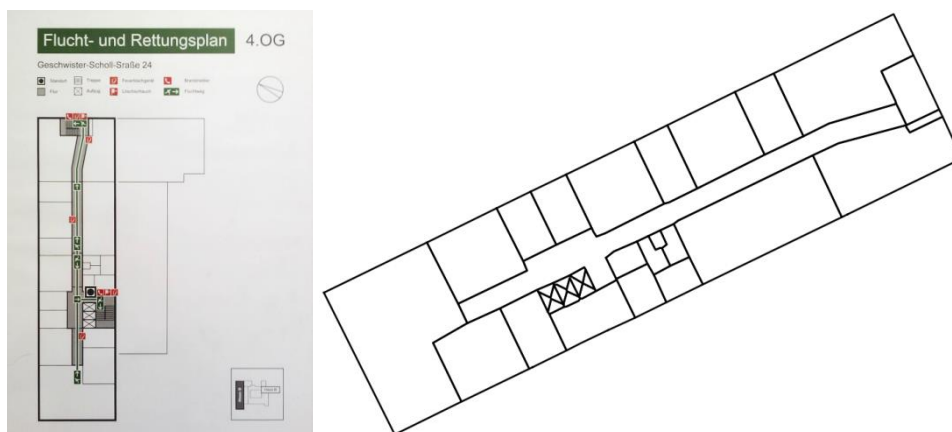


Figure 7.1 – The case study is a coarse floor plan automatically derived from a photographed evacuation plan using the work of (Peter et al., 2013b).

7.1. Registration of Individual Detailed Models to an Available Coarse Floor Model

As already mentioned, in the first step of the update and refinement process, the reconstructed detailed models have to be registered with an available coarse floor model. The registration consists of two steps: approximate and fine registration. In fact, the approximate registration provides initial values required for a fine registration, which is the optimal fitting of the detailed model to the coarse model using a least squares adjustment.

7.1.1. Approximate Registration

For the approximate registration, the initial position and orientation of the detailed model with respect to the coarse model is required. The translation is solved by the coincidence of the centroid of the detailed model with the centroid of the corresponding room in the coarse model. Therefore, it is sufficient to know the information about the room correspondences. This information can be provided by the user in an interactive way, or alternatively, by means of an indoor positioning solution during the data collection process. In the presented case study, the room correspondences are inferred by the user's track derived from the MEMS IMU positioning method, implemented and presented by (Peter et al., 2013b). In this positioning method, the user track is registered to the coarse model based on the initial position of the user and the building principal axes. The user initial position is assumed to be the location of the evacuation plan, where the user photographs it. Therefore, the user employs a foot mounted MEMS IMU and walks from the position of the evacuation plan into the room whose point cloud has to be collected. The corresponding room is the one that contains the last track point. Assuming the user starts capturing the point clouds while the sensor is oriented toward the door location, the initial orientation of the detailed model with respect to the coarse model is approximately known. According to Peter et al. (2013b), the door locations in the coarse model can be identified by the intersection of the user's track with this model. Figure 7.2 depicts the results of this registration for an exemplary room.

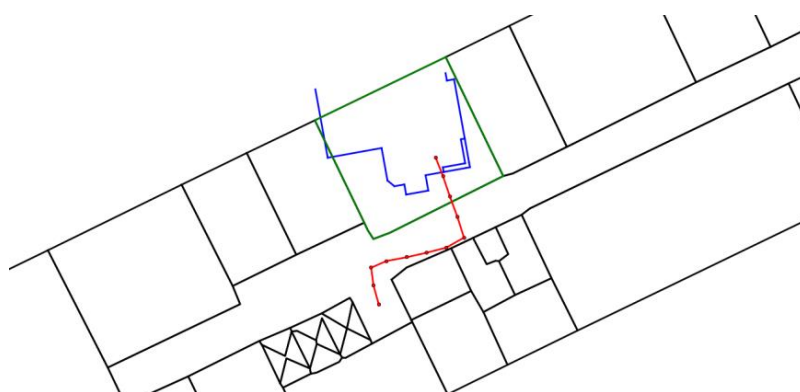


Figure 7.2 – Approximate registration to the coarse model. The user's track is identified in red, and the corresponding room in the coarse model by green.

7.1.2. Fine Registration

The approximate registration is further refined by the optimal fitting of the line segments in the detailed model to the corresponding line segments in the coarse model.

Finding the corresponding line segments: To find the line correspondences, first the line segments corresponding to the outer shell of the detailed model have to be derived by analyzing the convex hull of the model (figure 7.3 (a)). Possible changes in the room geometry due to renovations or addition of new structure elements cause the addition of new line segments only inside the room model. Therefore, the room's outer shell is assumed to be untouched, and consequently can be assigned to a wall (line segment) in the coarse model. The correspondences in the coarse model are then found by searching for the closest line segments having the most similar orientation. The search is performed using a ray tracing process, in which the corresponding line segments are assumed to be intersected by the same rays coming from the centroid of the model (figure 7.3 (b)). In order to deal with false assignments in case of having multiple candidates, which is often the case if the initial orientation is not accurate enough, candidates with the most similar orientations are selected. This assures a robust correspondence of line segments, if the initial orientation is estimated within a tolerance of $\pm 45^\circ$.

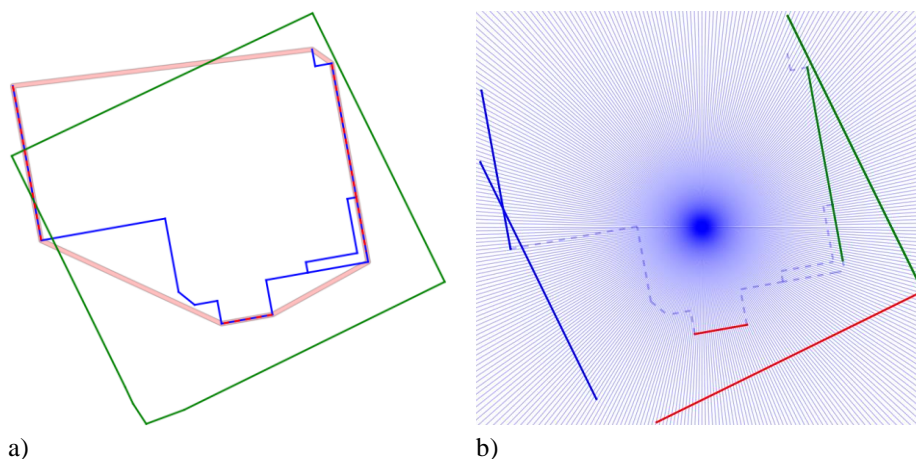


Figure 7.3 – Finding the corresponding line segments. a) Extracting the room's outer shell using the convex hull analysis (dashed lines); b) Ray tracing for finding the corresponding line segments in the detailed and coarse models.

Optimal fitting of the corresponding line segments: The corresponding line segments are optimally fitted together using a least squares adjustment. The adjustment model does not simply minimize the distance between the corresponding line segments (which is a “best fit”); instead, it firstly finds the best rotation that minimizes the orientation differences, and then the best translation that minimizes the distances between the corresponding line segments, in a separate process (here called an “optimal (constrained) fit”). The “best fit” and the “optimal fit” deliver different results in case of the shape asymmetry, as depicted in figure 7.4. The mathematical model of the “optimal fit” is presented as follows.

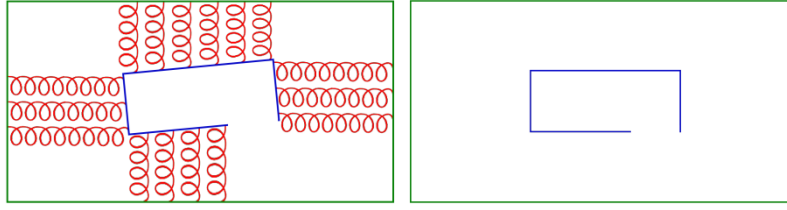


Figure 7.4 – A schematic comparison between the “best fit” (left) and the “optimal fit” (right) using the spring model for the distance minimization concept.

- a) For the estimation of the unknown rotation angle, the observation equation for each set of the line segments is given by:

$$d\alpha_i + \theta = e_i \quad (7.1)$$

in which, $d\alpha_i$ denotes the orientation difference between the corresponding line segments, θ is the unknown rotation and e_i is the corresponding residual. The Gauss-Markov linear model for the least squares adjustment for n observations can be written as:

$$\mathbf{A} = \begin{pmatrix} 1 \\ 1 \\ \vdots \\ 1 \end{pmatrix}_{n \times 1}, \quad \mathbf{L} = \begin{pmatrix} -d\alpha_1 \\ -d\alpha_2 \\ \vdots \\ -d\alpha_n \end{pmatrix}_{n \times 1}, \quad \mathbf{P} = \begin{pmatrix} l_1 & 0 & 0 & 0 \\ 0 & l_2 & 0 & 0 \\ & & \ddots & \\ 0 & 0 & 0 & l_n \end{pmatrix}_{n \times n}, \quad \mathbf{X} = (\theta)_{1 \times 1} \quad (7.2)$$

$$\mathbf{E} = \mathbf{e}^T \mathbf{P} \mathbf{e} = (\mathbf{L} - \mathbf{A} \mathbf{X})^T \mathbf{P} (\mathbf{L} - \mathbf{A} \mathbf{X}) \rightarrow \min \quad (7.3)$$

$$\Rightarrow \mathbf{X} = (\mathbf{A}^T \mathbf{P} \mathbf{A})^{-1} (\mathbf{A}^T \mathbf{P} \mathbf{L}) \quad (7.4)$$

in which, l_i is the length of the corresponding line in the detailed model, and \mathbf{P} is the weight matrix based on the length of the line segments.

- b) For estimating the unknown translation by minimizing the distance between the corresponding line segments, it is sufficient to minimize the distance between the centroid of the line segments in the detailed model and the corresponding line in the coarse model. In this case, for each set of the line segments one can write:

$$f_i(\mathbf{X}_T, \mathbf{Y}_T) = \frac{|a_i(\mathbf{X}_i + \mathbf{X}_T) + b_i(\mathbf{Y}_i + \mathbf{Y}_T) + c_i|}{\sqrt{a_i^2 + b_i^2}} \quad (7.5)$$

in which, $f_i(\mathbf{X}_T, \mathbf{Y}_T)$ is the distance between the centroid of a line segment in the detailed model $(\mathbf{X}_i, \mathbf{Y}_i)$ to the corresponding line $a_i x + b_i y + c_i = 0$ in the coarse models, after applying the translation $\mathbf{X}_T, \mathbf{Y}_T$ to the centroid $(\mathbf{X}_i, \mathbf{Y}_i)$. Therefore, the observation equation can be written as:

$$f_i(\mathbf{X}_{T0} + \Delta \mathbf{X}_T, \mathbf{Y}_{T0} + \Delta \mathbf{Y}_T) - f_i(\mathbf{X}_{T0}, \mathbf{Y}_{T0}) = e_i \quad (7.6)$$

The Gauss-Markov linear model for the least squares adjustment for n observations is given by:

$$\mathbf{A}_i = \left(\begin{array}{c} \frac{\partial f_i}{\partial X} \Big|_{X_{T0}} \\ \frac{\partial f_i}{\partial Y} \Big|_{Y_{T0}} \end{array} \right), \quad \mathbf{L}_i = (-f_i(X_{T0}, Y_{T0}))$$

$$\mathbf{A} = \begin{pmatrix} \mathbf{A}_1 \\ \mathbf{A}_2 \\ \vdots \\ \mathbf{A}_n \end{pmatrix}_{n \times 2}, \quad \mathbf{L} = \begin{pmatrix} \mathbf{L}_1 \\ \mathbf{L}_2 \\ \vdots \\ \mathbf{L}_n \end{pmatrix}_{n \times 1}, \quad \mathbf{P} = \begin{pmatrix} 1_1 & 0 & 0 & 0 \\ 0 & 1_2 & 0 & 0 \\ & & \ddots & \\ 0 & 0 & 0 & 1_n \end{pmatrix}_{n \times n}, \quad \boldsymbol{\delta} = (\Delta X_T \quad \Delta Y_T)_{1 \times 2} \quad (7.7)$$

$$\mathbf{E} = \mathbf{e}^T \mathbf{P} \mathbf{e} = (\mathbf{L} - \mathbf{A} \boldsymbol{\delta})^T \mathbf{P} (\mathbf{L} - \mathbf{A} \boldsymbol{\delta}) \rightarrow \min \quad (7.8)$$

$$\Rightarrow \boldsymbol{\delta} = (\mathbf{A}^T \mathbf{P} \mathbf{A})^{-1} (\mathbf{A}^T \mathbf{P} \mathbf{L}) \quad (7.9)$$

Since the observation equation is non-linear with respect to the unknowns, the unknown translation is estimated iteratively. In each iteration, the estimated translation is updated by:

$$\begin{aligned} X_T &= X_{T0} + \Delta X_T \\ Y_T &= Y_{T0} + \Delta Y_T \end{aligned} \quad (7.10)$$

As the door thickness in comparison to the wall thickness is usually negligible, the coincident of the line segments corresponding to the door serves as a constraint in the adjustment process. Figure 7.5 depicts the results of the constrained fit for the previous example.

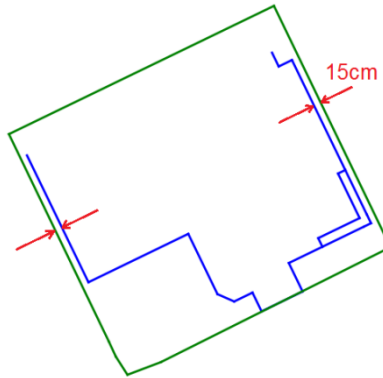


Figure 7.5 – Optimal fitting of the detailed model to the coarse model. Fitting residuals close to a typical value within a tolerance (e.g. 10-20cm) are considered as the wall thickness.

7.2. Fusion of Detailed Models to the Coarse Model

Computing the wall thickness: The actual value for the wall thickness is detectable after the registration process, by analyzing the registration residuals (distance between the corresponding line segments after the registration). In other words, residuals close to a typical value within a threshold (e.g. 10-20cm) are considered as the actual wall thickness for the room (see figure 7.5). The information about the wall thickness enables a correct fusion, and at the same time, a comparison between the detailed and the coarse models for finding the changes in the building interiors and updates to the coarse model.

Model fusion and gap filling: After the registration of the detailed models to the coarse model, they have to be merged in a consistent way. Therefore, besides coincidence and merging of the doors in the previous step, possible gaps in the detailed models have to be reconstructed based on the shape of the coarse model. In other words, the gap parts are reconstructed by following the shape of the coarse

model, considering the wall thickness. This is realized by generating a parallel buffer (equivalent to the wall thickness) inside the corresponding rooms in the coarse model (figure 7.6 (a)), and filling the gap parts using the buffer shell. For this purpose, the line segments in the detailed model are first converted to graph edges (figure 7.6 (b)), and those containing a free end node (nodes of degree 1) will be extended simultaneously in the original and perpendicular directions, in order to find their first intersection with the offset shell (figure 7.6 (c)). Assuming the gap parts are less than 50% of the corresponding detailed model, edges constituting the shortest path from the two most distant degree 1 nodes will be merged to the detailed model to fill the gaps (figure 7.6 (d)). Figure 7.7 depicts the fusion of the detailed model of some exemplary rooms with the coarse model using this approach. As already mentioned, the approach does not deal with the cases in which the detailed model is larger than the coarse model (see the rooms number 1 and 7 in figure 7.7), or multiple rooms are merged together (see the free space between rooms number 5 and 6). The main steps for the reconstruction of the detailed models of this example are provided in appendix E.

Change detection: As already mentioned, computing the wall thickness enables the detection of the changes to the coarse model; walls outside of a buffer equivalent to the wall thickness are considered as updates to the coarse model. Updates in the mentioned example are distinguished in figure 7.8 using a different color.

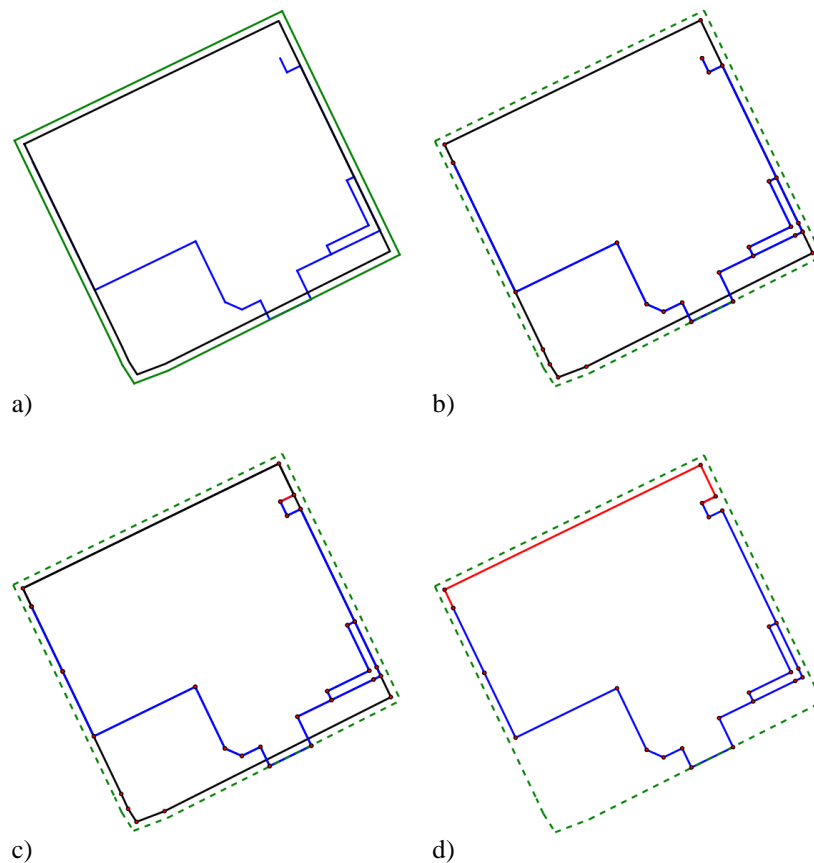


Figure 7.6 – a) Generating a parallel offset (black) inside the coarse model (green); b) Converting the line segments into graph edges; c) Connecting the degree 1 nodes in the detailed model to the offset shell ; d) Reconstructing the gaps by finding the shortest path between the two most distant degree 1 nodes in the detailed model (red).

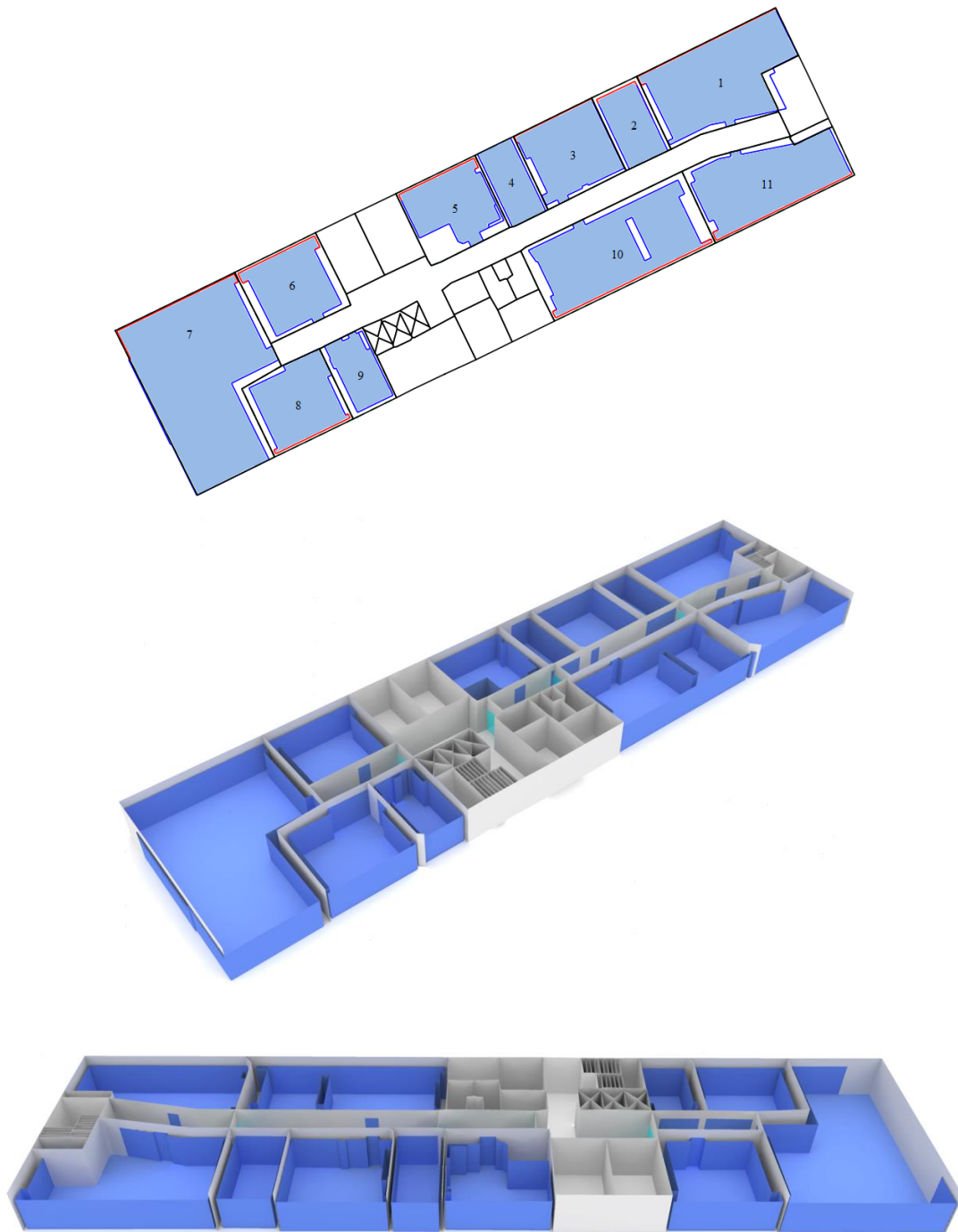


Figure 7.7 – Refinement of the coarse model by the fusion of detailed models. Top: reconstructed gaps are marked by the red color in the top view; Middle and bottom: perspective views (front walls in the coarse model are removed for the visibility purpose).

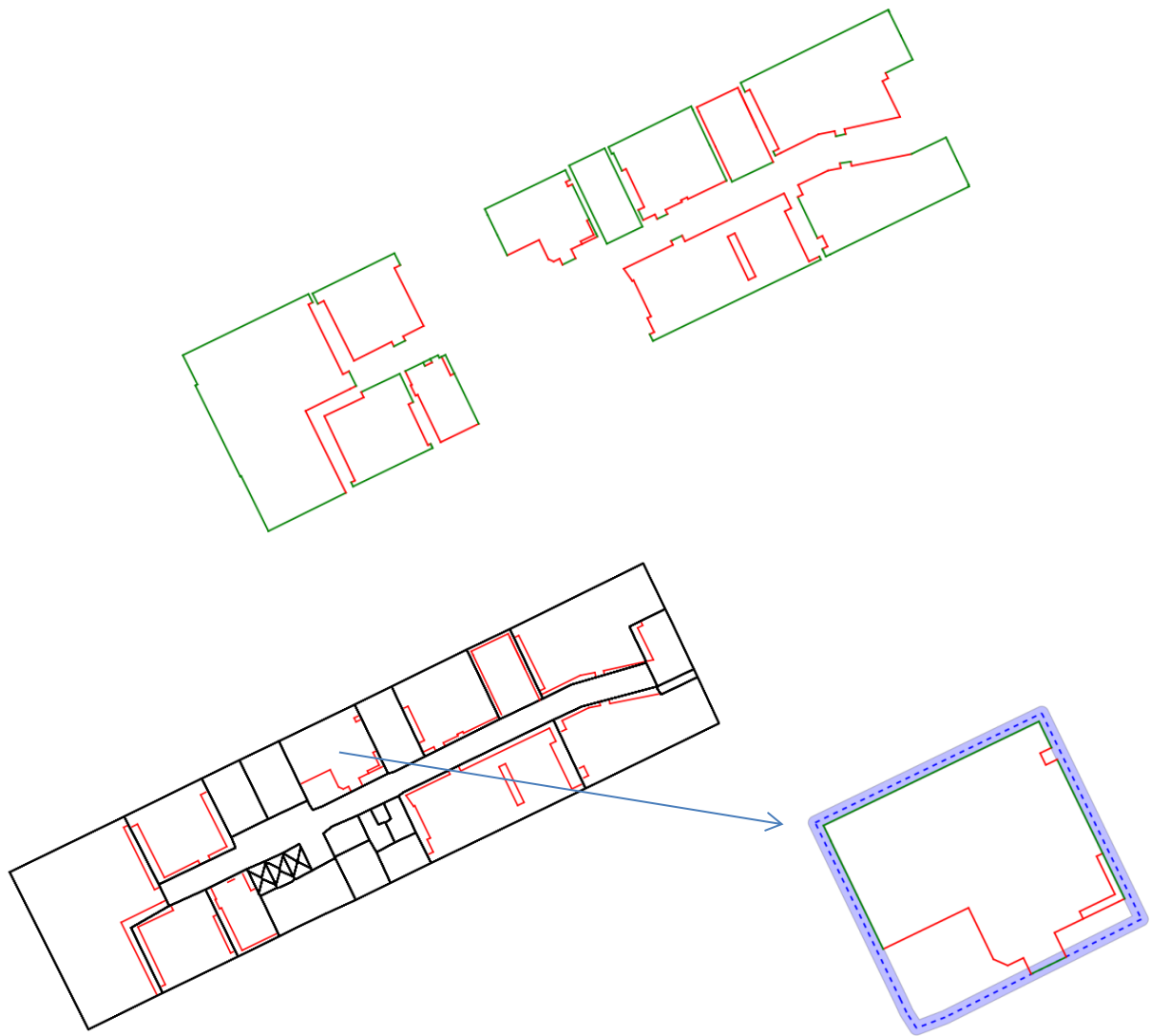


Figure 7.8 – Walls outside of the buffer (red) are considered as update to the coarse model.

8. Conclusion

8.1. Summary

This work investigated the automatic reconstruction of building interiors using low-cost sensor systems. The system developed for this purpose consists of two main parts: data acquisition and 2D/3D model reconstruction.

The data acquisition part focused on using state-of-the-art low-cost sensor systems for the collection of range data in indoor scenes. Microsoft Kinect was selected as the case study, and the system calibration together with the computation of 3D object coordinates were focused for this sensor system. Afterwards, available approaches for the registration of Kinect point clouds were presented, and a new complementary approach was proposed.

In the modeling part, the registered point clouds were first pre-processed in order to remove the furniture and clutter, reduce the noise of the range measurements, level the point cloud and project the points onto the ground plane. An orthographic projected image was then computed, in order to enable the modeling process in 2D space. Converting the reconstruction problem from 3D to 2D, besides simplification of the reconstruction task, enables efficient topological corrections using algebraic relationships and graph theories. The modeling process consists of estimating the line segments (corresponding to walls in 3D) together with some proposed topological corrections. The results were converted back to 3D using an extrusion. The parameters used in the modeling algorithm were discussed, and criteria for a correct parameter selection were presented. Experimental results demonstrated the robustness of the reconstruction approach, as well as the stability of the selected parameters in different scenarios, where different sensor types and different room shapes and sizes were used.

Finally, as an application of the proposed reconstruction approach, it was shown how the resulted 3D models with a higher level of details can be used to refine available coarse floor plans. During the refinement process, existing gaps in the detailed models were automatically reconstructed using the information derived from the coarse model.

8.2. Contributions

The contributions of this work can be summarized in the following parts:

Registration problem: Available approaches for the registration of point clouds collected from indoor scenes mainly rely on visual features extracted from color images, as well as geometrical information extracted from the range data. Such approaches fail in scenarios, where not enough well-distributed visual features can be observed, or geometrical constraints cannot fix the sensor 6 DOF. Therefore, a new complementary approach is introduced, in order to support the registration task by employing the

user's track information derived from an indoor positioning method, based on a foot mounted MEMS IMU.

Line estimation, clustering and topological corrections: Available 2D reconstruction approaches mostly directly deliver the output of the line estimation process (e.g. using the Hough transform) as the final results. Therefore, the line estimation parameters play an important role in the final results, and a suitable balance has to be made between the noise level, the required level of details and the expected length of the line segments, in order to estimate each wall by a single line segment. In practice, the problem is usually handled by estimating the parameters in a typical scenario, and using the same parameters in similar cases. In the proposed approach, this problem is managed more efficiently. Inputs for the modeling algorithm provided by different sensors (with different noise levels) are firstly homogenized using a pre-processing step with minimal user interactions. Then the line estimation parameters are set in a way that the smallest allowed features are taken into account. Although this results in the estimation of each wall by multiple smaller line segments, the proposed hierarchical clustering algorithm assigns the resulting line segments to the corresponding walls. It enables the averaging and merging of multiple line segments, in order to estimate each wall by a single line segment. The results are further improved using the proposed topological steps to correct small line orientation errors (parallelism and perpendicularity check), and to assure a correct intersection between the line segments (extension and trim algorithm). Moreover, small gaps in the model are detected and filled by the extension of free end points (degree 1 nodes in the corresponding graph) in the original and perpendicular directions. This results in the reconstruction of interiors with an arbitrary level of details.

Reconstruction of larger gaps in the models and refinement of available coarse models: Available coarse models (e.g. those derived from architectural drawings and floor plans) can be further refined by the fusion of the reconstructed model with the coarse model. For this purpose, a fusion algorithm is suggested, which also enables the reconstruction of remaining gaps in the detailed models using a learning-based approach based on the information derived from the coarse model and the fusion process. In other words, gaps are reconstructed by merging walls parallel to coarse model, considering the wall thickness (the term "learning" refers to the prediction of gaps from the behavior of the coarse model).

8.3. Future Work

The presented work has the potential of being used by the public for crowdsourcing, due to the affordability and accessibility of range measurement systems in the recent years. For this purpose, the following optimizations and extensions are suggested based on the experience gained in this work.

Visual user guides for the data acquisition task: The data acquisition task can be a challenge, if the interior space is too complex and large, or the registration fails due to the weak estimation of the sensor pose. Failures are revealed only after the data processing step. Therefore, it is required to make use of SLAM and visual tracking techniques in order to develop an Augmented Reality system that is able to guide the user in the data acquisition task, to assure a complete and faultless data acquisition. This can be realized by the use of tablets or wearable devices such as Google Glass. Some of the available business products have already integrated such features (e.g. DPI-7/8 handheld scanners), however, the capability of capturing larger spaces and improving the tracking module by the fusion of visual and geometrical features can still improve the performance of the systems.

Improving the pose estimation: As already mentioned, for an accurate registration of the range data, one may benefit from the combination of visual and geometrical features. The GPU-based RGB-D

odometry presented by (Whelan et al., 2013) is a successful example in this field. However, in public buildings, indoor scenes usually have poor visual texture or geometrical features. In such scenarios, one may benefit from the extraction and matching of line features instead of point features. Line-based SLAM approaches are well-suited for this purpose. Therefore, replacing the method used in this work (SfM) with such approaches can improve the registration results in challenging scenarios.

Extending the model fusion algorithm: In this work, a model fusion approach for the update or refinement of coarse floor plan was introduced. The algorithm does not consider the case that a room in the coarse model is split, or multiple rooms are merged together, or the room in the coarse model is smaller than the corresponding detailed model. Therefore, including such cases in the algorithm is required.

Extending the floor model reconstruction approach: The presented approach for the reconstruction of a complete floor model is based on the reconstruction of individual rooms, and fusing the results with an available coarse model. An extension to this work is the reconstruction of complete floor models from point clouds, independent from the existence of coarse models. For this purpose, the proposed topological concepts have to be extended, in order to assure a correct and consistent reconstruction and combination of different rooms and hallways. The performance of grammar-based approaches in this field is encouraging.

A. Point Cloud Registration – Fundamental Principles

As already mentioned in section 2.2.1, two point clouds are registered using a rigid-body transformation (Figure A.1). The transformation is a special case of a 7-parameters 3D similarity (Helmert's 7-parameters) transformation, in which the scale factor is set to 1 (equations (A.1)). The rigid-body transformation parameters can be estimated using point correspondences in the point clouds. Closed-form solutions can be used in case the point correspondences are known, otherwise the point correspondences are estimated using the ICP algorithm.

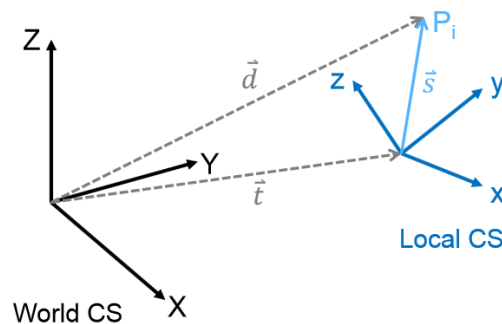


Figure A.1 – Rigid-body transformation. (figure and the corresponding relationships from Fritsch (2014))

$$\begin{pmatrix} X \\ Y \\ Z \end{pmatrix}_i = \mathbf{R} \cdot \begin{pmatrix} x \\ y \\ z \end{pmatrix}_{ij} + \begin{pmatrix} t_x \\ t_y \\ t_z \end{pmatrix}_j \quad (\text{A.1})$$

$$\mathbf{d} = f(\mathbf{s}) = \mathbf{R}\mathbf{s} + \mathbf{t} \quad (\text{A.2})$$

In this equation:

- \mathbf{d} is the point in the world coordinate system;
- \mathbf{s} is the point in the local coordinate system;
- \mathbf{R} is the rotation matrix;
- \mathbf{t} is the translation vector.

A.1. Closed-Form Solution

Equations (A.1) can be solved using the least squares adjustment; however, this needs initial values and linearization of the equations with respect to the unknown rotation angles. This not only slows down the convergence, but also may cause singularities in the system of equations. To avoid these issues, closed form solutions are proposed based on the unit quaternions, e.g. by (Horn, 1987; Sanso, 1973). A quaternion as a representation of rotation is known to be well-conditioned in numerical solutions for the orientation problem to avoid singularities. A quaternion has four elements that uniquely represent a rotation in the space:

$$\mathbf{q} = (q_0, q_1, q_2, q_3) \quad (\text{A.3})$$

According to Jain et al. (1995), in order to understand how quaternions encode rotations in the 3D space, one can compare it with a circle in 2D and a sphere in 3D. In 2D, any position on the unit circle in the xy plane encodes a rotation around the z axis. The equation of the unit circle in 2D is given by:

$$X^2 + Y^2 = 1 \quad (\text{A.4})$$

In 3D, any position on the unit sphere encodes rotations around only two axes. The implicit equation of the unit sphere is given by:

$$X^2 + Y^2 + Z^2 = 1 \quad (\text{A.5})$$

In analogy, in order to represent three rotations, another degree of freedom is required. Three rotations are encoded by a position on the unit quaternion in 4D, which is defined by:

$$q_0^2 + q_1^2 + q_2^2 + q_3^2 = 1 \quad (\text{A.6})$$

The rotation matrix \mathbf{R} can be derived based on the elements of the unit quaternion:

$$\mathbf{R}(\mathbf{q}) = \begin{pmatrix} q_0^2 + q_1^2 - q_2^2 - q_3^2 & 2(q_1q_2 - q_0q_3) & 2(q_1q_3 + q_0q_2) \\ 2(q_1q_2 + q_0q_3) & q_0^2 + q_2^2 - q_1^2 - q_3^2 & 2(q_2q_3 - q_0q_1) \\ 2(q_1q_3 - q_0q_2) & 2(q_2q_3 - q_0q_1) & q_0^2 + q_3^2 - q_1^2 - q_2^2 \end{pmatrix} \quad (\text{A.7})$$

By denoting the rotation axis by the unit vector $\boldsymbol{\omega} = (\omega_x, \omega_y, \omega_z)$ and the Cartesian axes unit vectors by \mathbf{i} , \mathbf{j} and \mathbf{k} , the rotation axis can be represented by:

$$\boldsymbol{\omega} = \omega_x \mathbf{i} + \omega_y \mathbf{j} + \omega_z \mathbf{k} \quad (\text{A.8})$$

The unit quaternion for a counterclockwise rotation θ around this axis can be represented by:

$$\begin{aligned} \mathbf{q} &= \cos\left(\frac{\theta}{2}\right) + \sin\left(\frac{\theta}{2}\right)(\omega_x \mathbf{i} + \omega_y \mathbf{j} + \omega_z \mathbf{k}) \\ &= q_0 + q_x \mathbf{i} + q_y \mathbf{j} + q_z \mathbf{k} \end{aligned} \quad (\text{A.9})$$

which consists of a scalar (real) part and a vector (imaginary) part.

Let be S a set of N points in \mathbf{R}^3 in the local coordinate system, and D a set of corresponding points in the world coordinate system, the rigid-body transformation $\mathbf{T}(\hat{\mathbf{q}}, \mathbf{t})$ is obtained by solving:

$$E: \sum_{i=0}^{N-1} \|\mathbf{d}_i - \mathbf{R}\mathbf{s}_i + \mathbf{t}\| \rightarrow \min \quad (\text{A.10})$$

in which $\mathbf{R} = \mathbf{R}(\hat{\mathbf{q}})$ and \mathbf{t} are the rotation and translation matrices.

By computing the centroid of the points in the corresponding coordinate systems:

$$\bar{\mathbf{d}} = \frac{1}{N} \sum_{i=0}^{N-1} \mathbf{d}_i; \bar{\mathbf{s}} = \frac{1}{N} \sum_{i=0}^{N-1} \mathbf{s}_i; \mathbf{d}' = \mathbf{d}_i - \bar{\mathbf{d}}; \mathbf{s}' = \mathbf{s}_i - \bar{\mathbf{s}} \quad (\text{A.11})$$

and constructing an auxiliary matrix \mathbf{M} :

$$\mathbf{M} = \sum_{i=0}^{N-1} \mathbf{d}_i' \mathbf{s}_i'^T = \begin{pmatrix} \mathbf{S}_{xx} & \mathbf{S}_{xy} & \mathbf{S}_{xz} \\ \mathbf{S}_{xy} & \mathbf{S}_{yy} & \mathbf{S}_{yz} \\ \mathbf{S}_{xz} & \mathbf{S}_{yz} & \mathbf{S}_{zz} \end{pmatrix} \quad (\text{A.12})$$

and a further auxiliary symmetric matrix \mathbf{N} :

$$\mathbf{N} = \begin{pmatrix} \mathbf{S}_{xx} + \mathbf{S}_{yy} + \mathbf{S}_{zz} & \mathbf{S}_{yz} - \mathbf{S}_{zy} & \mathbf{S}_{zx} - \mathbf{S}_{xz} & \mathbf{S}_{xy} - \mathbf{S}_{yx} \\ \mathbf{S}_{yz} - \mathbf{S}_{zy} & \mathbf{S}_{xx} - \mathbf{S}_{yy} - \mathbf{S}_{zz} & \mathbf{S} + \mathbf{S} & \mathbf{S}_{zx} + \mathbf{S}_{xz} \\ \mathbf{S}_{zx} - \mathbf{S}_{xz} & \mathbf{S}_{xy} + \mathbf{S}_{yx} & -\mathbf{S}_{xx} + \mathbf{S}_{yy} - \mathbf{S}_{zz} & \mathbf{S}_{yz} + \mathbf{S}_{zy} \\ \mathbf{S}_{xy} - \mathbf{S}_{yx} & \mathbf{S}_{zx} + \mathbf{S}_{xz} & \mathbf{S}_{yz} + \mathbf{S}_{zy} & -\mathbf{S}_{xx} - \mathbf{S}_{yy} - \mathbf{S}_{zz} \end{pmatrix} \quad (\text{A.13})$$

the singular value decomposition of \mathbf{N} delivers singular values and the corresponding vectors; the largest one represent the rotation matrix $\mathbf{R} = \mathbf{R}(\hat{\mathbf{q}})$.

The translation vector is finally given by:

$$\mathbf{t} = \mathbf{d} - \mathbf{R}\mathbf{s} \quad (\text{A.14})$$

A.2. Iterative Solution (ICP)

If the point correspondences are not provided for the calculation of the rigid-body transformation, the estimation of the transformation can be performed using common object surfaces in both point clouds. However, as also stated by Luhmann et al. (2014), the common surfaces must have at least three linearly independent normal vectors to achieve a unique solution. Moreover, if the common surfaces contain only one symmetrical shape such as sphere or plane, the registration is not possible. The most well-known registration algorithm based on common parts in the point cloud is the Iterative Closest Point (ICP) algorithm (Besl and McKay, 1992). The algorithm is an iterative procedure. Assuming the point cloud B has to be registered with the point cloud A, in each iteration, for every point in the point cloud B, a point in the point cloud A with smallest Euclidean distance is assigned. Based on the assigned correspondences, a rigid-body transformation is estimated, and is applied to the point cloud B. The iteration is continued by finding a new set of point correspondences, estimating the transformation and applying it, until the RMS of the distances is less than a given threshold (see Figure A.2).

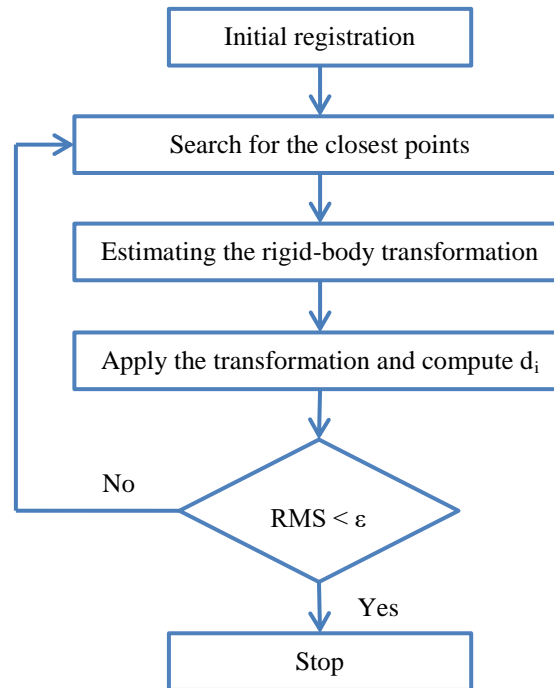


Figure A.2 – Flow diagram for the ICP algorithm. (adapted from Luhmann et al. (2014))

Distance Minimization

For the minimization of distances between the corresponding points in point clouds A and B, parameters of the corresponding rigid-body transformation have to be estimated. The mathematical model of the transformation is given by:

$$\mathbf{X}_A = \mathbf{X}_{0B} + \mathbf{R}(\mathbf{X}_B - \mathbf{X}_{0B}) \quad (\text{A.15})$$

Assuming small (differential) rotation angles, the rotation matrix is given by:

$$\mathbf{R} = \mathbf{R}(d\alpha, d\beta, d\gamma) = \begin{pmatrix} 1 & d\gamma & -d\beta \\ -d\gamma & 1 & d\alpha \\ d\beta & -d\alpha & 1 \end{pmatrix} \quad (\text{A.16})$$

Additionally, assuming small translation parameters, the transformation model can be replaced by the following linear model:

$$\mathbf{X}_A - \mathbf{X}_B = \mathbf{X}_{0B} + \mathbf{B} \cdot d\mathbf{X}_B \quad (\text{A.17})$$

where:

$$d\mathbf{X}_B = (dX_0 \ dY_0 \ dZ_0 \ d\alpha \ d\beta \ d\gamma)_B^t \quad (\text{A.18})$$

is the vector of unknowns containing 3 rotation angles and 3 translation elements, and:

$$\mathbf{B} = \begin{pmatrix} dX_0 & dY_0 & dZ_0 & d\alpha & d\beta & d\gamma \\ 1 & 0 & 0 & 0 & -\Delta Z_{iB} & \Delta Y_{iB} \\ 0 & 1 & 0 & \Delta Z_{iB} & 0 & -\Delta X_{iB} \\ 0 & 0 & 1 & -\Delta Y_{iB} & \Delta X_{iB} & 0 \\ \dots & & & \dots & & \end{pmatrix} \quad (\text{A.19})$$

is the coefficient matrix containing partial derivatives with respect to the unknowns, in which i denotes the point index.

The unknowns are estimated by iteration, if appropriate initial values for the unknowns are provided. In each iteration, after the estimation of the unknowns, the coordinates of the points in the point cloud B are updated. The iteration is continued until the estimated unknowns (differential rotation and translation elements) are smaller than a given threshold.

According to Fritsch (2014), the appropriate adjustment model for solving equation (A.17) is the Gauß-Helmert model, since also the right side of the equation contains measured coordinates:

$$\mathbf{A}\mathbf{v} + \mathbf{B}\mathbf{x} + \mathbf{w} = \mathbf{0}; \quad D(\mathbf{l}) = \sigma^2 \mathbf{P}^{-1} \quad (\text{A.20})$$

In more detail, the update equations for every point correspondence are expressed by:

$$\begin{aligned} & (X_{iA} + v_{X_{iA}}) - (X_{iB} + v_{X_{iB}}) - (X_{00B} + dX_{0B}) + \\ & (\Delta Z_{iB} + v_{\Delta Z_{iB}})(\Delta\beta_0 + d\beta) - (\Delta Y_{iB} + v_{\Delta Y_{iB}})(\Delta\gamma_0 + d\gamma) = 0 \\ & (Y_{iA} + v_{Y_{iA}}) - (Y_{iB} + v_{Y_{iB}}) - (Y_{00B} + dY_{0B}) - \\ & (\Delta Z_{iB} + v_{\Delta Z_{iB}})(\Delta\alpha_0 + d\alpha) + (\Delta X_{iB} + v_{\Delta X_{iB}})(\Delta\gamma_0 + d\gamma) = 0 \\ & (Z_{iA} + v_{Z_{iA}}) - (Z_{iB} + v_{Z_{iB}}) - (Z_{00B} + dZ_{0B}) + \\ & (\Delta Y_{iB} + v_{\Delta Y_{iB}})(\Delta\alpha_0 + d\alpha) - (\Delta X_{iB} + v_{\Delta X_{iB}})(\Delta\beta_0 + d\beta) = 0 \end{aligned} \quad (\text{A.21})$$

where, $X_{00B}, Y_{00B}, Z_{00B}, \Delta\alpha_0, \Delta\beta_0, \Delta\gamma_0$ are the initial (approximate) values of the unknown parameters. Therefore, the coefficient matrices in the equation (A.20) are given by:

$$\mathbf{A} = \begin{pmatrix} v_{X_{iA}} & v_{Y_{iA}} & v_{Z_{iA}} & v_{X_{iB}} & v_{Y_{iB}} & v_{Z_{iB}} & v_{\Delta X_{iB}} & v_{\Delta Y_{iB}} & v_{\Delta Z_{iB}} \\ 1 & 0 & 0 & -1 & 0 & 0 & 0 & -\Delta\gamma_0 & \Delta\beta_0 \\ 0 & 1 & 0 & 0 & -1 & 0 & \Delta\gamma_0 & 0 & -\Delta\alpha_0 \\ 0 & 0 & 1 & 0 & 0 & -1 & -\Delta\beta_0 & \Delta\alpha_0 & 0 \end{pmatrix} \quad (\text{A.22})$$

$$\mathbf{B} = \begin{pmatrix} dX_o & dY_o & dZ_o & d\alpha & d\beta & d\gamma \\ -1 & 0 & 0 & 0 & \Delta Z_{iB} & -\Delta Y_{iB} \\ 0 & -1 & 0 & -\Delta Z_{iB} & 0 & \Delta X_{iB} \\ 0 & 0 & -1 & \Delta Y_{iB} & \Delta X_{iB} & 0 \end{pmatrix} \quad (\text{A.23})$$

$$\mathbf{w} = \begin{pmatrix} X_{iA} - X_{iB} - X_{00B} + \Delta Z_{iB} \Delta \beta_0 - \Delta Y_{iB} \Delta \gamma_0 \\ Y_{iA} - Y_{iB} - Y_{00B} - \Delta Z_{iB} \Delta \alpha_0 + \Delta X_{iB} \Delta \gamma_0 \\ Z_{iA} - Z_{iB} - Z_{00B} + \Delta Y_{iB} \Delta \alpha_0 - \Delta X_{iB} \Delta \gamma_0 \end{pmatrix} \quad (\text{A.24})$$

Normal equations are given by:

$$\begin{pmatrix} \mathbf{A}\mathbf{P}^{-1}\mathbf{A} & \mathbf{B} \\ \mathbf{B}^t & \mathbf{0} \end{pmatrix} \begin{pmatrix} \hat{\boldsymbol{\lambda}} \\ \hat{\mathbf{X}} \end{pmatrix} = \begin{pmatrix} -\mathbf{w} \\ \mathbf{0} \end{pmatrix} \quad (\text{A.25})$$

which are solved by iteration to estimate the unknown vector $\hat{\mathbf{X}}$ containing the transformation parameters.

This is the strict solution of the ICP algorithm. Although there are modifications and other variants for this algorithm (e.g. different search algorithms or point-to-plane distance minimization instead of point-to-point distance), the main steps which are described in Figure A.2 remain essentially the same.

B. RANSAC

Random Sample Consensus (RANSAC) is an adjustment algorithm presented by Fischler and Bolles (1981), based on a voting scheme. The model is suitable for the estimation of any functional model from a set of observations containing a significant number of gross errors, even up to 80% (Schnabel et al., 2007). Opposed to many classical algorithms that fit the model to all of the presented data, this algorithm estimate the model parameters from a minimum set of observations using an iterative procedure.

In more detail, as described by Luhmann et al. (2014), the algorithm first randomly selects a minimum required number of observations from the full set of the observations in order to estimate the model parameters. Afterwards, all the remaining observations are tested against the estimated model, their residuals are computed, and those which are consistent with the model within a certain tolerance are regarded as valid observations and form a consensus set. The procedure is repeated using a new set of random observations to create a new consensus set. After some iterations, the model corresponding to the consensus set with the maximum number of valid observations is regarded as the best solution. The success of the algorithm depends on the mentioned tolerance and the termination criterion which can be the number of iterations, or the minimum size of the consensus set. Probabilistic criterions for the minimum number of iterations or the minimum size of the consensus set are proposed by (Fischler and Bolles, 1981). For instance, assuming w be the probability that any selected data is within the error tolerance of the model, k the number of trials required to select a subset of n valid observations, in order to ensure with probability of z that at least one of the random selections is an error-free set on n observations, then the number of iterations is given by:

$$b = w^n$$

$$(1 - b)^k = (1 - z)$$

$$k = \frac{\log(1 - z)}{\log(1 - b)} \tag{B.1}$$

According to Fischler and Bolles (1981), the algorithm is very well-suited for applications in automated image analysis that rely on the data provided by error-prone feature detectors, such as relative orientation. Other applications are for instance data association (e.g. 2D or 3D points in different coordinate systems), feature detection and fitting of geometric primitive to a set of points (e.g. line and circle in 2D or sphere and plane in 3D).

C. SLAM Problem

Simultaneous Localization And Mapping (SLAM) was originally introduced by Leonard and Durrant-Whyte (1991) based on the work of Smith et al. (1990) for mobile robot navigation. SLAM aims at creating a map of an unknown environment, while at the same time localizing the mobile robot within the environment. In fact, the localization supports the mapping process, and the created map supports the continuation of the localization process, similar to the well-known “chicken and egg” problem.

Figure C.1 illustrated this concept for a mobile robot using an example provided by (Frese et al., 2010). In this example, the robot observes the environment (artificial features on the floor) relative to its own unknown location using a camera mounted on the top of it. At the same time, the robot relative motion is measured using odometry. If the environment was known, the robot’s pose could be estimated using the provided observations (called localization). Conversely, if the robot’s pose was known, measuring the feature points could lead the positioning of the points in a global reference frame (called mapping). In general, neither the environment is known, nor the robot’s pose; they both have to be estimated using the same data (called simultaneous localization and mapping).

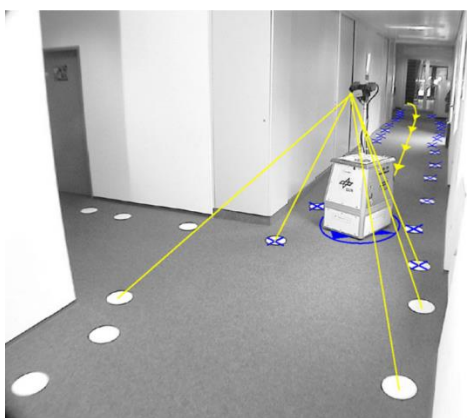


Figure C.1 – A mobile robot observes the environment and measures its relative motion, in order to estimate its pose and the scene geometry using a SLAM algorithm. (from Frese et al. (2010))

According to Riisgaard and Blas (2003), the standard SLAM process typically consists of following steps:

- a) **Landmark extraction:** Landmarks are the features that can be re-observed by the robot and be distinguished in the environment for the localization purpose. Depending on the type of the SLAM variant, landmarks can be extracted from different sources of data, e.g. laser scan data or image features.
- b) **Data association:** This problem deals with the searching and matching of the landmarks in an uncertainty area, in order to realize if a landmark has been re-observed.
- c) **State estimation:** In this step, it is assumed that the map is provided, and at least temporarily it does not require any update. When the odometry data is changed, the robot pose is estimated

using the new data (e.g. laser scan data, IMU data and visual features). This can be performed using different solutions, such as filtering methods (e.g. Extended Kalman Filter (EKF)) or keyframe-based methods that optimizes the solution using a bundle adjustment.

- d) State update: The robot's state is updated, as soon as landmarks are re-observed, in order to reduce errors in the pose estimation.
- e) Landmark update: Extracted landmarks which have not been observed before are regarded as new landmarks and added to the landmarks library.

Each of the mentioned steps of the SLAM process can be modified based on the application requirements. In the overview presented by Frese et al. (2010), different types of applications are distinguished, in which the standard SLAM algorithm is modified, in order to fulfil special requirements of the application:

Offline-SLAM for mapping (map learning): In such applications, the robot is manually navigated within the environment and sensor data is recorded. Then in a post-processing step, a map is computed using the computed trajectory. The map is later used for the actual operation of the system, e.g. localization, rout planning, etc.

Online-SLAM for localization: In this SLAM mode, both localization and mapping are performed in real-time, but the application only uses the localization results, and the mapping is performed just to support the localization. In this mode, the whole or parts of the map are known; therefore, the localization error only grows when the map has to be extended.

Online-SLAM for continuously updating the map: This mode is the most complex way of using SLAM, which is also the main motivation of SLAM research. In this mode, the map is generated and extended and the robot is localized within the generated map. Both localization and mapping results are further used for the robot navigation purpose.

The SLAM problem is a very active topic of research and still many problems have to be solved in order to reach a fully automated approach for the robot navigation and exploration in real world scenarios.

D. Hough Transform

D.1. Standard Hough Transform

Hough transform (Duda and Hart, 1972; Hough, 1962) extracts a certain class of shapes (most commonly lines, circles or ellipses) in a binary image, based on a voting scheme. The voting process is performed in a parameter space, which is defined by the parametric representation of the shape. For instance for the extraction of straight lines or collinear points in an image, the parameter space is defined by (ρ, θ) , $\theta \in [0, \pi]$, corresponding to the slope-intercept representation of the line (equation (D.1)). In this space, points in the (x, y) domain are represented by sinusoidal curves, and straight lines by points which are the intersection of sinusoidal curves corresponding to collinear points (see Figure D.1). Likewise, points lying on the same sinusoidal curves correspond to lines passing through a common point in the (x, y) domain.

The Hough transform algorithm detects lines (collinear points) in the (x, y) domain using a two dimensional array corresponding to (ρ, θ) , called an accumulator. The size of the array depends on the quantization error (step size) of ρ and θ values. Each cell in the accumulator is incremented by the number of curves passing through the corresponding point in the (ρ, θ) domain. Therefore, the count in a given cell (ρ_i, θ_i) determines how many points in the (x, y) domain lie along the line whose parameters are (ρ_i, θ_i) . The algorithm afterwards searches for the cells having counts more than a given threshold (counts are the number of collinear points for that line within the quantization error).

$$\rho = x \cos(\theta) + y \sin(\theta)$$

(D.1)

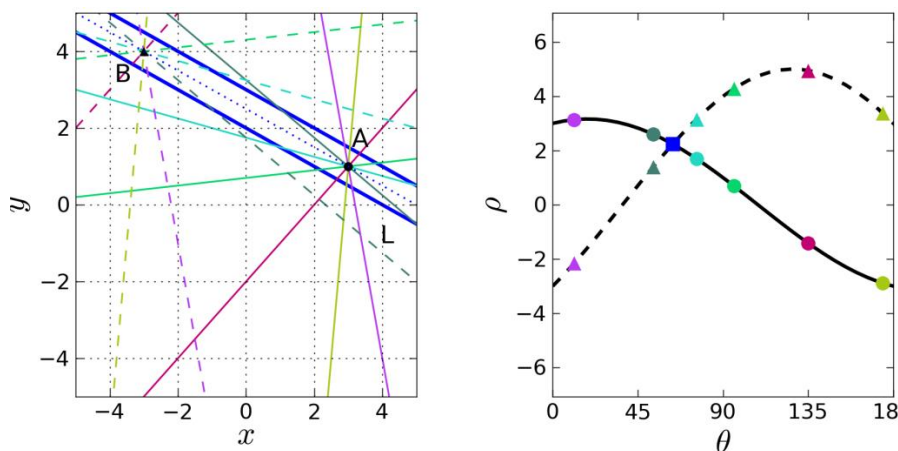


Figure D.1 – Hough transform concept for the extraction of lines. (from “EBS-Image, Hough Transform” (2011))

D.2. Progressive Probabilistic Hough Transform

This variant of the Hough transform improves the speed and efficiency of the standard Hough transform by minimizing the amount of computation needed for the detection of lines, which is realized by reducing the number of candidates and votes needed to reliably detect lines with different numbers of supporting points (Matas et al., 2000).

According to Matas et al. (2000), the algorithm repeatedly selects a random point for voting. After casting a vote, the hypothesis that “could the count be due to random noise?” is tested, based on a single comparison with a threshold per bin update (the threshold is also updated as votes are casted). In other words, the algorithm checks if the highest pick in the accumulator that was updated by the new point is higher than a threshold. After the detection of a line, the supporting points draw back their votes. Additionally, the remaining points supporting the lines which are not yet participated in the voting process are removed from the process. This reduces the amount of the remaining process, as the new random point is selected from the remaining points, and therefore only a small fraction of points are voted. This further reduces the number of false positives, where the assignment of points to lines is ambiguous, i.e. points are located in the neighborhood of more than one line.

E. Reconstruction of Detailed Models – Case Studies

This appendix presents study cases used for the assessment of the efficiency and robustness of the proposed reconstruction approach regarding parameter selection, different types of sensors (with different accuracies) and different room shapes, as explained in section 6.2.1. Existing gaps in the presented models are reconstructed in section 7.2, as a result of the fusion of these models to an available coarse model.

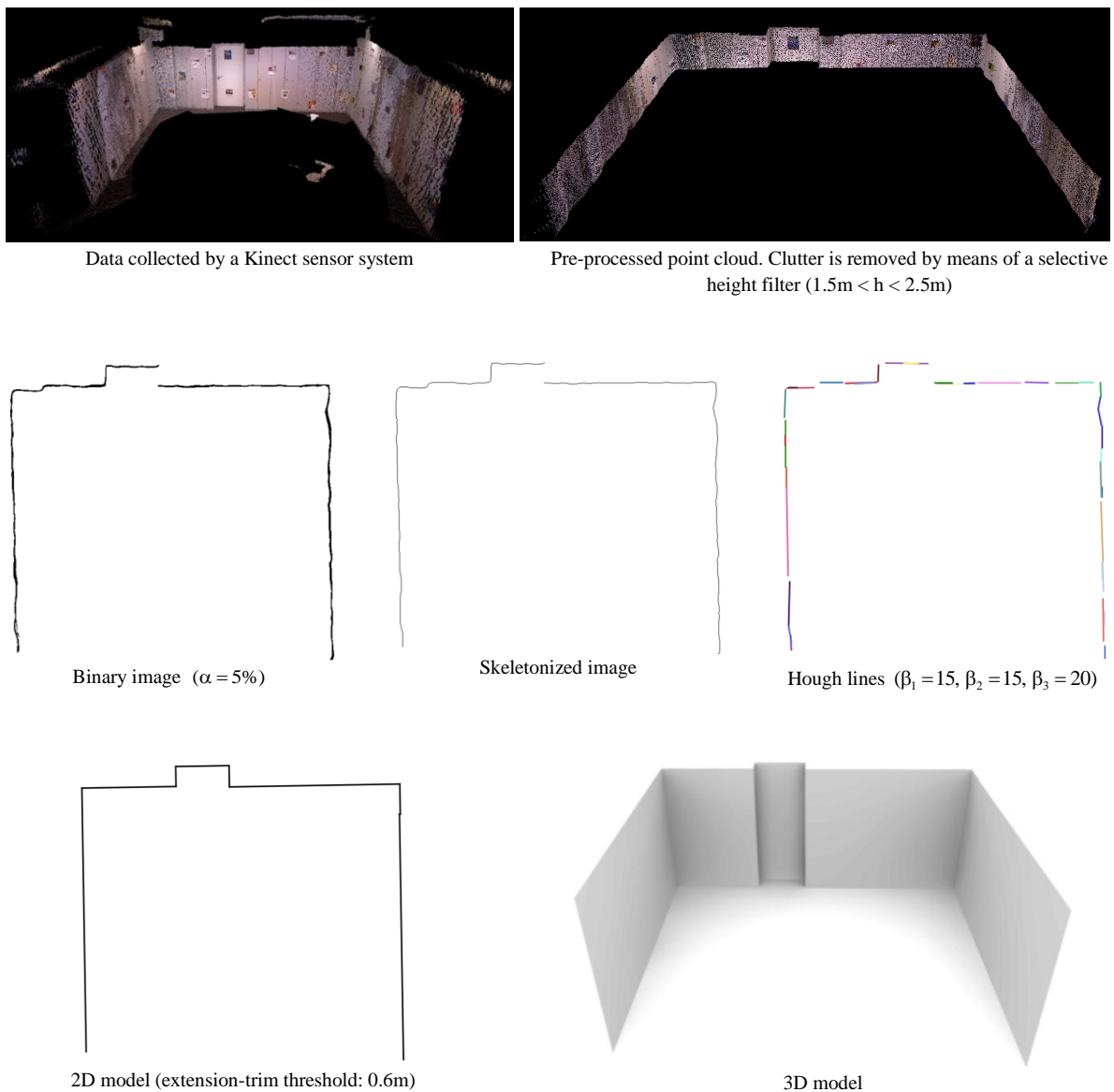
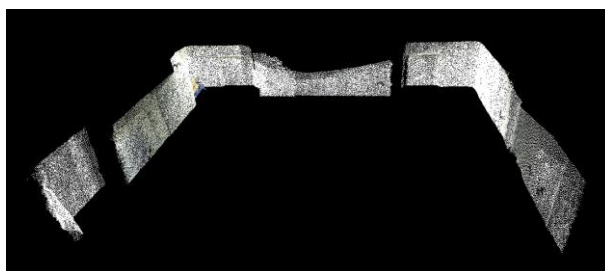


Figure E.1 – Modeling of a sample room captured by a Kinect sensor system.



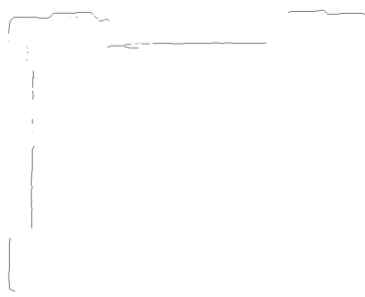
Data collected by a Kinect V2 sensor system



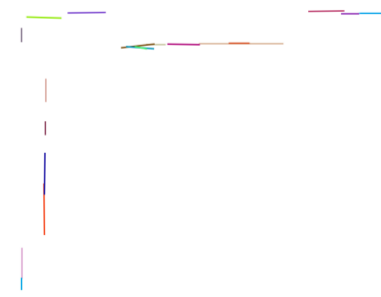
Pre-processed point cloud. Furniture is removed by means of a selective height filter ($1.5m < h < 2.5m$), remaining clutter is removed manually.



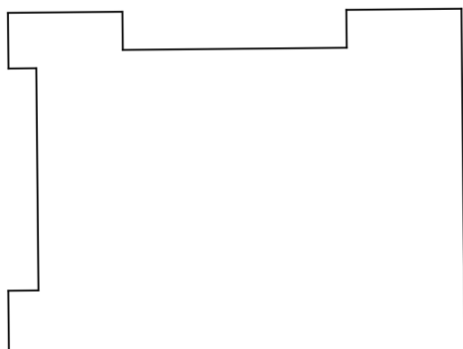
Binary image ($\alpha = 20\%$)



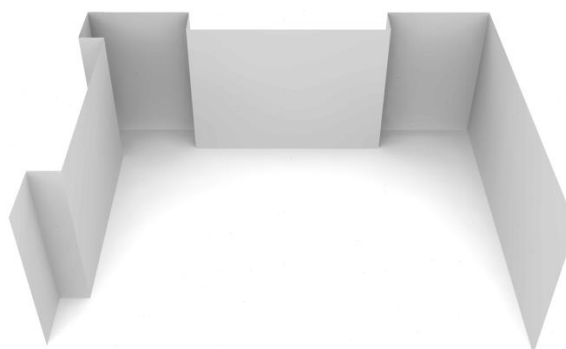
Skeletonized image



Hough lines ($\beta_1 = 15, \beta_2 = 15, \beta_3 = 20$)

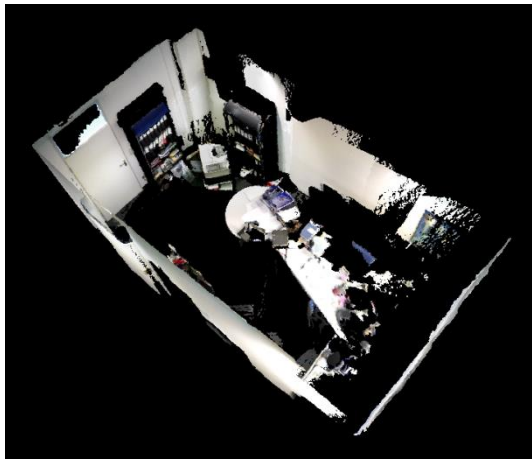


2D model (extension-trim threshold: 0.8m)



3D model

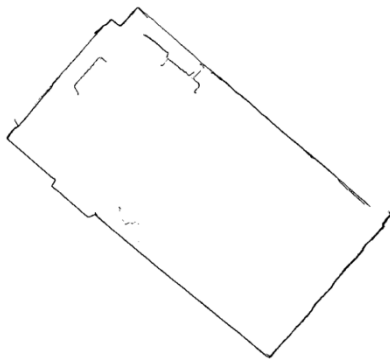
Figure E.2 – Modeling of a sample room captured by a Kinect V2 sensor system.



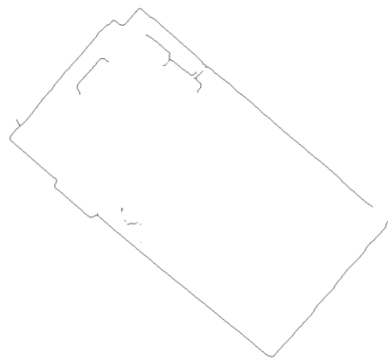
Data collected by a DPI-7 sensor system (ceiling points are removed for the visibility purpose)



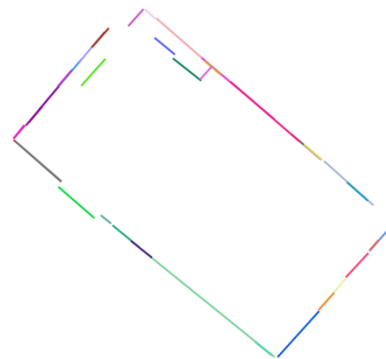
Pre-processed point cloud. Furniture is fully removed by means of a selective height filter ($1.5\text{m} < h < 2.5\text{m}$). Remaining clutter is removed in the binarization process.



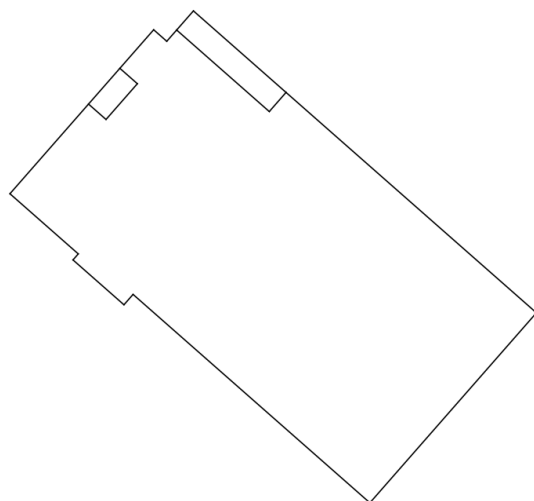
Binary image ($\alpha = 15\%$)



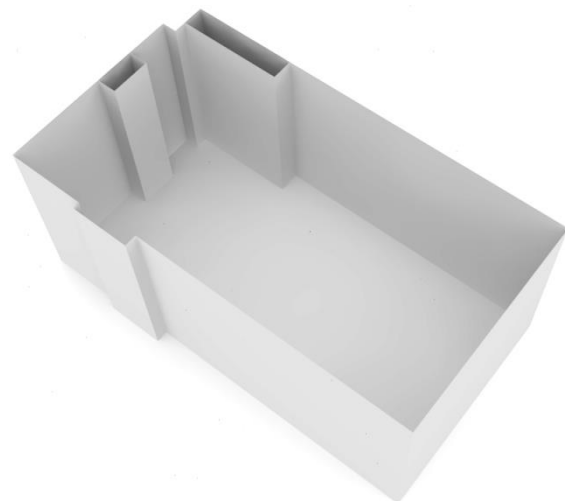
Skeletonized image



Hough lines ($\beta_1 = 15, \beta_2 = 15, \beta_3 = 20$)



2D model (extension-trim threshold: 0.5m)



3D model

Figure E.3 – Modeling of a sample room captured by a DPI-7 sensor system.

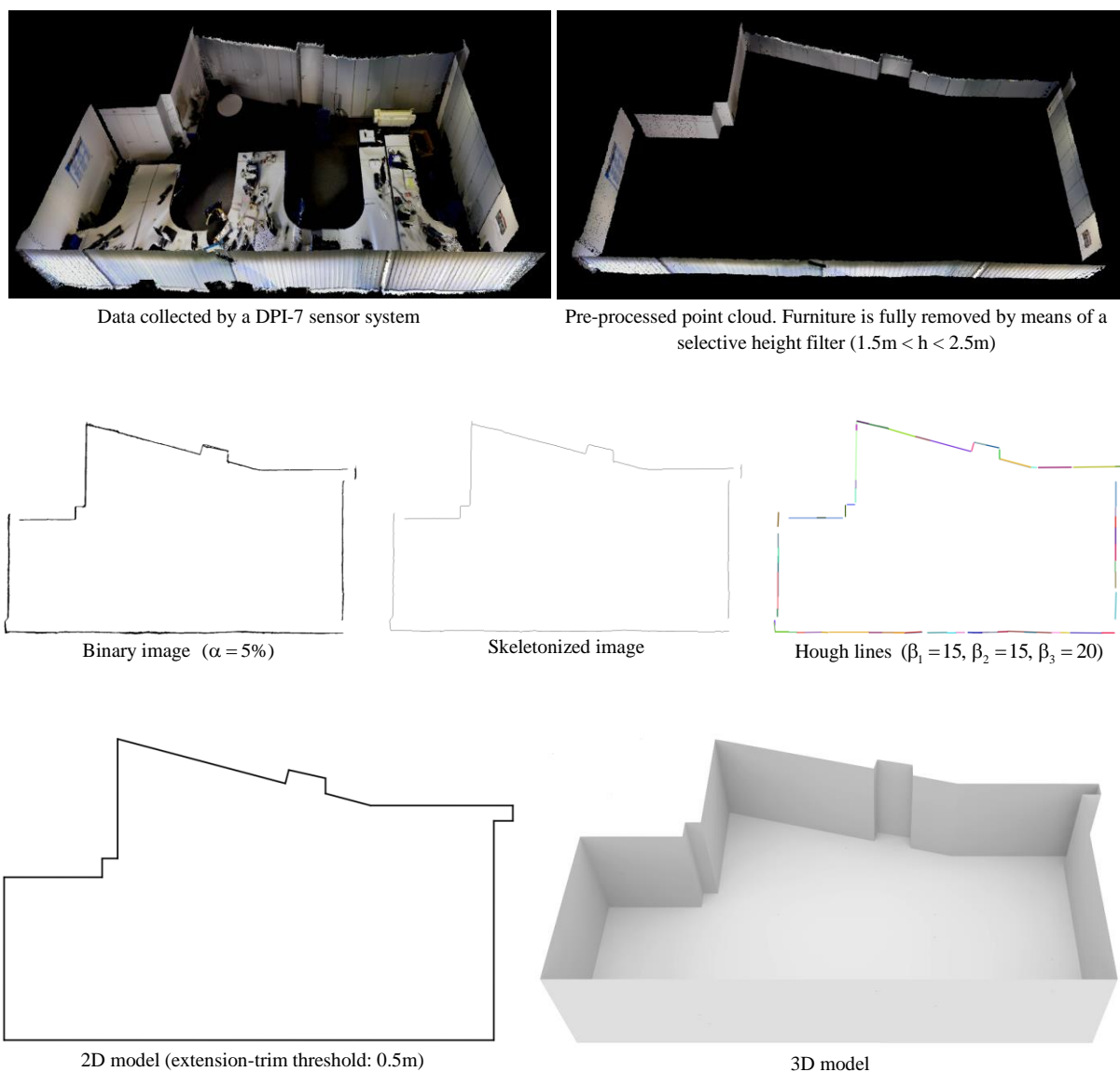
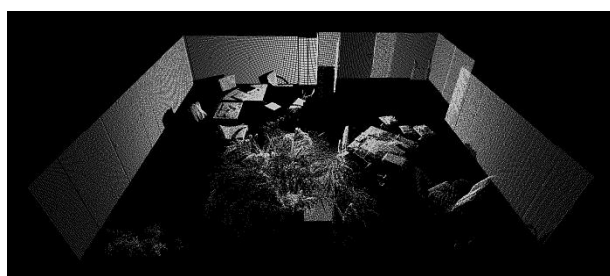
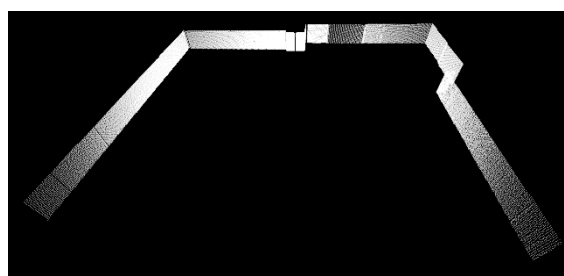


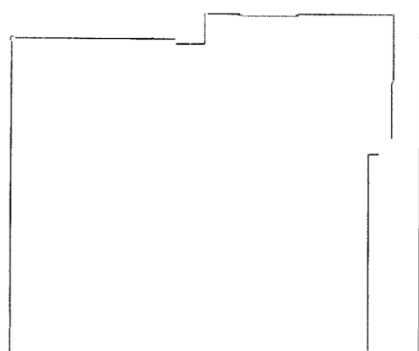
Figure E.4 – Modeling of a sample room captured by a DPI-7 sensor system.



Data collected by a Leica HDS3000 laser scanner



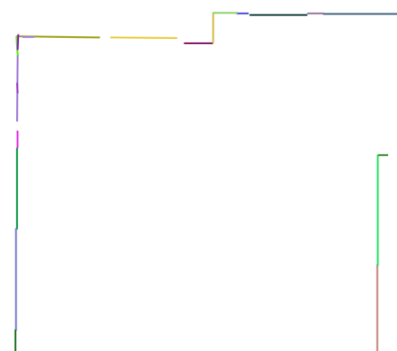
Pre-processed point cloud. Furniture is removed by means of a selective height filter ($1\text{m} < h < 1.5\text{m}$), remaining clutter is removed manually.



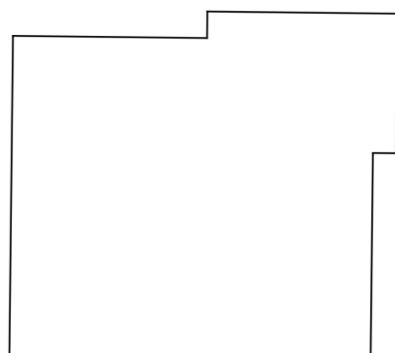
Binary image ($\alpha = 5\%$)



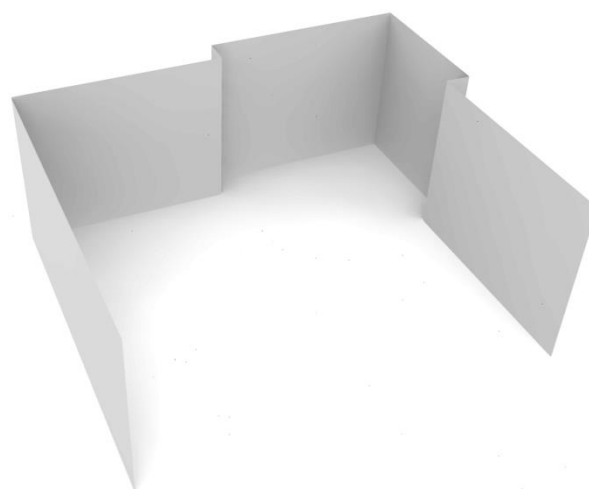
Skeletonized image



Hough lines ($\beta_1 = 15, \beta_2 = 15, \beta_3 = 20$)



2D model (extension-trim threshold: 0.5m)



3D model

Figure E.5 – Modeling of a sample room captured by a Leica HDS3000 laser scanner.

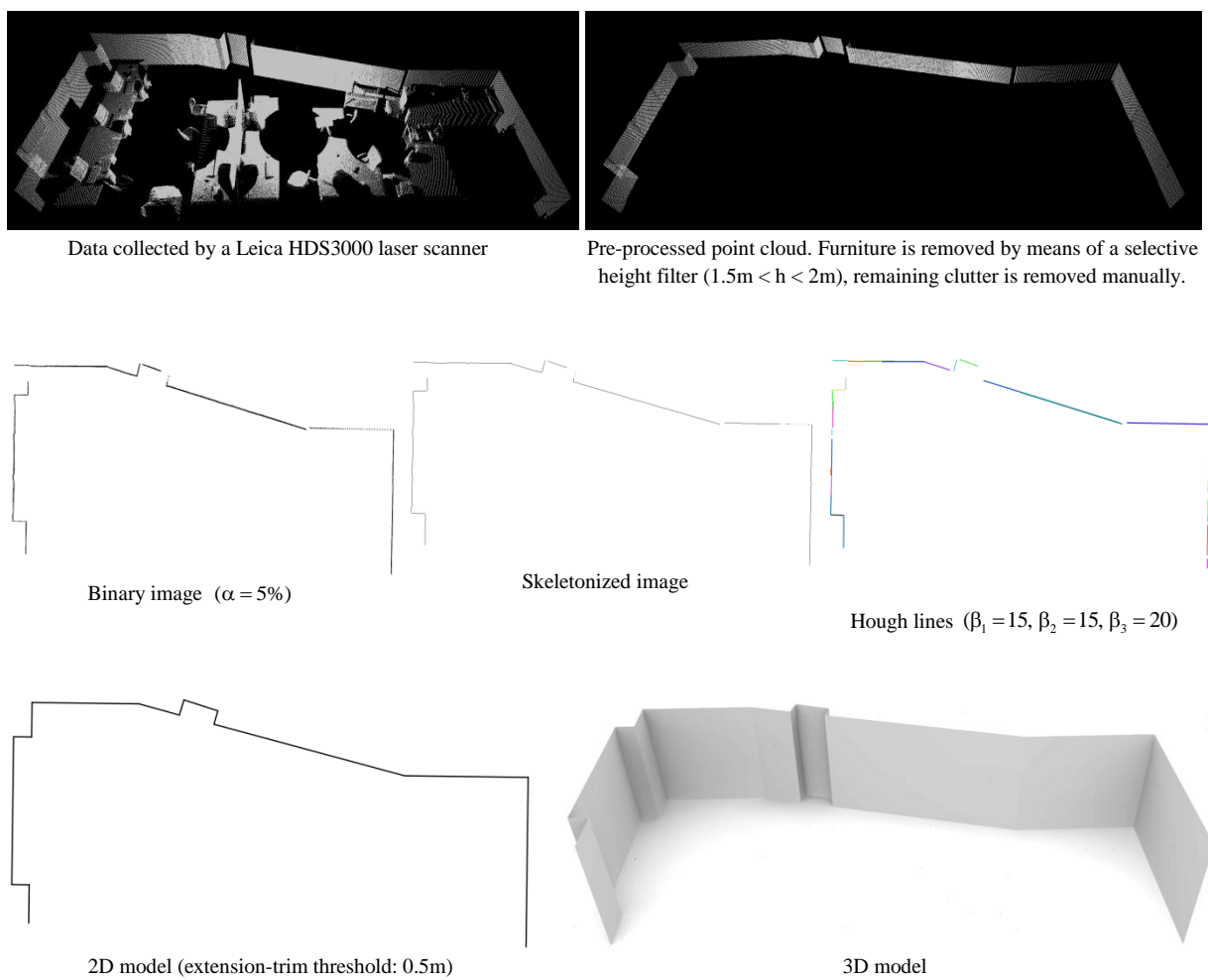


Figure E.6 – Modeling of a sample room captured by a Leica HDS3000 laser scanner.

References

- Adan, A., Huber, D., 2011. 3D reconstruction of interior wall surfaces under occlusion and clutter, in: 3D Imaging, Modeling, Processing, Visualization and Transmission (3DIMPVT), 2011 International Conference on. pp. 275–281.
- Ah-Soon, C., Tombre, K., 2001. Architectural symbol recognition using a network of constraints. *Pattern Recognition Letters* 22, 231–248.
- Ah-Soon, C., Tombre, K., 1997. Variations on the analysis of architectural drawings, in: *Document Analysis and Recognition, 1997.*, Proceedings of the Fourth International Conference on. IEEE, pp. 347–351.
- ATAP Project Tango [WWW Document], 2015. . Google. URL <https://www.google.com/atap/projecttango/> (accessed 3.11.15).
- Bamji, C.S., O'Connor, P., Elkhatib, T., Mehta, S., Thompson, B., Prather, L.A., Snow, D., Akkaya, O.C., Daniel, A., Payne, A.D., Perry, T., Fenton, M., Chan, V.-H., 2015. A 0.13 um CMOS System-on-Chip for a 512 x 424 Time-of-Flight Image Sensor With Multi-Frequency Photo-Demodulation up to 130 MHz and 2 GS/s ADC. *IEEE Journal of Solid-State Circuits* 50, 303–319. doi:10.1109/JSSC.2014.2364270
- Bay, H., Tuytelaars, T., Van Gool, L., 2006. Surf: Speeded up robust features, in: *Computer vision—ECCV 2006*. Springer, pp. 404–417.
- Becker, S., 2009. Generation and application of rules for quality dependent façade reconstruction. *ISPRS Journal of Photogrammetry and Remote Sensing* 64, 640–653. doi:10.1016/j.isprsjprs.2009.06.002
- Becker, S., Peter, M., Fritsch, D., Philipp, D., Baier, P., Dibak, C., 2013. Combined Grammar for the Modeling of Building Interiors. *ISPRS Annals of Photogrammetry, Remote Sensing and Spatial Information Sciences II-4/W1*, 1–6. doi:10.5194/isprannals-II-4-W1-1-2013
- Beraldin, J.A., Blais, F., Lohr, U., 2010. Laser scanning technology, in: *Airborne and Terrestrial Laser Scanning*, Ed. Vosselman, G. and Maas, H. G. Whittles Publishing, pp. 1–42.
- Beraldin, J.-A., Picard, M., El-Hakim, S., Godin, G., Borgeat, L., Blais, F., Paquet, E., Rioux, M., Valzano, V., Bandiera, A., 2005. Virtual reconstruction of heritage sites: opportunities and challenges created by 3D technologies. NRC Publications Record.
- Besl, P.J., McKay, N.D., 1992. Method for registration of 3-D shapes, in: *Robotics-DL Tentative*. pp. 586–606.
- Böhm, J., 2014. Accuracy Investigation for Structured-light Based Consumer 3D Sensors. *Photogrammetrie - Fernerkundung - Geoinformation* 2014, 117–127. doi:10.1127/1432-8364/2014/0214
- Böhm, J., Becker, S., 2007. Automatic marker-free registration of terrestrial laser scans using reflectance features, in: *Proceedings of 8th Conference on Optical 3D Measurement Techniques*. Zurich, Switzerland, pp. 338–344.
- Bradski, G., 2000. The OpenCV Library (2000). *Dr. Dobb's Journal of Software Tools*.
- Brown, D.C., 1971. Close-range camera calibration. *PHOTOGRAMMETRIC ENGINEERING* 37, 855–866.
- Budroni, A., 2013. Automatic Model Reconstruction of Indoor Manhattan-world Scenes from Dense Laser Range Data. Dissertation at the Institute for Photogrammetry, University of Stuttgart.
- Budroni, A., Böhm, J., 2009. Toward automatic reconstruction of interiors from laser data. *Proceedings of Virtual Reconstruction and Visualization of Complex Architectures (3D-Arch)*.
- Buxbaum, B., Schwarte, R., Ringbeck, T., Grothof, M., Luan, X., 2002. MSM-PMD as correlation receiver in a new 3D-ranging system, in: *International Symposium on Remote Sensing*. International Society for Optics and Photonics, pp. 145–153.
- Canny, J., 1986. A computational approach to edge detection. *Pattern Analysis and Machine Intelligence*, IEEE Transactions on 679–698.

- Chli, M., Furgale, P., Hutter, M., Siegwart, R., 2015. Lecture notes in Autonomous Mobile Robots, ASL (Master program), ETHZ.
- Color Structure Code [WWW Document], 2014. URL <http://www.uni-koblenz-landau.de/koblenz/fb4/icv//agprieese/research/ColorImgSeg/download/csc> (accessed 6.30.14).
- Connecting Kinects for Group Surveillance [WWW Document], 2014. URL <http://actu.epfl.ch/news/connecting-kinects-for-group-surveillance/> (accessed 2.19.14).
- Coughlan, J.M., Yuille, A.L., 2003. Manhattan world: Orientation and outlier detection by bayesian inference. *Neural Computation* 15, 1063–1088.
- Cramer, M., 2014. Lecture notes in Photogrammetry, Institute for Photogrammetry, University of Stuttgart.
- Criminisi, A., Reid, I., Zisserman, A., 1999. Single view metrology, in: *The Proceedings of the Seventh IEEE International Conference on Computer Vision*, 1999. pp. 434–441 vol.1. doi:10.1109/ICCV.1999.791253
- Criminisi, A., Reid, I., Zisserman, A., 1998. Computing 3D euclidean distance from a single view. Technical Report OUEL 2158/98, Dept. Eng. Science, University of Oxford.
- Delage, E., Lee, H., Ng, A.Y., 2006. A Dynamic Bayesian Network Model for Autonomous 3D Reconstruction from a Single Indoor Image, in: *2006 IEEE Computer Society Conference on Computer Vision and Pattern Recognition*. pp. 2418–2428. doi:10.1109/CVPR.2006.23
- Doc-Ok.org [WWW Document], 2015. URL <http://doc-ok.org/?p=584> (accessed 3.11.15).
- Documentation - Point Cloud Library (PCL) [WWW Document], 2015. URL http://pointclouds.org/documentation/tutorials/narf_feature_extraction.php (accessed 3.15.15).
- Dold, J., 1997. Ein hybrides photogrammetrisches Industriemesssystem höchster Genauigkeit und seine Überprüfung (PhD thesis). Univ. der Bundeswehr München, Fak. für Bauingenieur- und Vermessungswesen, Studiengang Vermessungswesen.
- Dosch, P., Tombre, K., Ah-Soon, C., Masini, G., 2000. A complete system for the analysis of architectural drawings. *International Journal on Document Analysis and Recognition* 3, 102–116.
- DotProduct LLC [WWW Document], 2015. URL <http://www.dotproduct3d.com> (accessed 3.9.15).
- DPI-7 User Manual, 2014.
- Duda, R.O., Hart, P.E., 1972. Use of the Hough transformation to detect lines and curves in pictures. *Communications of the ACM* 15, 11–15.
- EBS-Image [WWW Document], 2011. URL <http://www.ebsd-image.org/documentation/reference/ops/hough/ohoughtransform.html> (accessed 1.17.16).
- El-Hakim, S., 2002. Semi-automatic 3D reconstruction of occluded and unmarked surfaces from widely separated views. *Close Range Visualization Techniques*.
- El-Hakim, S., Beraldin, J.-A., 2006. Sensor integration and visualization. Chapter 10 of *Applications of 3D Measurement from Images*.
- Endres, F., Hess, J., Engelhard, N., Sturm, J., Cremers, D., Burgard, W., 2012. An evaluation of the RGB-D SLAM system, in: *Robotics and Automation (ICRA), 2012 IEEE International Conference on*. IEEE, pp. 1691–1696.
- Fischler, M.A., Bolles, R.C., 1981. Random sample consensus: a paradigm for model fitting with applications to image analysis and automated cartography. *Communications of the ACM* 24, 381–395.
- Frese, U., Wagner, R., Röfer, T., 2010. A SLAM Overview from a User's Perspective. *KI - Künstliche Intelligenz* 24, 191–198. doi:10.1007/s13218-010-0040-4
- Fritsch, D., 2014. Lecture notes in Terrestrial Laser Scanning (Terrestrisches Laserscanning), Institute for Photogrammetry, University of Stuttgart.
- Furukawa, Y., Curless, B., Seitz, S.M., Szeliski, R., 2009a. Reconstructing building interiors from images, in: *2009 IEEE 12th International Conference on Computer Vision*. pp. 80–87. doi:10.1109/ICCV.2009.5459145
- Furukawa, Y., Curless, B., Seitz, S.M., Szeliski, R., 2009b. Manhattan-world stereo, in: *Computer Vision and Pattern Recognition, 2009. IEEE Conference on*. pp. 1422–1429.
- GestSure [WWW Document], 2014. URL <http://gestsure.com/> (accessed 2.19.14).
- Godha, S., Lachapelle, G., 2008. Foot mounted inertial system for pedestrian navigation. *Measurement Science and Technology* 19, 075202. doi:10.1088/0957-0233/19/7/075202
- Google Store [WWW Document], 2015. URL https://store.google.com/product/project_tango_tablet_black?playredirect=true
- Gröger, G., Plümer, L., 2010. Derivation of 3D indoor models by grammars for route planning. *Photogrammetrie-Fernerkundung-Geoinformation* 2010, 191–206.

- Guidi, G., Remondino, F., 2012. 3D Modelling from Real Data, in: *Modelling and Simulation in Engineering*, Ed. Catalin, A. INTECH Open Access Publisher.
- Haala, N., Fritsch, D., Peter, M., Khosravani, A.M., 2011. Pedestrian mobile mapping system for indoor environments based on MEMS IMU and range camera. *Archives of Photogrammetry, Cartography and Remote Sensing* 22, 159–172.
- Hähnel, D., Burgard, W., Thrun, S., 2003. Learning compact 3D models of indoor and outdoor environments with a mobile robot. *Robotics and Autonomous Systems* 44, 15–27. doi:10.1016/S0921-8890(03)00007-1
- Han, F., Zhu, S.-C., 2009. Bottom-up/top-down image parsing with attribute grammar. *Pattern Analysis and Machine Intelligence, IEEE Transactions on* 31, 59–73.
- Hartley, R., Zisserman, A., 2003. *Multiple view geometry in computer vision*. Cambridge university press.
- Henry, P., Krainin, M., Herbst, E., Ren, X., Fox, D., 2012. RGB-D mapping: Using Kinect-style depth cameras for dense 3D modeling of indoor environments. *The International Journal of Robotics Research* 31, 647–663.
- Hong, S., Ye, C., Bruch, M., Halterman, R., 2012. Performance evaluation of a Pose Estimation method based on the SwissRanger SR4000, in: *Mechatronics and Automation (ICMA), 2012 International Conference on*. IEEE, pp. 499–504.
- Horna, S., Damiand, G., Meneveaux, D., Bertrand, Y., others, 2007. Building 3D indoor scenes topology from 2D architectural plans., in: *Proc. of 2nd International Conference on Computer Graphics Theory and Applications (GRAPP)*. Barcelona, Spain, pp. 37–44.
- Horn, B.K., 1987. Closed-form solution of absolute orientation using unit quaternions. *Optical Society of America* 4, 629–642.
- Hough, P.V.C., 1962. Method and means for recognizing complex patterns. US3069654 A.
- Huang, J., Cowan, B., 2009. Simple 3D Reconstruction of Single Indoor Image with Perspective Cues. Presented at the *Computer and Robot Vision, 2009. CRV '09. Canadian Conference on*, IEEE, Kelowna, BC, pp. 140–147. doi:10.1109/CRV.2009.33
- Jain, R., Kasturi, R., Schunck, B.G., 1995. *Machine Vision*. McGraw-Hill.
- Jenke, P., Huhle, B., Straßer, W., 2009. Statistical reconstruction of indoor scenes, in: *Proc. WSCG '09 (2009)*.
- Kemper, A., Wallrath, M., 1987. An analysis of geometric modeling in database systems. *ACM Computing Surveys (CSUR)* 19, 47–91.
- Khoshelham, K., Díaz-Vilariño, L., 2014. 3D Modelling of Interior Spaces: Learning the Language of Indoor Architecture. *ISPRS - International Archives of the Photogrammetry, Remote Sensing and Spatial Information Sciences* XL-5, 321–326. doi:10.5194/isprsarchives-XL-5-321-2014
- Khoshelham, K., Elberink, S.O., 2012. Accuracy and Resolution of Kinect Depth Data for Indoor Mapping Applications. *Sensors* 12, 1437–1454. doi:10.3390/s120201437
- Klein, G., Murray, D., 2007. Parallel tracking and mapping for small AR workspaces, in: *Mixed and Augmented Reality, 2007. ISMAR 2007. 6th IEEE and ACM International Symposium on*. pp. 225–234.
- Kodinariya, T.M., Makwana, P.R., 2013. Review on determining number of Cluster in K-Means Clustering. *International Journal of Advance Research in Computer Science and Management Studies* 1.
- Kolb, A., Barth, E., Koch, R., Larsen, R., 2009. Time-of-flight sensors in computer graphics, in: *Proc. Eurographics (State-of-the-Art Report)*. pp. 119–134.
- Kolbe, T.H., Gröger, G., Plümer, L., 2005. CityGML: Interoperable access to 3D city models, in: *Geo-Information for Disaster Management*. Springer, pp. 883–899.
- Kraft, H., Frey, J., Moeller, T., Albrecht, M., Grothof, M., Schink, B., Hess, H., Buxbaum, B., 2004. 3D-camera of high 3D-frame rate, depth-resolution and background light elimination based on improved PMD (photonic mixer device)-technologies. *OPTO, Nuernberg, May 2004*.
- Lancaster, P., Salkauskas, K., 1981. Surfaces generated by moving least squares methods. *Mathematics of computation* 37, 141–158.
- Leica Cyclone [WWW Document], 2014. URL http://hds.leica-geosystems.com/en/Leica-Cyclone_6515.htm (accessed 12.9.14).
- Leica HDS3000 Product Specifications [WWW Document], 2015. URL http://hds.leica-geosystems.com/hds/en/Leica_HDS3000.pdf (accessed 2.14.15).
- Leonard, J.J., Durrant-Whyte, H.F., 1991. Mobile robot localization by tracking geometric beacons. *Robotics and Automation, IEEE Transactions on* 7, 376–382.
- Leutenegger, S., Furgale, P.T., Rabaud, V., Chli, M., Konolige, K., Siegwart, R., 2013.

- Keyframe-Based Visual-Inertial SLAM using Nonlinear Optimization., in: *Robotics: Science and Systems*.
- Lewis, R., Séquin, C., 1998. Generation of 3D building models from 2D architectural plans. *Computer-Aided Design* 30, 765–779.
- Lindner, M., Kolb, A., Ringbeck, T., 2008. New insights into the calibration of ToF-sensors, in: *Computer Vision and Pattern Recognition Workshops, 2008. CVPRW'08. IEEE Computer Society Conference on. IEEE*, pp. 1–5.
- Lloyd, S., 1982. Least squares quantization in PCM. *Information Theory, IEEE Transactions on* 28, 129–137.
- Loriggio, P., 2011. *Globe and Mail* [WWW Document]. Toronto: Globe and Mail. URL <http://www.theglobeandmail.com/technology/gadgets-and-gear/gadgets/toronto-doctors-try-microsofts-kinect-in-or/article573347/>
- Lowe, D.G., 2004. Distinctive image features from scale-invariant keypoints. *International journal of computer vision* 60, 91–110.
- Luhmann, T., Robson, S., Kyle, S., Boehm, J., 2014. *Close-range Photogrammetry and 3D Imaging*. De Gruyter.
- Lu, T., Tai, C.-L., Bao, L., Su, F., Cai, S., 2005. 3D Reconstruction of Detailed Buildings from Architectural Drawings. *Computer-Aided Design and Applications* 2, 527–536. doi:10.1080/16864360.2005.10738402
- Lu, T., Yang, H., Yang, R., Cai, S., 2007. Automatic analysis and integration of architectural drawings. *International Journal of Document Analysis and Recognition (IJ DAR)* 9, 31–47.
- Maas, H.-G., 2008. Close-range photogrammetry sensors, in: *Advances in Photogrammetry, Remote Sensing and Spatial Information Science: 2008 ISPRS Congress Book*. pp. 63–72.
- Matas, J., Galambos, C., Kittler, J., 2000. Robust Detection of Lines Using the Progressive Probabilistic Hough Transform. *Computer Vision and Image Understanding* 78, 119–137. doi:10.1006/cviu.1999.0831
- May, S., Dröschel, D., Fuchs, S., Holz, D., Nuchter, A., 2009. Robust 3D-mapping with time-of-flight cameras, in: *Intelligent Robots and Systems, 2009. IROS 2009. IEEE/RSJ International Conference on. IEEE*, pp. 1673–1678.
- Menna, F., Remondino, F., Battisti, R., Nocerino, E., 2011. Geometric investigation of a gaming active device, in: *Remondino, F., Shortis, M.R.* (Eds.), . p. 80850G–80850G–15. doi:10.1117/12.890070
- Microsoft news [WWW Document], 2013. . Microsoft News. URL <http://microsoft-news.com/microsoft-76-million-xbox-360-consoles-and-24-million-kinect-sensors-sold-since-launch/> (accessed 1.17.16).
- MID Brochure [WWW Document], 2014. URL http://mapindoor.com/Brochure_MID.pdf (accessed 3.9.15).
- Mikolajczyk, K., Schmid, C., 2004. Scale & affine invariant interest point detectors. *International journal of computer vision* 60, 63–86.
- MSDN Kinect [WWW Document], 2015. URL <https://msdn.microsoft.com/en-us/library/jj131033.aspx> (accessed 3.9.15).
- MS Robotics Developer Studio [WWW Document], 2014. URL <http://msdn.microsoft.com/en-us/library/bb648760.aspx> (accessed 12.31.14).
- Müller, P., Wonka, P., Haegler, S., Ulmer, A., Van Gool, L., 2006. Procedural modeling of buildings. *ACM*.
- Nealen, A., 2004. An as-short-as-possible introduction to the least squares, weighted least squares and moving least squares methods for scattered data approximation and interpolation. URL: <http://www.nealen.com/projects> 130, 150.
- Newcombe, R.A., Davison, A.J., Izadi, S., Kohli, P., Hilliges, O., Shotton, J., Molyneaux, D., Hodges, S., Kim, D., Fitzgibbon, A., 2011. KinectFusion: Real-time dense surface mapping and tracking, in: *2011 10th IEEE International Symposium on Mixed and Augmented Reality (ISMAR)*. Presented at the 2011 10th IEEE International Symposium on Mixed and Augmented Reality (ISMAR), pp. 127–136. doi:10.1109/ISMAR.2011.6092378
- Nüchter, A., Lingemann, K., Hertzberg, J., Surmann, H., 2007. 6D SLAM—3D mapping outdoor environments. *J. Field Robotics* 24, 699–722. doi:10.1002/rob.20209
- Oesau, S., Lafarge, F., Alliez, P., 2014. Indoor scene reconstruction using feature sensitive primitive extraction and graph-cut. *ISPRS Journal of Photogrammetry and Remote Sensing* 90, 68–82. doi:10.1016/j.isprsjprs.2014.02.004
- Okorn, B., Xiong, X., Akinci, B., Huber, D., 2010. Toward automated modeling of floor plans, in: *Proceedings of the Symposium on 3D Data Processing, Visualization and Transmission*.
- Panushev, I., Brandt, J., 2007. *3D Imaging Pilot Projects: Three Case Studies (Research Report)*. Harvard Design School, Boston, MA.

- Pattinson, T., 2010. Quantification and Description of Distance Measurement Errors of a Time-of-Flight Camera. M. Sc. Thesis, University of Stuttgart, Stuttgart, Germany.
- Peter, M., Becker, S., Fritsch, D., 2013a. Grammar Supported Indoor Mapping, in: Proceedings of the 26th International Cartographic Conference (ICC). Dresden, Germany, pp. 1–18.
- Peter, M., Haala, N., Fritsch, D., 2011. Using photographed evacuation plans to support MEMS IMU navigation, in: Proceedings of the 2011 International Conference on Indoor Positioning and Indoor Navigation (IPIN2011). Guimaraes, Portugal.
- Peter, M., Haala, N., Schenk, M., Otto, T., 2010. Indoor Navigation and Modeling Using Photographed Evacuation Plans and MEMS IMU, in: ISPRS Archives, Vol. XXXVIII, Part 4, Commission IV Symposium. ISPRS, Orlando, USA.
- Peter, M., Khosravani, A.M., Fritsch, D., 2013b. Refinement of Coarse Indoor Models using Position Traces and a Low-Cost Range Camera, in: International Conference on Indoor Positioning and Indoor Navigation. p. 31.
- Philipp, D., Baier, P., Dibak, C., Durr, F., Rothermel, K., Becker, S., Peter, M., Fritsch, D., 2014. MapGENIE: Grammar-enhanced indoor map construction from crowd-sourced data, in: Pervasive Computing and Communications (PerCom), 2014 IEEE International Conference on. IEEE, pp. 139–147.
- PMDTechnologies [WWW Document], 2015. URL <http://pmdtec.com> (accessed 3.12.15).
- Previtali, M., Barazzetti, L., Brumana, R., Scaioni, M., 2014. Towards automatic indoor reconstruction of cluttered building rooms from point clouds. ISPRS Annals of Photogrammetry, Remote Sensing and Spatial Information Sciences II-5, 281–288. doi:10.5194/isprsannals-II-5-281-2014
- ReconstructMe [WWW Document], 2015. URL <http://reconstructme.net/> (accessed 6.4.15).
- Remondino, F., 2010. Terrestrial Optical Active Sensors - Theory & Applications. Presented at the International Summer School “3D Modeling in Archaeology and Cultural Heritage, Durham, UK.
- Remondino, F., 2003. From point cloud to surface: the modeling and visualization problem, in: International Workshop on Visualization and Animation of Reality-Based 3D Models. p. 5.
- Remondino, F., El-Hakim, S., 2006. Image-based 3D Modelling: A Review. The Photogrammetric Record 21, 269–291.
- Riisgaard, S., Blas, M.R., 2003. SLAM for Dummies - A Tutorial Approach to Simultaneous Localization and Mapping.
- ROS Kinect calibration [WWW Document], 2011. URL http://wiki.ros.org/kinect_calibration/technical (accessed 1.28.11).
- Rosten, E., Drummond, T., 2006. Machine learning for high-speed corner detection, in: Computer Vision–ECCV 2006. Springer, pp. 430–443.
- Rosten, E., Drummond, T., 2005. Fusing points and lines for high performance tracking, in: Computer Vision, 2005. ICCV 2005. Tenth IEEE International Conference on. IEEE, pp. 1508–1515.
- Rottensteiner, F., 2000. Semi-automatic building reconstruction integrated in strict bundle block adjustment. International Archives of Photogrammetry and Remote Sensing 33, 461–468.
- Rusu, R.B., Cousins, S., 2011. 3D is here: Point Cloud Library (PCL), in: Robotics and Automation (ICRA), 2011 IEEE International Conference on. IEEE, pp. 1–4.
- Sanso, F., 1973. An exact solution of the roto-translation problem. Photogrammetria 29, 203–216.
- Say hello to Project Tango!, 2014.
- SCENECT [WWW Document], 2015. URL <http://www.faro.com/de-de/scenect/scenect> (accessed 3.15.15).
- Schnabel, R., Wahl, R., Klein, R., 2007. Efficient RANSAC for Point-Cloud Shape Detection, in: Computer Graphics Forum. Wiley Online Library, pp. 214–226.
- Sell, J., O’Connor, P., 2014. The Xbox One System on a Chip and Kinect Sensor.
- Sensopia Inc. [WWW Document], 2014. URL <http://www.sensopia.com/english/index.html> (accessed 12.12.14).
- Shum, H.-Y., Han, M., Szeliski, R., 1998. Interactive construction of 3D models from panoramic mosaics, in: Computer Vision and Pattern Recognition, 1998. Proceedings. 1998 IEEE Computer Society Conference on. IEEE, pp. 427–433.
- Sinha, S.N., Steedly, D., Szeliski, R., Agrawala, M., Pollefeys, M., 2008. Interactive 3D architectural modeling from unordered photo collections, in: ACM Transactions on Graphics (TOG). ACM, p. 159.
- Skaneet by Occipital [WWW Document], 2015. . Skaneet 3D Scanning Software By Occipital.

- URL <http://skanect.occipital.com> (accessed 3.15.15).
- Skolnik, M.I., 1980. Introduction to radar systems, 2nd ed. McGraw-Hill, NY, USA.
- Smith, R., Self, M., Cheeseman, P., 1990. Estimating uncertain spatial relationships in robotics, in: *Autonomous Robot Vehicles*. Springer, pp. 167–193.
- Snavely, K.N., 2008. Scene reconstruction and visualization from internet photo collections. University of Washington.
- Snavely, N., Seitz, S.M., Szeliski, R., 2006. Photo tourism: exploring photo collections in 3D. *ACM transactions on graphics (TOG)* 25, 835–846.
- Steder, B., Rusu, R.B., Konolige, K., Burgard, W., 2011. Point feature extraction on 3D range scans taking into account object boundaries, in: *Robotics and Automation (icra), 2011 Ieee International Conference on*. IEEE, pp. 2601–2608.
- Stiny, G., Mitchell, W.J., others, 1978. The palladian grammar. *Environment and Planning B* 5, 5–18.
- structure.io [WWW Document], 2014. URL <http://structure.io/> (accessed 5.23.14).
- Tango Concepts [WWW Document], 2015. . Google Developers. URL <https://developers.google.com/project-tango/overview/concepts> (accessed 3.12.15).
- Tang, P., Huber, D., Akinci, B., Lipman, R., Lytle, A., 2010. Automatic reconstruction of as-built building information models from laser-scanned point clouds: A review of related techniques. *Automation in Construction* 19, 829–843. doi:10.1016/j.autcon.2010.06.007
- Tang, R., Fritsch, D., Cramer, M., 2012. A novel family of mathematical self-calibration additional parameters for airborne camera systems. Castelldefels (Catalunya, Spain): EuroCOW.
- The Verge [WWW Document], 2015. . The Verge. URL <http://www.theverge.com/2015/1/30/7952949/google-project-tango-graduates-from-atap> (accessed 3.11.15).
- Thomson, C., Apostolopoulos, G., Backes, D., Boehm, J., 2013. Mobile Laser Scanning for Indoor Modelling. *ISPRS Annals of Photogrammetry, Remote Sensing and Spatial Information Sciences II-5/W2*, 289–293. doi:10.5194/isprsannals-II-5-W2-289-2013
- Thorndike, R.L., 1953. Who belongs in the family? *Psychometrika* 18, 267–276.
- Thorsten, R., Hagebecker, B., 2007. A 3D time of flight camera for object detection. *Optical 3-D Measurement Techniques*.
- Toldo, R., Fusiello, A., 2014. J-linkage: Robust fitting of multiple models [WWW Document]. URL <http://www.diegm.uniud.it/fusiello/demo/jlk/> (accessed 12.25.14).
- Toldo, R., Fusiello, A., 2008. Robust multiple structures estimation with j-linkage, in: *Computer Vision–ECCV 2008*. Springer, pp. 537–547.
- Triggs, B., Zisserman, A., Szeliski, R., 2000. *Vision Algorithms: Theory and Practice: International Workshop on Vision Algorithms Corfu, Greece, September 21-22, 1999 Proceedings*. Springer Science & Business Media.
- UrgBenri Information Page [WWW Document], 2015. URL <https://www.hokuyo-aut.jp/02sensor/07scanner/download/products/urg-04lx-ug01/data/UrgBenri.htm> (accessed 3.6.15).
- U.S. General Services Administration [WWW Document], 2009. . GSA BIM Guide for 3D Imaging, ver. 1.0, vol. 3. URL http://www.gsa.gov/graphics/pbs/GSA_BIM_Guide_Series_03.pdf (accessed 12.4.14).
- Valero, E., Adán, A., Cerrada, C., 2012. Automatic Method for Building Indoor Boundary Models from Dense Point Clouds Collected by Laser Scanners. *Sensors* 12, 16099–16115. doi:10.3390/s121216099
- Van Nieuwenhove, D., 2011. Optrima Technology Overview about DepthSense and OptriCam, in: *International Workshop on Range-Imaging Sensors and Applications (RISA) 2011*. Trento, Italy.
- Vosselman, G.V., Maas, H.-G., 2010. Airborne and terrestrial laser scanning. Whittles.
- Wagner, W., Ullrich, A., Melzer, T., Briese, C., Kraus, K., 2004. From single-pulse to full-waveform airborne laser scanners: potential and practical challenges. *International Archives of Photogrammetry, Remote Sensing and Spatial Information Sciences* 35, 201–206.
- Walker, E.G.L., 1989. Frame-based geometric reasoning for construction and maintenance of three-dimensional world models.
- Wallis, R., 1976. An approach to the space variant restoration and enhancement of images, in: *Proc. of Symp. on Current Mathematical Problems in Image Science*, Naval Postgraduate School, Monterey CA, USA, November. pp. 329–340.

- Wester-Ebbinghaus, W., 1981. Zur Verfahrensentwicklung in der Nahbereichsphotogrammetrie.
- Whelan, T., Johannsson, H., Kaess, M., Leonard, J.J., McDonald, J., 2013. Robust real-time visual odometry for dense RGB-D mapping, in: Robotics and Automation (ICRA), 2013 IEEE International Conference on. IEEE, pp. 5724–5731.
- Wonka, P., Wimmer, M., Sillion, F., Ribarsky, W., 2003. Instant architecture. ACM.
- Wu, C., 2013. Towards Linear-Time Incremental Structure from Motion. IEEE, pp. 127–134. doi:10.1109/3DV.2013.25
- Wu, C., Agarwal, S., Curless, B., Seitz, S.M., 2011. Multicore bundle adjustment, in: Computer Vision and Pattern Recognition (CVPR), 2011 IEEE Conference on. IEEE, pp. 3057–3064.
- Wurm, K.M., Hornung, A., Bennewitz, M., Stachniss, C., Burgard, W., 2010. OctoMap: A probabilistic, flexible, and compact 3D map representation for robotic systems, in: Proc. of the ICRA 2010 Workshop on Best Practice in 3D Perception and Modeling for Mobile Manipulation.
- Xbox One Kinect Teardown [WWW Document], 2013. iFixit. URL <https://www.ifixit.com/Teardown/Xbox+One+Kinect+Teardown/19725> (accessed 1.18.16).
- Xiao, J., Furukawa, Y., 2012. Reconstructing the world's museums, in: Computer Vision–ECCV 2012. Springer, pp. 668–681.
- Yahav, G., Iddan, G.J., Mandelboum, D., 2007. 3D Imaging Camera for Gaming Application, in: Consumer Electronics, 2007. ICCE 2007. Digest of Technical Papers. International Conference on.
- Yin, X., Wonka, P., Razdan, A., 2009. Generating 3D building models from architectural drawings: A survey. Computer Graphics and Applications, IEEE 29, 20–30.
- Yu, F., Lu, Z., Luo, H., Wang, P., 2011. Three-dimensional model analysis and processing. Springer.
- Zhang, R., Tsai, P.-S., Cryer, J.E., Shah, M., 1999. Shape-from-shading: a survey. Pattern Analysis and Machine Intelligence, IEEE Transactions on 21, 690–706.
- Zhang, T.Y., Suen, C.Y., 1984. A fast parallel algorithm for thinning digital patterns. Communications of the ACM 27, 236–239.

Relevant Publications

Most parts of the presented work have been published in:

- Peter, M., Khosravani, A.M., Fritsch, D., 2013. Refinement of coarse indoor models using position traces and a low-cost range camera, in: International Conference on Indoor Positioning and Indoor Navigation. p. 31. (IEEE Conference Publications)
- Khosravani, A.M., Peter, M., Fritsch, D., 2013. Alignment of range image data based on MEMS IMU and coarse 3D models derived from evacuation plans, in: SPIE Optical Metrology. p. 87910F.
- Khosravani, A.M., Lingenfelder, M., Wenzel, K., Fritsch, D., 2012. Co-registration of Kinect point clouds based on image and object space observations. Presented at the LC3D workshop, Berlin.
- Haala, N., Fritsch, D., Peter, M., Khosravani, A.M., 2011. Pedestrian mobile mapping system for indoor environments based on MEMS IMU and range camera. Archives of Photogrammetry, Cartography and Remote Sensing 22, 159–172.
- Haala, N., Fritsch, D., Peter, M., Khosravani, A.M., 2011. Pedestrian navigation and modeling for indoor environments, in: Proceeding of 7th International Symposium on Mobile Mapping Technology, Cracow, Poland.
- Fritsch, D., Khosravani, A.M., Cefalu, A., Wenzel, K., 2011. Multi-sensors and multiray reconstruction for digital preservation, in: Photogrammetric Week, Ed. Fritsch, D., pp. 305–323.

Curriculum Vitae

Personal

Name	Ali Mohammad Khosravani
Date and Place of Birth	16.09.1984 in Shiraz, Iran

Education

2010 – 2015	Ph.D. candidate at the Institute for Photogrammetry, University of Stuttgart, Germany
2008 – 2010	M.Sc. studies in Geomatics Engineering, University of Stuttgart, Germany
2002 – 2007	B.Sc. studies in Geomatics Engineering, University of Isfahan, Iran

Acknowledgment

First of all, I would like to express my profound gratitude to Prof. Dr.-Ing. Dieter Fritsch, for giving me the opportunity to do my PhD research at the Institute for Photogrammetry (ifp), for his kind supports during this time and the supervision of this work.

Also I would like to thank all my colleagues at ifp for their kind supports and cooperation. I specially would like to appreciate Prof. Dr.-Ing. Norbert Haala, Dr.-Ing. Michael Peter and Dipl.-Ing. Alessandro Cefalu for their invaluable advices and supports; without their help this work could not be successfully finished. I would also like to thank Dipl.-Ing. Max Schneider for providing me with the data collected by Kinect V2.

I also would like to thank the Ministry of Science, Research and the Arts of Baden-Württemberg for funding this work for the duration of 3 years, through the “Landesgraduierten-förderung” scholarship.

Finally, I wish to express my heartily thanks and gratitude to my mother, Yasmin and Aryan for their endless love and supports.